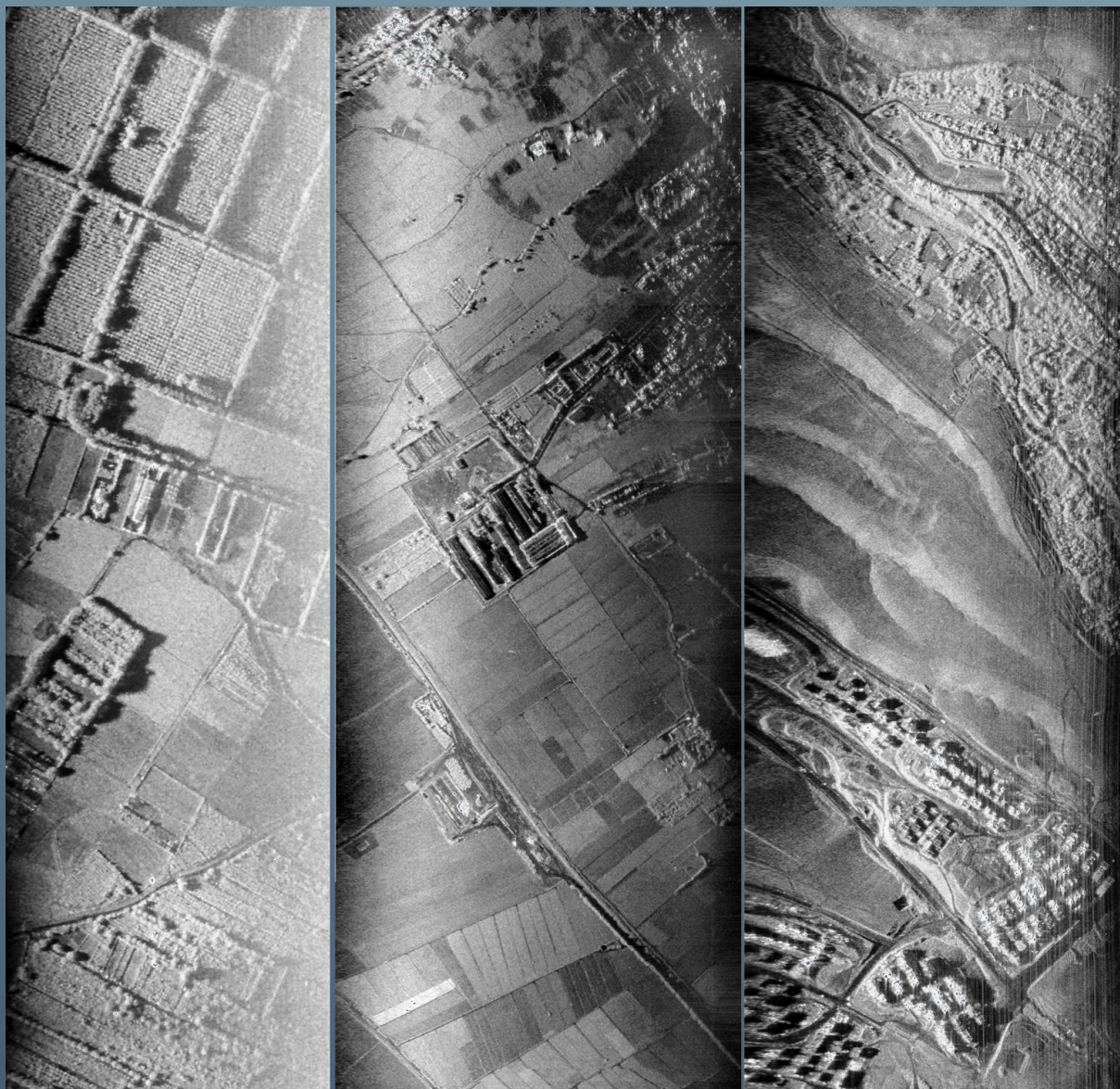


Ph.D. Thesis

**Synthetic Aperture Radar Signal  
Processing Using Nonlinear Frequency  
Modulation and Phase Error Compensation**



**Author: Jamal Saeedi**

**Thesis advisor: Prof. Karim Faez**



**Amirkabir University of Technology  
(Tehran Polytechnic)**

**Electrical Engineering Department**

A Thesis Submitted in Partial Fulfillment of the Requirement for the  
Degree of Doctor of Philosophy in Electrical Engineering, Electronics

**Title**

Synthetic Aperture Radar Signal Processing Using  
Nonlinear Frequency Modulation and Phase Error  
Compensation

**By**

Jamal Saeedi

**Supervisor**

Dr. Karim Faez

**September 2015**



Copyright © 2015 by Jamal Saeedi. All rights reserved. Reproduction  
by any means or translation of any part of this work is forbidden  
without permission of the copyright holder.

*To my beloved Rozita*

*To my father Saeed, my mother Shahrbanoo*

*and my sisters Zari and Roza.*

## **Acknowledgments**

Many thanks belong to my advisor and mentor, Dr. Karim Faez as well as the students at Tehran Polytechnic in Machine Vision Research Lab (MVRL) who helped so much with this research. Most of all, I wish to thank my amazing wife Rozita for being extremely patient and having so much faith in me. Thank you.

## **Abstract**

In this thesis, signal-processing issues of synthetic aperture radar (SAR) have been under consideration. Signal processing of SAR signal is a process of transforming the raw SAR signal into the gray level image. Specifically, we have focused on two topics in the field of SAR signal processing in this research consisting of nonlinear frequency modulation (NLFM) signal in SAR imaging, and phase error compensation using a new autofocus algorithm. In the first study, a new NLFM waveform is developed, which can be used as a transmitted chirp in SAR imaging to improve the imaging quality compared to LFM chirp signal. The new NLFM is constructed based on pricewise linear functions which is optimized using multi-objective optimization. Different signal prospecting algorithms including time domain correlation, back-projection, omega-k, and range-Doppler algorithm are investigated in order to use NLFM as the transmitted chirp in SAR system. In addition, a modified motion compensation algorithm using navigation data is proposed for frequency domain algorithm. Strip-map SAR geometry is considered to generate SAR raw signal for both point and distributed targets, in order to validate the new offered chirp signal and the proposed motion compensation algorithm. In the second study, a new autofocus algorithm is proposed for back-projection (BP) image formation of SAR imaging. The approach is based on maximizing an objective function obtained by prominent points in different sub-apertures of constructed SAR image by varying the flight trajectory parameters. While image-quality-based autofocus approach together with BP algorithm can be computationally intensive, we use approximations that allow optimal corrections to be derived. The approach is applicable for focusing different signal processing algorithms by obtaining modified flight trajectory parameters. Different examples demonstrate the effectiveness of the new autofocus approach applied to the frequency modulated continuous wave mode SAR dataset.

**Key Words:** Synthetic aperture radar; Non-linear frequency modulation; Back-projection algorithm; Autofocus algorithm; Stripmap imaging geometry; Phase error compensation.

# Table of Contents

<b>Acknowledgments.....</b>	<b>v</b>
<b>Abstract.....</b>	<b>vi</b>
<b>Table of Contents.....</b>	<b>vii</b>
<b>List of Figures .....</b>	<b>x</b>
<b>List of Tables .....</b>	<b>xiv</b>
<b>Acronyms .....</b>	<b>xv</b>
<b>Nomenclature .....</b>	<b>xviii</b>
<b>Chapter 1. Introduction .....</b>	<b>1</b>
<b>Chapter 2. Principle of synthetic aperture radar .....</b>	<b>8</b>
2.1 Definition.....	8
2.2 SAR history.....	9
2.3 Interpreting SAR image.....	12
2.4 SAR applications.....	14
2.5 SAR operation modes.....	16
2.6 Radar operation.....	19
2.6.1 SAR systems and hardware .....	19
2.6.1.1 Timing and control.....	19
2.6.1.2 Signal generation and transmit.....	20
2.6.1.3 Signal reception and data recording.....	21
2.6.1.4 Motion measurement .....	23
2.6.2 Pulsed SAR system .....	23
2.6.2.1 Pulse length .....	23
2.6.2.2 Range resolution and compression .....	24
2.6.3 Continuous wave SAR .....	25
2.6.3.1 Analog dechirp .....	25
2.6.3.2 Range resolution and compression .....	30
2.7 Moving platform .....	31
2.7.1 SAR imaging geometry and azimuth Resolution .....	32
2.7.2 Change in range and signal phase history .....	34
2.8 Basic signal processing for pulsed mode SAR .....	35
2.8.1 Range compression.....	36
2.8.2 Range cell migration correction.....	37

2.8.3 Azimuth compression .....	40
2.9 Summary.....	40
<b>Chapter 3. Problems definition and related review .....</b>	<b>42</b>
3.1 Introduction.....	42
3.2 Using of NLFM waveform in SAR imaging.....	46
3.3 Autofocus algorithm for flight trajectory optimization.....	50
3.4 Summary.....	52
<b>Chapter 4. SAR signal processing using NLFM .....</b>	<b>53</b>
4.1 Introduction.....	53
4.2 The proposed NLFM waveform .....	54
4.2.1 NLFM design based on PoSP .....	54
4.2.1.1 Cosine spectrum shape .....	57
4.2.1.2 Tangent-based waveform.....	58
4.2.1.3 Truncated Gaussian.....	58
4.2.1.4 Hybrid NLFM .....	59
4.2.2 New NLFM waveform using PWL functions.....	59
4.2.3 Parameters selection based on multi-objective optimization.....	61
4.3 SAR signal processing for NLFM chirp signal .....	65
4.3.1 Time domain correlation.....	67
4.3.2 Back-projection.....	68
4.3.3 Omega-K algorithm .....	69
4.3.4 Range-Doppler algorithm.....	72
4.4 Motion compensation algorithm for NLFM chirp signal .....	74
4.5 Summary.....	77
<b>Chapter 5. Autofocus algorithm based on flight trajectory optimization .....</b>	<b>79</b>
5.1 Introduction.....	79
5.2 LFM-CW synthetic aperture radar signal processing .....	80
5.2.1 Time domain signal processing algorithms.....	85
5.2.2 Frequency domain signal processing algorithm .....	86
5.3 Motion compensation using navigation data.....	88
5.3.1 Flight trajectory estimation using GPS data .....	88
5.3.2 Full motion compensation using flight trajectory information .....	90
5.4 Trajectory optimization for BP image formation .....	93
5.4.1 General autofocus model .....	93
5.4.2 Approximate model.....	98
5.4.3 Genetic optimization .....	101
5.5 Summary.....	103
<b>Chapter 6. Experimental results .....</b>	<b>104</b>
6.1 Comparison of the proposed NLFM with traditional waveforms.....	104
6.2 The proposed NLFM waveform in SAR scenario .....	106
6.3 The proposed MC algorithm in case of using NLFM waveform .....	112
6.4 The proposed autofocus algorithm.....	116

<b>Chapter 7. Conclusions and future works .....</b>	<b>126</b>
<b>References .....</b>	<b>131</b>
<b>Appendix .....</b>	<b>139</b>

# List of Figures

Figure 2.1: (a) Wiley's Patent, (b) Goodyear Aerospace appreciation of Carl Wiley.	10
Figure 2.2: Example of optically processed SAR image: SEASAT orbit 1149, 15 September 1978, showing area to the south of the Shetland Islands.	11
Figure 2.3: First digital SEASAT image, Trois Rivieres SEASAT scene, 40 hours processing time for 40×40 km scene. Featured in Aviation Week, Feb. 26, 1979	12
Figure 2.4: A sample SAR image from ERS with resolution of 12.5 m.	13
Figure 2.5: Geometry configurations in different SAR modes. <b>Stripmap</b> : Radar carrying the aircraft flies along the cross-range maintaining a fixed range. <b>Spotlight</b> : The radar carrying aircraft moves along a straight flight path while steering its main beam to constantly illuminate a specific ground patch. <b>Scan</b> : The antenna is scanned in range several times during a synthetic aperture. <b>Circular</b> : The aircraft carrying the radar flies around a scene of interest.	17
Figure 2.6: Basic SAR system block diagram [6].	20
Figure 2.7: Illustration of a side-looking SAR setup	22
Figure 2.8: SAR imaging geometry. The radar echo received at point $x_1$ was transmitted toward the target at point $x_2$ [6].	27
Figure 2.9: Simplified spectrogram of the SAR data (top) and the dechirped data (bottom) showing the effects of dechirping [6].	30
Figure 2.10: SAR imaging geometry for discussion of azimuth resolution.	33
Figure 4.1: Frequency modulation signal for $n + 1$ stages PWL functions.	61
Figure 4.2: Geometrical representation of the goal attainment method [59].	65

Figure 4.3: Proposed NLFM waveform using 64 parameters ( $n = 32$ ) (left), and MF output (right).	65
Figure 4.4: (a) SAR geometry, and (b) normal plane of the ideal trajectory.	75
Figure 5.1: (a) Stripmap SAR geometry, (b) Normal plane of the ideal trajectory.	89
Figure 5.2: (a) A sample of 10 Hz GPS data for 10 seconds flight, (b) corresponding flight trajectory, and (c) flight trajectory after fitting 10-order polynomial functions.	91
Figure 5.3: Range-compressed data with nadir return at top of the image (slant range extends from the top of the image).	92
Figure 5.4: Block diagram of the proposed autofocus for BP algorithm using navigation and SAR raw data.	94
Figure 5.5: Top row: (left) degraded, and (right) focused SAR image, bottom row, azimuth profiles of point targets highlighted in white circles.	97
Figure 5.6: Graphical representation of forming the sub-images in different sub-apertures using BP algorithm.	98
Figure 5.7: Flowchart of the proposed autofocus method.	99
Figure 5.8: Graphical representation of the proposed autofocus algorithm.	101
Figure 6.1: Doppler sensitivity results of different NLFM waveforms, left to right: SPLR, ISLR and IRW of pulse compression results versus Doppler shift.	106
Figure 6.2: Comparison of different time domain algorithms in different scenarios. Top row, left to right: TDC results with LFM, LFM+windowing and NLFM, bottom row: BP algorithm results.	110
Figure 6.3: Comparison of different frequency domain algorithms in different scenarios. Top row, left to right: RDA results with LFM, LFM+windowing and NLFM, bottom row: omega-K algorithm results.	110
Figure 6.4: Comparison of different NLFM waveforms used in SAR scenario with point target. From top left, clockwise: Cosine, $n = 1$ [12], Tangent-based [13], Hybrid	111

NLFM [15], and the proposed NLFM.

Figure 6.5: A real SAR image used to simulate raw data (this SAR image shows an area of the sea near a busy port). 112

Figure 6.6: Results of distributed target analysis, from top left, clockwise: TDC, BP, RDA, and omega-K algorithms. 113

Figure 6.7: Nominal trajectory versus real trajectory used in simulation. 114

Figure 6.8: MC results. Top row, left to right: Amplitude image obtained in ideal case, without MC, traditional MC [24], and proposed MC. Bottom row: contour image of logarithmic scale for better visual comparison. 114

Figure 6.9: MC results. from top left, clockwise: Amplitude image obtained in ideal case, without MC, traditional MC [24], and proposed MC. 115

Figure 6.10: Left: Photograph of antennas mounted on a helicopter, and right: SAR system hardware. 117

Figure 6.11: A sample SAR image (a) without MC, (b) MC with navigation data, and (c) the proposed autofocus. Middle row: Magnified images highlighted by white rectangles. Bottom row: Azimuth profiles of selected point targets highlighted by white circles. 118

Figure 6.12: A sample SAR image (a) without MC, (b) MC with navigation data, and (c) the proposed autofocus. Middle row: Magnified images highlighted by white rectangles. Bottom row: Azimuth profiles of selected point targets highlighted by white circles. 120

Figure 6.13: Azimuth profiles of selected point targets in different scenarios highlighted by white circles in (a) Figure 6.11, and (b) Figure 6.12. 121

Figure 6.14: A sample SAR image (a) without MC, (b) MC with navigation data, and (c) the proposed autofocus. Bottom row: Magnified images highlighted by white rectangles. 122

Figure 6.15: Left: Photograph of a microASAR system mounted on a small UAS, and right: SAR system hardware. 124

Figure 6.16: A sample SAR image (a) without MC, (b) MC with navigation data, and 125  
(c) the proposed autofocus. Bottom row: Magnified images highlighted by white  
rectangles.

## List of Tables

Table 6.1: Key simulation parameters.	105
Table 6.2: Results of pulse compression of different NLFM waveforms.	105
Table 6.3: SAR system parameters for raw data simulation	107
Table 6.4: Results of point target analysis, for the time domain signal processing algorithms.	108
Table 6.5: Results of point target analysis, for the frequency domain signal processing algorithms.	109
Table 6.6: Results of MC experiment for point target.	115

## Acronyms

CRT	Line-scan cathode-ray tube
PoSP	Principle of Stationary Phase
RCMC	Range Cell Migration Correction
BP	Back Projection
ECM	Electronic Counter Measures
$\omega - k$	Omega-K
FPGA	Field programmable gate arrays
JPL	Jet Propulsion Laboratory
PRI	Pulse repetition interval
FFT	Fast Fourier transform
DDS	Direct digital synthesizer
PWL	Piecewise linear functions
MC	Motion Compensation
EW	Electronic warfare
PSD	Power spectral density
QPE	Quadrature Phase Error

GA	Goal attainment
SAR	Synthetic aperture radar
ISAR	Inverse SAR
MA	Multiple Aperture
NASA	National Aeronautics and Space Administration
GPS	Global Positioning System
UAS	Unmanned aircraft systems
MTI	Moving Target Indication
CCD	Coherent Change Detection
IRW	Impulse response width
RCS	Radar cross section
PRF	Pulse Repetition Frequency
RF	Radio Frequency
RC	Range Compression
SRC	Secondary Range-Compression
PGA	Phase Gradient Autofocus
MF	Matched filter
RDA	Range-Doppler Algorithm
GA	Genetic algorithm

PFA	Polar Format algorithm
CSA	Chirp Scaling Algorithm
FSA	Frequency Scaling Algorithm
RMA	Range Migration Algorithm
A/D	Analog to digital converter
LFM	Linear frequency modulated
NLFM	Non-linear frequency modulation
FMCW	Frequency modulated continuous wave
EV	Eigenvector
SPLR	Sidelobe peak level ratio
ISLR	Integrated sidelobe level ratio
PP	Prominent points
VCO	Voltage controlled oscillator
IMU	Inertial Measurement Unit (IMU)
GPU	graphic processor units
TDC	Time domain correlation

## Nomenclature

$t$	Fast time
$f_0$	Frequency at the beginning of the chirp
$k_r$	Chirp rate
$\phi$	Starting phase
$\tau$	The two-way time of flight to the target
$R$	Range to target
$c_0$	The light speed
$t_p$	Pulsewidth
BW	Bandwidth
$\eta$	Slow time
$s_r$	Received signal
$s_t$	Transmitted signal
$s_{dc}$	Dechirped signal
$\Delta R$	Resolution in range direction
$f_s$	Sampling frequency
$l_{az}$	Real antenna length in azimuth direction
$\lambda$	Wavelength
$\theta_a$	Antenna beamwidth
$\Delta z_{ra}$	Resolution in azimuth direction for a single radar

$H$	Flight altitude
$v$	Platform velocity
$f_d$	Doppler frequency
$S$	Synthetic aperture time
$\Delta f_d$	Doppler frequency resolution
$\Delta z$	Resolution in azimuth direction for synthetic aperture radar
$\phi_{ex}$	Expected phase
$R_0$	Range in closest approach to target
$f_r$	Range frequency
$f_\eta$	Azimuth frequency
$T_g(f)$	Group delay function
$f(t)$	Instantaneous frequency
$\phi(t)$	Instantaneous phase
$G_i$	Goal
$F_i$	Objective function
$c(x)$	Nonlinear inequality constraint
$ceq(x)$	Linear inequality constraint
$w$	Weighting vector
$\varphi(t)$	Phase function for NLFM signal
$A(t)$	Signal amplitude
$p_r(t)$	Compressed pulse envelope in the range direction
$p_a(t)$	Compressed pulse envelope in the azimuth direction

# Chapter 1. Introduction

Synthetic Aperture Radar (SAR) can produce high-resolution imagery of a wide area using a small antenna and a large bandwidth. Taking advantage of the motion of the radar platform (usually an aircraft or spacecraft), a very large aperture is computationally synthesized using the data recorded from the radar echoes of a series of radar transmissions. This large synthetic aperture provides fine resolution in the direction of motion while a large bandwidth provides fine resolution in range.

SAR applications assist both the civilian and military subdivisions. Examples of SAR applications include [1]: Reconnaissance, surveillance, and targeting, treaty verification and nonproliferation, interferometry, foliage and ground penetration, navigation and guidance, moving target indication, change detection, and environmental monitoring. The ability to produce images in day or night under all weather conditions is the most important feature of SAR.

As SAR processing algorithms have been developed, certain assumptions and approximations have been made that match specific SAR scenarios (i.e., system parameters and/or requirements of the application). All SAR processing algorithms make approximations; the more general algorithms make fewer assumptions and are applicable in more circumstances, often at the cost of an increased processing load. For many SAR processing algorithms, the assumptions and approximations may be invalidated if the data is collected from a SAR system that is operating with very different parameters, such as frequency, bandwidth, beamwidth, squint, platform, or

range. Attempting to use a specialized algorithm when the approximations are not valid can result in degraded performance or even failure to produce an image.

A short review of major SAR processing algorithms is given in this chapter. The most commonly used SAR processing method is the range-Doppler algorithm (RDA) [2]. It was developed in the mid 1970's for processing data from JPL's SEASAT SAR. It efficiently focuses the data in both range and azimuth using frequency domain operations. One drawback is a computationally costly interpolation to correct the range-cell migration. Another limitation is the inability to handle squint-mode or wide-beam SAR. However, there is a modification to the RDA that can help in these cases by introducing a secondary range-compression (SRC). The SRC accounts for an additional term of a Taylor series approximation, but only at a reference range [2].

The chirp-scaling algorithm (CSA) was developed to eliminate the interpolation used for range-cell migration correction (RCMC) in the RDA [2]. The CSA employs a two-step scaling process to shift the target trajectories (a differential shift and a bulk shift), removing the RCM. Like the RDA, the CSA neglects the range-dependence of the SRC and all the higher order terms from the Taylor series approximation, limiting its utility for high squint and wide beamwidth SARs. The frequency-scaling algorithm (FSA) is related to the CSA, but it works with dechirped SAR data. The FSA has the same limitations as the CSA.

A third processing method has its origins in seismic processing and is known as the omega-K algorithm ( $\omega$ -K) [2] or range migration algorithm (RMA) [3]. The  $\omega$ -K directly processes the data in the two-dimensional frequency domain (wavenumber domain) without approximations in the signal model. The SAR data is compensated for a single reference range, and then a Stolt interpolation (which is computationally costly) compensates for the other ranges in the image. Because there are no approximations in deriving the signal model, the algorithm is suitable for very wide beamwidths or high squint. The drawback is that with all the processing done in the wavenumber domain, there is no opportunity for implementing range-dependent compensation for non-ideal platform motion.

The most general and computationally costly algorithm is known as back-projection (BP) [20]. Each pulse is firstly range-compressed in BP algorithm, and then the distance between each pulse location to each pixel in the final image is obtained. The range-compressed pulse is multiplied by the expected phase for that range and is summed across the entire pulses. Accordingly using the BP algorithm any beamwidth, squint, or translational motion can be exactly compensated. The benefits of BP include the simplicity of the algorithm, the parallel computation structure, and the ability to process data from an arbitrary platform path. Using the parallel nature of the algorithm and the parallel processing of modern general-purpose graphic processor units can significantly improve the processing time [5].

Other algorithms have been developed for specific applications. The polar format algorithm [2] is an older method for compensating for the range cell migration in spotlight SAR imaging. The SPECAN algorithm is designed to provide quick-look SAR imagery of lower quality with less processing time. In addition, the SPECAN algorithm can be used together with an imaging mode called Scan-SAR, where the antenna beam scans outward during each pulse to increase the swath width. Another older algorithm for SAR processing is called Doppler beam sharpening, in which signal returns are placed in individual Doppler bins, and then processed to form an image.

In this dissertation, different issues in the field of SAR signal processing are investigated. The overall objective of this research in the area of SAR signal processing in the present study is to propose different approaches to improve the quality of image formed by raw data. Specifically, we have focused on two different topics in the field of SAR signal processing in this research consisting of nonlinear frequency modulation (NLFM) signal in SAR imaging, and phase error compensation using a new autofocus algorithm.

The first research topic in this dissertation is concerned about using NLFM signal in SAR imaging. To aim this a new NLFM waveform is developed, which can be used as a transmitted chirp in SAR imaging to improve the imaging quality compared to LFM chirp signal. The new NLFM is constructed based on piecewise linear functions

which is optimized using multi-objective optimization. Different signal prospecting algorithms including time domain correlation, back-projection, omega-k, and range-Doppler algorithm are investigated in order to use NLFM as the transmitted chirp in SAR system.

Generally, SAR systems can be divided into two different modes: pulsed and continuous wave (CW). In CW SAR mode, the pulse duration or pulse width is higher than pulsed mode SAR. In addition, a technique called de-chirping or de-ramping is used in CW SAR in contrast with pulsed mode SAR [6]. Its principle is that if a LFM signal is de-chirped then the Matched filter (MF) of signal degenerates into a Fourier transform of the de-chirped result. This is only true for LFM waveforms. No similar methods for NLFM waveforms have been reported in the literature. Therefore, we cannot use NLFM waveform in the CW mode SAR and it is beyond the scope of this paper.

The second research topic, which is considered in this thesis, is autofocus algorithm. The automatic estimation and compensation of phase errors in SAR image formation using the information in raw data is referred as autofocus algorithm. Going forward through this research, a new autofocus algorithm is proposed for BP image formation of SAR imaging. Conventional autofocus methods are applicable for the frequency domain data processing algorithms such as RDA, and FSA, and cannot be applied by BP image formation method. The BP image formation algorithm places few limitations on SAR imaging; therefore, it is desirable to have an autofocus algorithm that is likewise unconstrained. This paper presents an autofocus method that is accordant with BP. The proposed approach is based on maximizing an objective function obtained by prominent points in different sub-apertures of constructed SAR image by varying the flight trajectory parameters. While image-quality-based autofocus approach together with BP algorithm can be computationally intensive, we use approximations that allow optimal corrections to be derived.

Constructions of very small SAR systems are possible by using a linear frequency modulated continuous wave (LFM-CW) signal in the radar transmitter [7-12]. Combined with an analog dechirp in the receiver, these systems can be made with

hardware which is simpler, cheaper, and consumes less power than the conventional pulsed SAR systems. This enables the use of low cost SARs on small-unmanned aircraft systems (UAS), which makes possible SAR imagery to be obtained in harsh climates or in environments too dangerous for manned aircraft or expensive SAR systems. The motion error problem is particularly apparent to the UAS SAR, because it is easily disturbed by the atmospheric turbulence due to its small size and lightweight. Moreover, the UAS SAR may not be equipped with a highly accurate navigation system due to weight capacity restriction [13]. Therefore, for the UAS SAR imaging, MC strategies are important and advisable based on the raw data or autofocus. For this reason, we have considered SAR in LFM-CW mode for theoretical discussions of the second research in this thesis; however, it can be generalized for pulsed mode SAR.

During this study, we were able to acquire special achievements in relation to the subject of synthetic aperture radar signal processing. These achievements are summarized in this section:

- Conceptual and system design of SAR in different functional modes consisting of pulsed and CW modes is accomplished and localized manufacturing capability of synthetic aperture radar has been created in the country.
- Raw signal simulation based on points and the distributed targets for different operating modes is performed. Since the SAR raw signal simulation for the distributed targets has high computational cost, ability to use special hardware such as graphics processing unit (GPU) for implementation as parallel processing has been created.
- A new NLFM waveform based on piecewise linear functions has been proposed for improving the MF response in SAR imaging.
- Different signal prospecting algorithms including time domain correlation, back-projection, omega-k, and range-Doppler algorithm are investigated in order to use NLFM as the transmitted chirp in SAR system.

- A modified motion compensation algorithm using navigation data is proposed for phase error compensation due to translational motion of SAR platform.
- Lastly, a new autofocus algorithm is presented for BP image formation for remaining phase error compensation in SAR signal.

The following conference and journal papers are published throughout of this research:

1. J. Saeedi, K. Faez, “Non-linear Frequency Modulation Using Piecewise Linear Functions for Synthetic Aperture Radar Imaging,” *10th European Conference on Synthetic Aperture Radar*, Berlin, Germany, pp. 1-4, 2014
2. J. Saeedi, K. Faez, “A back-projection autofocus algorithm based on flight trajectory optimization for synthetic aperture radar imaging,” *Multidimensional Systems and Signal Processing*, pp. 1-21, December 2014.
3. J. Saeedi, K. Faez, “Synthetic Aperture Radar Signal Processing Using Nonlinear Frequency Modulation Chirp signal,” *IEEE transactions on aerospace and electronic Systems*, 52 (1), pp. 1-12, February 2016.

The remainder of this thesis is organized as follows: Chapter 2 gives the background necessary to understand the research of this thesis. This background consists of a short history of SAR, principle of its operation, hardware components and SAR operating modes including pulsed SAR and continuous wave SAR. Then, the importance of platform motion is discussed, including the SAR imaging geometry, and the motion-induced signal phase history. Finally, basic SAR processing is discussed.

In Chapter 3, problems definition and an overview of the various algorithms and issues related to them is presented.

In Chapter 4, the first research topic in this dissertation will be discussed. First, description of the new NLFM chirp signal using PWL functions is presented. Then, SAR Signal processing for NLFM chirp as transmitting signal in SAR system is

explained and the theoretical discussion is provided. Finally, an improved motion compensation (MC) algorithm based on navigation information for NLFM waveform is explained.

The second study in this thesis, which is about an autofocus method for BP algorithm will be described in Chapter 5. First, the fundamental of SAR signal processing in LFM-CW mode and BP algorithm are briefly reviewed. Then, the phase error due to non-ideal motion of SAR platform along with the description of the MC using navigation data will be presented. Finally, the proposed autofocus algorithm based on flight trajectory optimization for BP image formation is presented.

Chapter 6 illustrates experimental results and different comparisons. At first, the proposed NLFM waveform is compared with traditional waveforms. Then, the results of signal processing using different image formation algorithms in disparate scenarios are provided. Finally, the results of the proposed autofocus algorithm are examined. It should be mentioned that in this chapter, both synthetic raw SAR data and real data are used to evaluate different algorithms.

Finally, conclusions and suggestions for future works are given in Chapter 7.

## Chapter 2. Principle of synthetic aperture radar

In the present study in the thesis, the issues about SAR signal processing will be discussed. SAR signal is actually radar echoes, which is sampled by an analog to digital converter. This raw signal is converted to a gray level image of illuminated area using appropriate image formation algorithms.

To provide a better understanding of SAR signal processing, an introduction to SAR is provided in this chapter. At first, a short history of SAR, SAR image interpretation, applications, and different functional modes will be explained. Then, an overview is given of the radar operation, introducing hardware components and system parameters crucial to any SAR processing theory. Two SAR operating modes, pulsed SAR and continuous wave SAR, are compared and contrasted. The importance of platform motion is discussed, including the SAR imaging geometry, and the motion-induced signal phase history. Finally, basic SAR processing is discussed including range compression, range cell migration correction, and azimuth compression.

### 2.1 Definition

SAR is a form of radar whose defining characteristic is its use of relative motion, between an antenna and its target region, to provide distinctive long-term coherent-signal variations. SAR is one of the powerful technics use for improve the azimuth resolution, the target stay in view of the antenna for a significant amount of time and observe by the radar from numerous locations along the platform path.

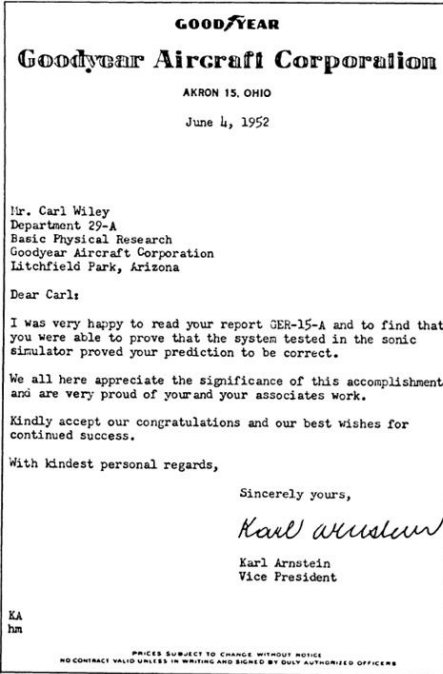
SAR can produce high-resolution imagery of a wide area using a small antenna and a large bandwidth. Taking advantage of the motion of the radar platform (usually an aircraft or spacecraft), a very large aperture is computationally synthesized using the data recorded from the radar echoes of a series of radar transmissions. This large synthetic aperture provides fine resolution in the direction of motion while a large bandwidth provides fine resolution in range.

The increased usage of SAR in the remote sensing community is based upon three main principles: 1) A radar carries its own illumination, so it works equally well in darkness. 2) The electromagnetic waves of common radar frequencies pass through clouds and precipitation with little or no deterioration. 3) The radar energy scatters off materials differently from optical energy, providing a complementary and sometimes better discrimination of surface features than optical sensors.

## 2.2 SAR history

Radar was originally developed for military purposes during World War II. Its initial purpose was to track aircraft and ships through heavy weather and darkness. It has experienced a steady growth, with advances in radio frequency (RF) technology, antennas, and, more recently, digital technology [14]. The original radar systems measured range to a target (radar scatterer) via time delay, and direction of a target via antenna directivity. It was not long before Doppler shifts were used to measure target speed. Then it was discovered that the Doppler shifts could be processed to obtain fine resolution in a direction perpendicular to the range or beam direction.

Through this latter concept, often credited to Carl Wiley of Goodyear Aerospace in 1951 [15], it was found that two-dimensional images could be made of the targets and of the Earth's surface using radar. The method was termed SAR, referring to the concept of creating the effect of a very long antenna by signal analysis. Fig. 2.1 shows the first page of Wiley's Patent, and Goodyear Aerospace appreciation of Carl Wiley.



(a)



(b)

Figure 2.1: (a) Wiley's Patent, (b) Goodyear Aerospace appreciation of Carl Wiley.

The first SAR processing was done optically. The processing system was precisely designed to work with a single SAR system operating at a single set of SAR parameters. During data collection, the radar signal returns modulated the intensity of a line-scan cathode-ray tube (CRT). The output of the CRT was imaged through a lens onto a moving filmstrip. It was found that the focusing could be accomplished using laser beams and lenses using the principles of Fourier optics [16].

The received radar data were recorded on black and white film, and a laser beam was collimated and shone through the film. Lenses provided a real-time two-dimensional Fourier transform of the data, and diffraction gratings were used to focus the data. Optical SAR processors could produce a well-focused image, but required precise alignment of high-quality lenses on a large optical bench. Even though the processing was done in real time (apart from the film processing), a skilled operator was required to control image quality, and production was difficult to automate. In addition, the output film limited the dynamic range of the final image [17]. Example of optically processed SAR image is shown in Fig. 2.2.

The first space-borne SAR was carried by NASA's SEASAT satellite in 1978. This only lasted for three months, when a power supply fault caused its early demise, but in that time, it produced a wealth of data from land, ocean and ice surfaces. With the lead up to the SEASAT mission, a concentrated effort was made to develop digital SAR processors. The received radar data were digitized and stored on tape or disk. In the late 1970s, 256 KB of memory was considered large for computers, and disk capacity and transfer speeds were very modest by today's standards. Nevertheless, a digital SAR processor was built for SEASAT data in 1978, and it took 40 hours to process a 40x40 km image with 25-m resolution [18]. Today's computers can process the same data in a few tens of seconds, using desktop workstations. When digitally recording the data, the processing is more flexible, but algorithm development has continued to focus on specific radars or applications. The most commonly used SAR processing method is the RDA [2]. It was developed in the mid 1970's for processing data from JPL's SEASAT SAR. Fig. 2.3 shows the first digital SEASAT Image.

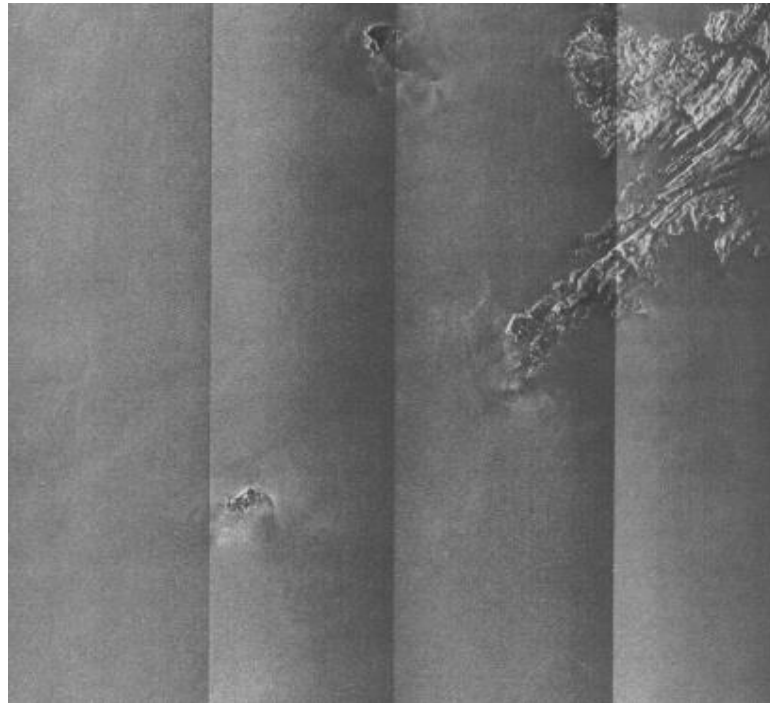


Figure 2.2: Example of optically processed SAR image: SEASAT orbit 1149, 15 September 1978, showing area to the south of the Shetland Islands.



**Seasat Imagery Shows St. Lawrence**

Digitaly processed image from National Aeronautics and Space Administration's Seasat-A synthetic aperture radar shows a portion of the St. Lawrence River near the city of Trois Rivières, Québec. The satellite passed overhead at an altitude of 800 km. (496 mi.) and the L-band radar antenna had a boresight angle of 20 deg. from the nadir. The data was recorded at the Shoe Cove, Newfoundland, satellite receiving station and was first processed last summer by MacDonald, Dettwiler & Associates Ltd., Richmond, British Columbia. The image covers an area 38 km. (22.6 mi.) along the river by 41 km. (25.5 mi.) with a resolution of 25 m. (82 ft.). The radar data was processed to four looks in azimuth and corrected for slant range distortion. Surface differences in water in both Lac St. Pierre (lower left) and the St. Lawrence River are evident—the smoother water is dark and rougher water is brighter. Several ships also can be seen (left center) west of the bridge spanning the river. Forests show as bright areas and tilled land as dark areas. Also evident are highways leading to the city (1), Canadian Pacific rail line (2), the city of Trois Rivières (3), the Côte de la Prairie where the St. Maurice River empties into the St. Lawrence (4) and the Gentilly nuclear power station (5). Digital processing of the synthetic aperture radar data results in images that are free from processor induced imperfections and artifacts, according to MacDonald, Dettwiler & Assoc. The process also results in magnetic tape that stores the image to the full dynamic range of the original radar data.

Figure 2.3: First digital SEASAT image, Trois Rivieres SEASAT scene, 40 hours processing time for 40×40 km scene. Featured in Aviation Week, Feb. 26, 1979

### 2.3 Interpreting SAR image

A single SAR image is usually displayed as a grey scale image, such as the one shown in Fig. 2.4. The intensity of each pixel represents the proportion of microwave backscattered from that area on the ground, which depends on a variety of factors: types, sizes, shapes, and orientations of the scatterers in the target area; moisture content of the target area; frequency and polarization of the radar pulses; as well as the incident angles of the radar beam. The pixel intensity values are often converted to a physical quantity called the backscattering coefficient or normalized radar cross-section measured in decibel (dB) units with values ranging from +5 dB for very bright objects to -40 dB for very dark surfaces.

Interpreting a radar image is not a straightforward task. It very often requires some familiarity with the ground conditions of the areas imaged. As a useful rule of



Figure 2.4: A sample SAR image from ERS with resolution of 12.5 m.

thumb, the higher the backscattered intensity, the rougher is the surface being imaged. Flat surfaces such as paved roads, runways, or calm water normally appear as dark areas in a radar image since most of the incident radar pulses are specularly reflected away. Calm sea surfaces appear dark in SAR images. However, rough sea surfaces may appear bright especially when the incidence angle is small. The presence of oil films smoothen out the sea surface. Under certain conditions when the sea surface is sufficiently rough, oil films can be detected as dark patches against a bright background.

Trees and other vegetation are usually moderately rough on the wavelength scale. Hence, they appear as moderately bright features in the image. The tropical rain forests have a characteristic backscatter coefficient of between -6 and -7 dB, which is spatially homogeneous and remains stable in time. For this reason, the tropical rainforests have been used as calibrating targets in performing radiometric calibration of SAR images.

Very bright targets may appear in the image due to the corner-reflector or double-bounce effect where the radar pulse bounces off the horizontal ground (or the sea) towards the target, and then reflected from one vertical surface of the target back to the sensor. Examples of such targets are ships on the sea, high-rise buildings, and regular metallic objects such as cargo containers. Built-up areas and many man-made features usually appear as bright patches in a radar image due to the corner reflector effect.

The brightness of areas covered by soil may vary from very dark to very bright depending on its roughness and moisture content. Typically, rough soil appears bright in the image. For similar soil roughness, the surface with a higher moisture content will appear brighter.

## 2.4 SAR applications

SAR applications benefit both the civilian and military sectors. One type of classification of SAR applications includes the following:

**Reconnaissance, Surveillance, and Targeting:** Many applications for synthetic aperture radar are for reconnaissance, surveillance, and targeting. These applications are driven by the military's need for all weather, day-and-night imaging sensors. SAR can provide sufficiently high resolution to distinguish terrain features and to recognize and identify selected man made targets.

**Treaty Verification and Nonproliferation:** The ability to monitor other nations for treaty compliance and for the nonproliferation of nuclear, chemical, and biological weapons is increasingly critical. Often, monitoring is possible only at specific times, when over flights are allowed, or it is necessary to maintain a monitoring capability in inclement weather or at night, to ensure an adversary is not using these conditions to hide an activity. SAR provides the all-weather capability and complements information available from other airborne sensors, such as optical or thermal-infrared sensors.

**Interferometry (3-D SAR):** Interferometric SAR data can be acquired using two antennas on one aircraft or by flying two slightly offset passes of an aircraft with a single antenna. Interferometric SAR can be used to generate very accurate surface profile maps of the terrain.

**Navigation and Guidance:** SAR provides the capability for all-weather, autonomous navigation and guidance. By forming SAR reflectivity images of the terrain and then "correlating" the SAR image with a stored reference (obtained from optical photography or a previous SAR image), a navigation update can be obtained. Position accuracies of less than a SAR resolution cell can be obtained. SAR may also be used to guidance applications by pointing or "squinting" the antenna beam in the direction of motion of the airborne platform.

**Foliage and Ground Penetration:** SARs offer the capability for penetrating materials which are optically opaque, and thus not visible by optical or IR techniques. Low-frequency SARs may be used under certain conditions to penetrate foliage and even soil. This provides the capability for imaging targets normally hidden by trees, brush, and other ground cover [19]. To obtain adequate foliage and soil penetration, SARs must operate at relatively low frequencies (10's of MHz to 1 GHz).

**Moving Target Indication:** The motion of a ground-based moving target such as a car, truck, or military vehicle, causes the radar signature of the moving target to shift outside of the normal ground return of a radar image. Different techniques are developed to automatically detect ground-based moving targets and to extract other target information such as location, speed, size, and Radar Cross Section (RCS) from these target signatures.

**Change Detection:** A technique known as coherent change detection offers the capability for detecting changes between imaging passes. To detect whether or not a change has occurred, two images are taken of the same scene, but at different times. These images are then geometrically registered so that the same target pixels in each image align. After the images are registered, they are cross-correlated pixel by pixel. Where a change has not occurred between the imaging passes, the pixels

remain correlated, whereas if a change has occurred, the pixels are uncorrelated. Of course, targets that are not fixed or rigid, such as trees blowing in the wind, will naturally decorrelate and show as having "changed." While this technique is useful for detecting change, it does not measure direction or the magnitude of change.

**Environmental Monitoring:** SAR is used for a wide variety of environmental applications, such as monitoring crop characteristics, deforestation, ice flows, and oil spills. Oil spills can often be detected in SAR imagery because the oil changes the backscatter characteristics of the ocean. Radar backscatter from the ocean results primarily from capillary waves through what is known as Bragg scattering (constructive interference from the capillary waves being close to the same wavelength as the SAR). The presence of oil dampens the capillary waves, thereby decreasing the radar backscatter. Thus, oil slicks appear dark in SAR images relative to oil-free areas. In the aftermath of a flood, the ability of SAR to penetrate clouds is extremely useful. Here SAR data can help to optimize response initiatives and to assess damages.

## 2.5 SAR operation modes

SAR can be operated in a number of different ways, sometimes with different systems, or sometimes as different modes within a single system. Some of the different modes of operation include:

**Stripmap mode:** In this mode, the antenna pointing direction is held constant as the radar platform moves. The beam sweeps along the ground at an approximately uniform rate, and a contiguous image is formed. A strip of ground is imaged, and the length of the strip is only limited by how far the sensor moves or how long the radar is left on. The azimuth resolution is governed by the antenna length. Fundamental Stripmap imaging geometry is shown in Fig. 2.5 [4].

**Scan mode:** This mode is a variation of stripmap SAR, whereby the antenna is scanned in range several times during a synthetic aperture. In this way, a much

wider swath is obtained, but the azimuth resolution is degraded (or the number of looks is reduced). The best azimuth resolution that can be obtained is that of the stripmap mode multiplied by the number of swaths scanned (Fig. 2.5).

**Spotlight mode:** The resolution of the stripmap mode can be improved by increasing the angular extent of the illumination on the area of interest (a spot on the ground). This can be done by steering the beam gradually backwards as the sensor passes the scene. The beam steering has the transient effect of simulating a wider antenna beam (i.e., a shorter antenna). However, the antenna must ultimately be steered forward again, and a part of the ground is missed. This means that the

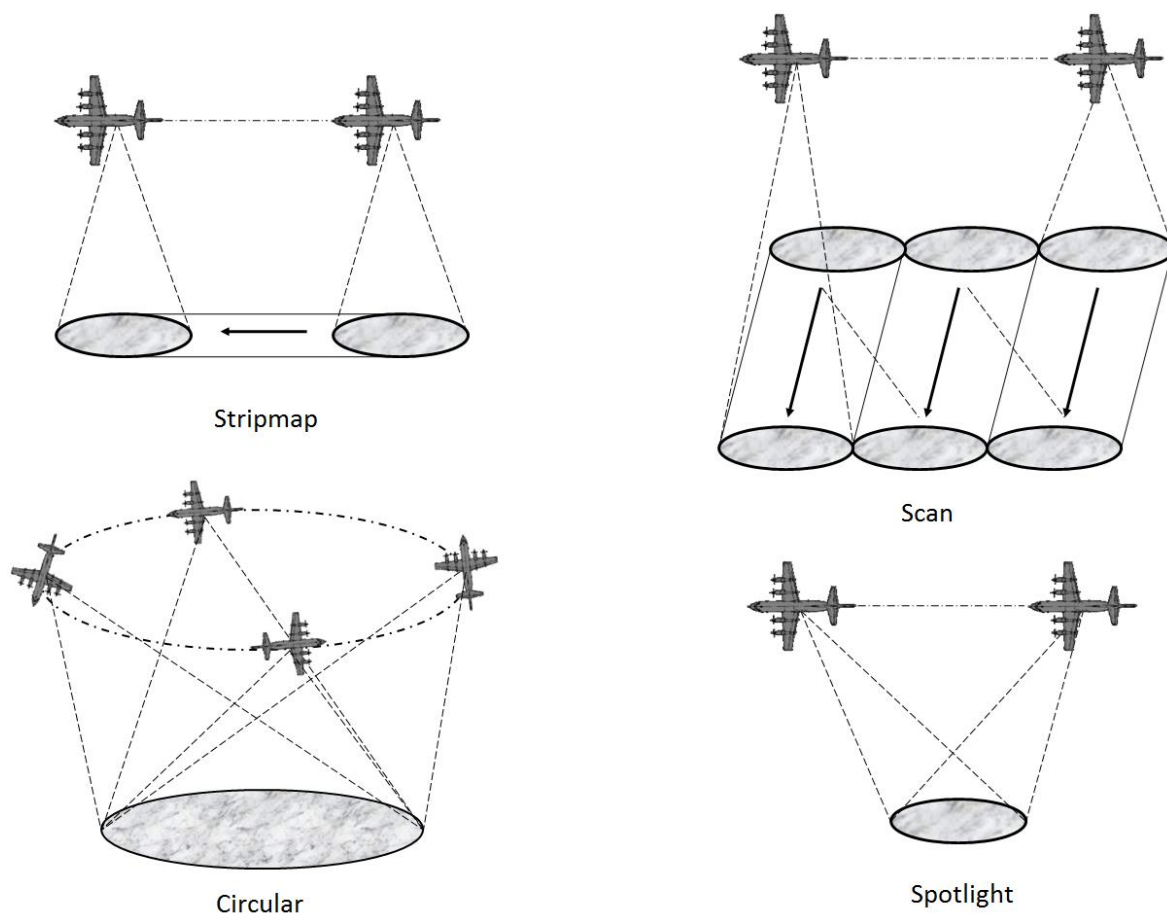


Figure 2.5: Geometry configurations in different SAR modes. **Stripmap:** Radar carrying the aircraft flies along the cross-range maintaining a fixed range. **Spotlight:** The radar carrying aircraft moves along a straight flight path while steering its main beam to constantly illuminate a specific ground patch. **Scan:** The antenna is scanned in range several times during a synthetic aperture. **Circular:** The aircraft carrying the radar flies around a scene of interest.

coverage is not contiguous-only one spot on the ground is imaged at a time. SAR spotlight mode imaging geometry is shown in Fig. 2.5. Spotlight SAR data collection enables high resolution imaging capabilities.

**Circular SAR:** SAR data collection modalities such as stripmap, spotlight and Scan use a radar trajectory that is a straight flight path. These data collection modalities are known as linear SAR. SAR data collection using a circular flight path is known as circular SAR (CSAR). In CSAR, the radar moves around a circular flight path while steering its main- beam to constantly illuminate a specific ground patch. Antenna steering is accomplished either mechanically or electronically. CSAR data collection can be viewed as spotlight SAR data collection. However, the difference is that in CSAR the data is collected using a circular path while in spotlight SAR data is collected using a straight flight path.

**Inverse SAR:** So far, it has been assumed that the target is stationary and the SAR system is moving. However, SAR also works if the target is moving and the radar system is stationary. This reversal of roles leads to the term "Inverse SAR." An example is the tracking of satellites from a ground-based radar. The concept can be generalized to the case where both the target and the sensor are moving, such as a ship in heavy seas being imaged by an airborne or satellite SAR.

**Bistatic SAR:** This is a mode of SAR operation in which the receiver and the transmitter are at different locations. In remote sensing SARs, the receiver is usually at approximately the same location as the transmitter, which is referred to as monostatic.

**Interferometric SAR (InSAR):** This is a mode of SAR operation in which post-processing is used to extract terrain height or displacement from the complex images. Two complex SAR images acquired at the same spatial positions (differential InSAR) or slightly different positions (terrain height InSAR) over the same area are conjugate multiplied. The result is an interferogram with contours of equal displacement or elevations.

## 2.6 Radar operation

SAR is an active microwave remote sensing technique that produces wide-area images of high resolution. While passing by a target, the SAR illuminates the area with a series of coherent pulses. The series of radar echoes from the target area are digitized and processed to form the image. SAR complements optical imagery in a variety of applications and has a number of advantages. The radar is its own illumination source, thus it can operate equally well day or night. The choice of frequencies in the microwave band allows imaging through clouds, precipitation, dust, and smoke, and at the low-frequency end of the microwave spectrum, foliage and dry ground penetration are possible. The choices of SAR system parameters and hardware components are often driven by specific applications.

### 2.6.1 SAR systems and hardware

A basic SAR system consists of five main subsections as shown in Fig. 2.6. The subsections are timing and control, signal generation and transmission, signal reception and data recording, motion measurement and estimation, and image formation. The separate subsystems must work closely together for the SAR to operate correctly [6].

#### 2.6.1.1 Timing and control

To form an image, the SAR signal must be coherent over the entire series of pulses that make up a data collection. An important part of that is maintaining coherence and consistent timing between the separate subsystems that make up the SAR. The timing and control system maintains coherence from pulse to pulse and between subsystems, determines the timing for turning the radar on, off and for switching between transmit, and receive.

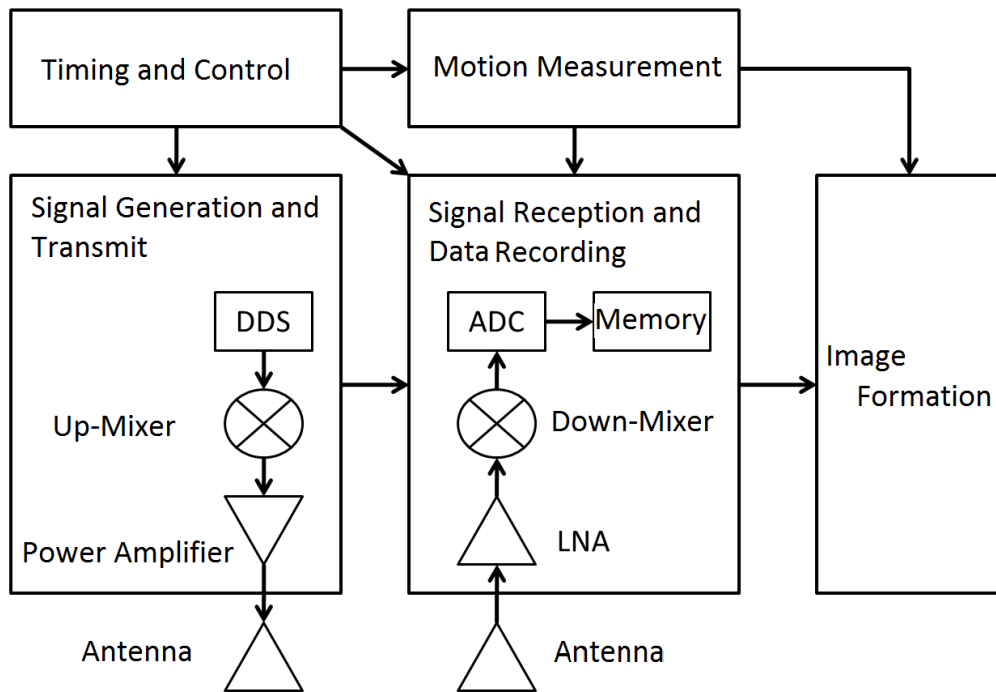


Figure 2.6: Basic SAR system block diagram [6].

### 2.6.1.2 Signal generation and transmit

Before the SAR signal is generated, a number of important system parameters are determined, including center frequency, bandwidth, pulse length, and pulse repetition frequency (PRF). The signal can be generated using a direct digital synthesizer (DDS) or a voltage controlled oscillator (VCO). A DDS allows a specific waveform to be generated from programmed digital controls. The most common SAR signal is a linear frequency modulated (LFM) chirp, where the signal spans the bandwidth over the pulse length, changing in frequency at a linear rate. This cycle is repeated at the PRF.

The SAR signal is usually generated at or near baseband and then mixed up to the desired operating frequency before transmission. A LFM transmit signal can be expressed:

$$s_t(t) = A(t) \exp(j(2\pi f_0 t + \pi k_r t^2 + \phi)) \quad (2.1)$$

where  $A(t)$  is the signal amplitude and, as a function of  $t$ , defines the pulse length with a rect function,  $f_0$  is the frequency at the beginning of the chirp,  $k_r$  is the chirp rate, and  $\phi$  is the starting phase which can usually be neglected.

In the transmission chain, a power amplifier increases the transmit power to a specified level. The transmitted signal needs to have enough power so that the signal-to-noise-ratio (SNR) is large enough to generate a quality image. SNR also depends on the specific imaging parameters, especially range to target and antenna beamwidth.

The antenna is designed with certain beamwidths in azimuth and elevation and can be pointed in different directions for different SAR imaging modes. Conventional side-looking SAR is illustrated in Fig. 2.7. In stripmap mode a fixed antenna pointing orthogonal to the motion of the platform is used; while for squint mode the antenna is pointed slightly forward or backward. In spotlight mode the antenna moves (mechanically using a gimbal or electronically using a phased array) to stay pointed at the center of the target area [20].

The beamwidth and antenna pointing determine the illuminated footprint on the ground. As the radar moves alongside the mapping area, chirp pulses are emitted at some constant PRF. The platform motion, the antenna pointing, and the antenna beamwidth determine the Doppler frequencies of the return signals from the targets in the illuminated area (the Doppler bandwidth). The maximum Doppler frequency cannot be greater than the Doppler bandwidth of the system, defined by the PRF, or else Doppler aliasing occurs.

### 2.6.1.3 Signal reception and data recording

The amplified signal transmitted through the antenna propagates to the target area. The propagation environment consists of the layers of atmosphere, usually approximated as free space, and the distributed scatterers that make up the target scene. A very small portion of the transmit signal is reflected back to the radar. The reflected signal from a point target can be expressed as:

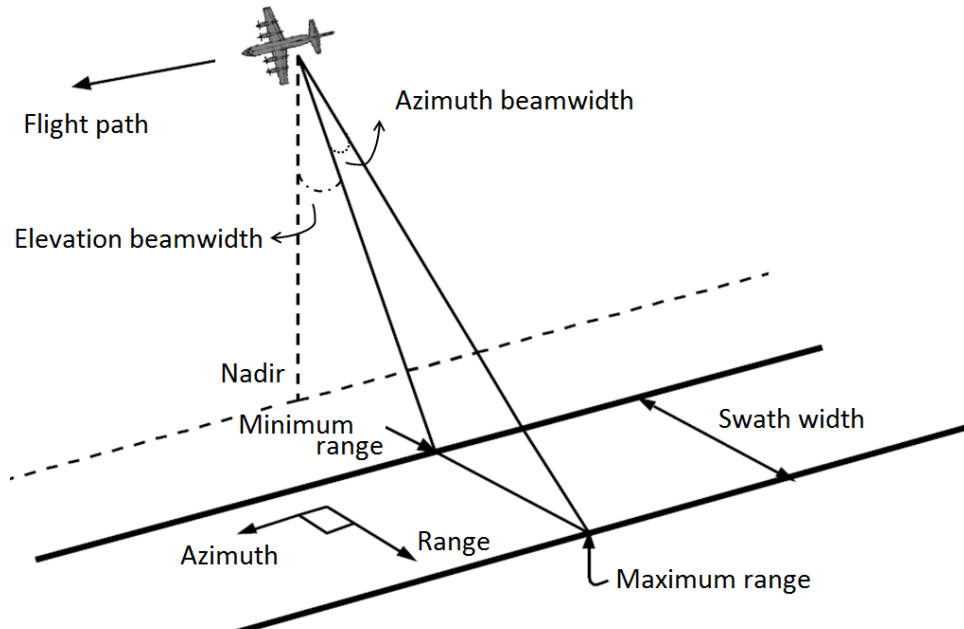


Figure 2.7: Illustration of a side-looking SAR setup

$$s_r(t) = A'(t) \exp\left(j(2\pi f_0(t-\tau) + \pi k_r(t-\tau)^2 + \phi)\right) \quad (2.2)$$

where  $A'(t)$  is an attenuated version of  $A(t)$ , and  $\tau$  is the two-way time of flight to the target at range  $R$ .

$$\tau = \frac{2R}{c_0} \quad (2.3)$$

where  $c_0$  is light speed.

The received signal is amplified with a low-noise amplifier (LNA) and mixed down to an appropriate band for sampling. One option for sampling is offset video with a single channel at a rate at least twice the bandwidth of the signal. Another option is quadrature demodulation to baseband with two channel I/Q sampling. After the signal from (2.2) is mixed down by a frequency,  $f_{md}$ , the signal ready to be recorded is:

$$\begin{aligned} s_{rm}(t) &= A''(t) \exp\left(j(2\pi f_0(t-\tau) - 2\pi f_{md} t + \pi k_r(t-\tau)^2 + \phi)\right) \\ &= A''(t) \exp\left(j(2\pi(f_0 - f_{md})t - 2\pi f_0 \tau + \pi k_r(t-\tau)^2 + \phi)\right) \end{aligned} \quad (2.4)$$

The first SAR systems recorded the data optically on film and used analog optical processing to produce the image. Modern SAR systems digitize the data and either store it on board, transmit it to a ground station, or process it on-board.

#### 2.6.1.4 Motion measurement

An important part of SAR data collection and processing that is not directly part of the radar is the motion measurement system [3]. SAR processing requires knowledge of the flight path during data collection, or at least an estimation of the flight path. Motion measurement systems used with the SAR systems can use a variety of methods including manually recording the velocity readings from the aircraft instrumentation during data collection, utilizing a low rate GPS solution inserted into the SAR data, and employing a high rate inertial measurement unit (IMU) coupled with GPS and carefully time-tagged and aligned with the collected SAR data. The better the motion measurements, the more accurately the SAR data can be processed to form a well-focused image.

### 2.6.2 Pulsed SAR system

The most common type of SAR transmits short pulses. This allows ample time to switch off the transmitter, turn on the receiver and reuse the transmit antenna as the receive antenna. For pulsed SAR there are several important factors to be considered in processing the data: the pulse length, the range resolution, and the method of range compression.

#### 2.6.2.1 Pulse length

The length of time that the SAR is transmitting is known as the pulse length,  $t_p$ . For a LFM chirp,  $t_p$  is related to the bandwidth and the chirp rate by:

$$\Delta R = \frac{c_0 \cdot \Delta t}{2} \quad (2.5)$$

For a given transmit power, a longer pulse produces a better SNR after range compression, but the cost is increased data volume. There are other factors that limit the pulse length, such as the maximum duty cycle of the power amplifier. The transmit duty cycle, expressed as the fraction of time that the power amplifier is on, is:

$$\text{Duty Cycle} = t_p \cdot PRF \quad (2.6)$$

The two-way time of flight to the nearest point of the area we desire to image also limits the pulse length. Before the return echo from this nearest point begins to arrive at the radar, we must allow time for the power down transient of the power amplifier and the power on transient of the receiver to stabilize. For very large ranges, such as imaging from a satellite, carefully timing the transmit and receive periods allows multiple pulses to be in transit to and from the target area at the same time.

### 2.6.2.2 Range resolution and compression

Range compression is performed via matched filtering the received signal with expected return signal, a copy of the transmit signal. Using this method, the return from a point target is compressed from a signal with length  $t_p$  to a focused point with a width equal to the range resolution. Range resolution is defined by the minimum distance separating targets for which the radar echoes can be separated. For a single frequency pulse of length  $\Delta t$  the spatial resolution is expressed as:

$$\Delta R = \frac{c_0 \cdot \Delta t}{2} \quad (2.7)$$

Spatial resolution can also be expressed in terms of the signal bandwidth. The bandwidth of an interrupted continuous-wave, or a single frequency pulse, is approximated  $BW = 1/\Delta t$ . The bandwidth for a modulated signal (such as the

LFM signal in our example) is the transmitted bandwidth. Typically, range resolution is expressed as:

$$\Delta R = \frac{c_0}{2 \cdot \text{BW}} \quad (2.8)$$

### 2.6.3 Continuous wave SAR

The pulse length is maximized when the SAR is continuously transmitting, or equivalently when a single pulse fills the entire pulse repetition interval (PRI). Maximizing the pulse length maximizes the SNR for a given transmit power. This requires bistatic operation, one antenna to continuously transmit and another antenna to continuously receive.

One problem with this is that the direct feed-through from the transmitter to the receiver can have much higher power than the radar echoes from the target area. This feed-through must be managed to prevent it from drowning out the desired signal. Various methods have been developed for accomplishing this task. One method involves an analog dechirp in the receive chain. This dechirp converts the feed-through to a single frequency that can be filtered out in hardware. The analog dechirp also offers some other advantages particularly useful for CW SAR: a reduced sampling bandwidth and a simplified range compression computation.

#### 2.6.3.1 Analog dechirp

With an analog dechirp, the received signal is mixed with a copy of the transmit signal. The dechirp signal can be a synchronous copy of the transmit signal (for direct dechirp) or a delayed version. The frequency of the LFM-CW signal increases from a starting frequency  $f_0$ , and spans the bandwidth BW, at the chirp-rate  $k_r = \text{BW} \cdot \text{PRF}$ . This cycle is repeated at the PRF, giving a PRI equal to the pulse length,  $t_p$ . The transmitted up-chirp signal can be expressed in the time domain, where  $t$  is fast time and  $\eta$  is slow time, as:

$$s_t(t, \eta) = \exp\left(j\left(2\pi f_0 t + \pi k_r t^2 + \phi\right)\right), \quad (2.9)$$

where  $\phi$  is the initial phase.

At time  $t$ , the radar is also receiving the reflected signal transmitted at time  $t - \tau$ , where  $\tau$  is the two way time of flight to a target.  $\tau$  is calculated using the range to target, which is different from time  $t$  and time  $t - \tau$  due to the constant motion of the aircraft. Using the slant range geometry shown in Fig. 2.8, we assign  $x_1$  to the location of the radar at time  $\eta + t$ , and  $x_2$  to the location at  $\eta + t - \tau$ , where  $\eta$  is slow-time. The calculation of  $\tau$  is complicated by the motion of the aircraft, but can be approximated.

In order to precisely determine  $\tau$ , we define a point,  $x_h$  approximately half way between  $x_1$  and  $x_2$ .

$$x_h = x_2 + \frac{R_2}{c_0} v = x_1 - \frac{R_1}{c_0} v \quad (2.10)$$

where  $v$  is platform speed, and  $R_1$  and  $R_2$  are the distances to the target from points  $x_1$  and  $x_2$  respectively, defined as:

$$R_2 = \sqrt{R_0^2 + x_1^2} \quad (2.11)$$

$$R_1 = \sqrt{R_0^2 + x_2^2} \quad (2.12)$$

We also know that  $x_1 = (\eta + t) \cdot v$ , from which we know  $R_1$ . That leaves us with unknowns  $x_2$  and  $R_2$ , which are obtained as:

$$x_2 = \frac{-v^3 \cdot R_1}{c_0 \cdot c_0^2 - v^2} + \frac{v^2 \cdot x_1}{c_0^2 - v^2} + x_1 - \frac{R_1 \cdot v - \frac{v \cdot \sqrt{-v^2 R_0^2 c_0^2 + c_0^4 R_0^2 - 2c_0^3 x_1 R_1 v + c_0^2 R_1^2 v^2 + c_0^4 x_1^2}}{c_0 \cdot c_0^2 - v^2}}{c_0 \cdot c_0^2 - v^2} \quad (2.13)$$

and now  $\tau$  can be calculated as follows:

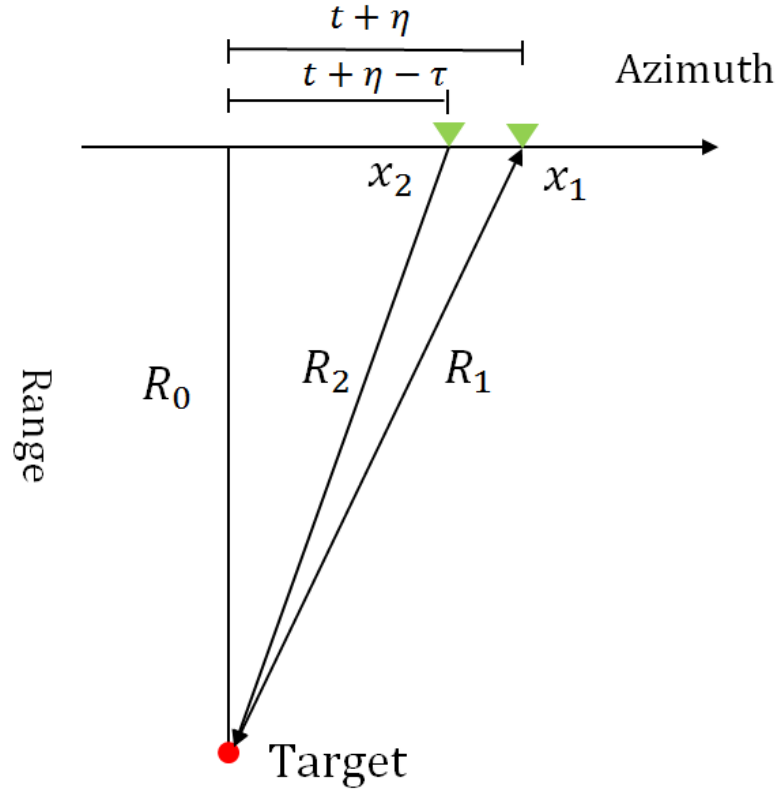


Figure 2.8: SAR imaging geometry. The radar echo received at point  $x_1$  was transmitted toward the target at point  $x_2$  [6].

$$\tau = \frac{R_1 + R_2}{c_0} \quad (2.14)$$

A very close approximation is to assume that the ranges  $R_1$  and  $R_2$  are the same (for spaceborne SAR they can differ by as much as several meters, but for airborne applications they only differ by at most a few millimeters, and much less than that for low altitude operation), thus the expression for  $\tau$  can be simplified to  $\tau = 2R(t, \eta)/c_0$  where  $R^2(t, \eta) = R_0^2 + v^2(t + \eta)^2$  and  $R_0$  is the range of closest approach to the target.

Going forward with this approximation, the received signal from a target at range  $R$ , with time delay  $\tau$  is:

$$s_r(t, \eta) = \exp\left(j\left(2\pi f_0(t - \tau) + \pi k_r(t - \tau)^2 + \phi\right)\right) \quad (2.15)$$

The transmit signal is mixed with the received signal and low-pass filtered in hardware, which is mathematically equivalent to multiplying (2.9) by the complex conjugate of (2.15). This results in the dechirped signal:

$$s_{dc}(t, \eta) = s_t \cdot s_r^* = \exp\left(j(2\pi f_0 t + 2\pi k_r t \tau - \pi k_r \tau^2)\right) \quad (2.16)$$

Alternatively, the return signal is mixed with a copy of the transmit signal delayed by  $d$ :

$$s_{td}(t, \eta) = \exp\left(j(2\pi f_0(t-d) + \pi k_r(t-d)^2 + \phi)\right) \quad (2.17)$$

The dechirped signal can then be expressed by multiplying (2.17) by the complex conjugate of (2.15), resulting in:

$$s_{dc}(t, \eta) = s_{td} \cdot s_r^* = \exp\left(j(2\pi f_0(\tau-d) + 2\pi k_r t(\tau-d) - \pi k_r(\tau^2 - d^2))\right) \quad (2.18)$$

The result of dechirping is a frequency difference between the signals. For direct dechirp, this frequency difference,  $\Delta f$ , corresponds directly to the distance from the target (the target range),

$$\Delta f = \frac{2Rk_r}{c_0} \quad (2.19)$$

Or for a delayed dechirp, with delay  $d$ ,

$$\Delta f = \left(\frac{2R}{c_0} - d\right) \cdot k_r \quad (2.20)$$

The dechirping operation also reduces the signal bandwidth from the full transmit bandwidth to a dechirped bandwidth determined by the maximum range of interest, or the width of the bandpass filter. This dechirped bandwidth is:

$$BW_{dc} = \frac{2R_{\max}k_r}{c_0} \quad (2.21)$$

for a direct dechirp, or for a delayed dechirp,

$$BW_{dc} = \frac{2R_{\max}k_r}{c_0} - d \cdot k_r = \frac{2R_{\max}k_r}{c_0} - \frac{2R_{\min}k_r}{c_0} \quad (2.22)$$

where  $R_{\max}$  is the maximum range that can be imaged and  $R_{\min}$  is the minimum range.

A delayed dechirp shifts more ranges into the sampling bandwidth, allowing for a wider swath. The delay is set to the nearest range desired in the image - the frequencies increase with range from that point. In this way, none of the sampling bandwidth is wasted on any range nearer to the platform than this minimum range.

The sampling and data storage requirements are reduced by using the analog dechirp. Rather than continuously sampling at a rate sufficient to digitize the transmit bandwidth, the data is continuously collected at a much lower rate, sufficient for the bandwidth of the dechirped signal. The effect of dechirping is shown in Fig. 2.9. It can be seen that the bandwidth of the dechirped signal is related to the bandwidth of transmitted signal using (2.21) by:

$$BW_{dc} = \frac{2R_{\max} \cdot BW}{c_0 \cdot t_p} \quad (2.23)$$

To remove returns from targets outside the desired swath, LFM-CW SAR systems usually employ a band-pass filter with high out of band rejection [10, 21-22]. For targets at ranges farther than the maximum range with a corresponding frequency higher than the sampling rate, aliasing can occur, placing the target return within the swath. It is important that the bandpass filter attenuates such signals to avoid ambiguities. For a delayed dechirp there can be targets nearer to the radar than the minimum range. The frequencies from such targets can fold over into the sampling band when the signal is dechirped to baseband. One solution is to dechirp the signal to an intermediate frequency, apply the band-pass filter, and then mix to baseband [22] to avoid near range ambiguities.

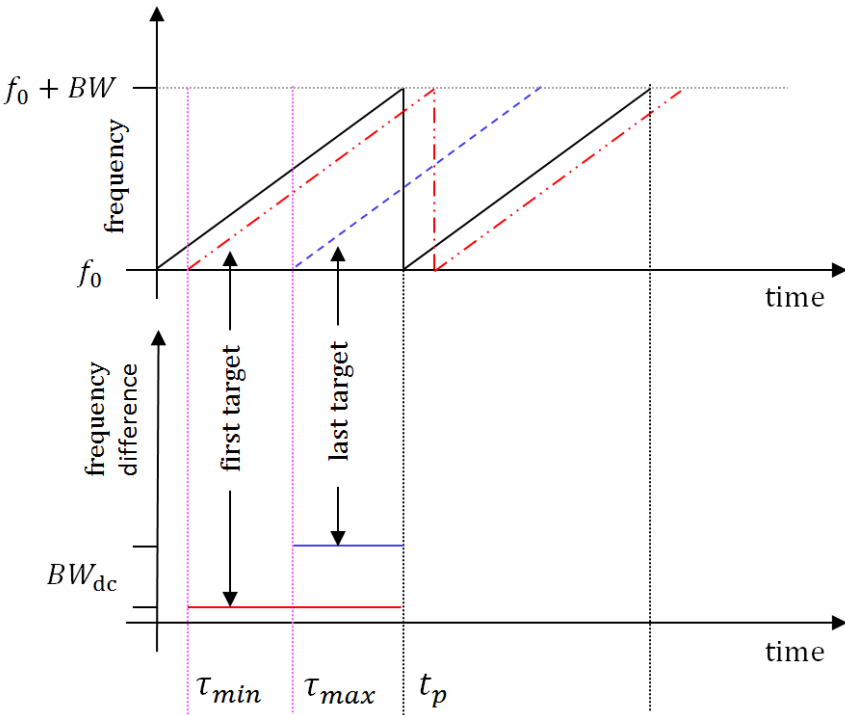


Figure 2.9: Simplified spectrogram of the SAR data (top) and the dechirped data (bottom) showing the effects of dechirping [6].

### 2.6.3.2 Range resolution and compression

For the dechirped data, range compression can be accomplished with a range Fourier transform, which separates the frequencies (and the ranges). The range resolution is determined by the frequency resolution of the Fourier transform,

$$\Delta f_r = \frac{1}{t_p} = \frac{f_s}{N} \quad (2.24)$$

here  $f_s$  is the sample rate of the analog to digital converter (ADC) and  $N$  is the number of samples collected for a single chirp. For dechirped SAR data, frequencies correspond to ranges; thus, this frequency resolution corresponds to a spatial range resolution,  $\Delta R$ , calculated as:

$$\Delta R = \Delta f_r \cdot \frac{c_0}{2 \cdot k_r} = \frac{c_0 \cdot f_s}{2 \cdot N \cdot k_r} \quad (2.25)$$

For CW SAR  $N/f_s = t_p$  and  $t_p \cdot k_r = BW$  (the transmit bandwidth), so that (2.25) simplifies to:

$$\Delta R = \frac{c_0}{2 \cdot BW} \quad (2.26)$$

which is equivalent to (2.8), the range resolution calculation for pulsed SAR.

## 2.7 Moving platform

Essential to all types of SAR operation is the motion of the platform, which also introduces complications. As the authors of [3] state, “In SAR, motion is the solution and the problem.” Without motion, or without using synthetic aperture techniques, the azimuth resolution of a radar is dependent on the beamwidth of the antenna; the resulting azimuth spatial resolution is highly dependent on range,

$$\Delta z_{ra} = 2R \tan\left(\frac{\theta_a}{2}\right) \quad (2.27)$$

The small angle approximation for trigonometric functions is applied so that:

$$\Delta z_{ra} = R \cdot \theta_a \quad (2.28)$$

The azimuth beamwidth of the antenna is approximated as  $\theta_a \approx \lambda/l_{az}$  where  $l_{az}$  is the length of the antenna in the azimuth direction and  $\lambda$  is the wavelength of the transmitted signal. Therefore, (2.28) is rewritten as follows:

$$\Delta z_{ra} = \frac{R \cdot \lambda}{l_{az}} \quad (2.29)$$

Equation (2.29) reveals that the azimuth resolution of a side-looking real aperture radar system is dependent on the length of the transmit antenna, the wavelength of the carrier frequency, and the slant-range to the target. Thus, in order to obtain useful imagery at far ranges (such as for spaceborne radar applications), it

is necessary to have an extremely long antenna. For instance, if a SAR platform is orbiting at an altitude of 800 km and operates at X-band ( $\lambda = 3$  cm), it would take an antenna 240 m long simply to achieve a resolution cell of  $\Delta z = 100$  m. An antenna that large would be extraordinarily difficult, if not impossible, to construct and deploy. The imaging geometry of SAR allows for the motion necessary to generate a target phase history that is due to the changing range between target and platform.

### 2.7.1 SAR imaging geometry and azimuth Resolution

In Fig. 2.10, the SAR platform moves along the flight path illuminating a target area off to one side. For airborne SAR, the flight path is ideally linear with a constant velocity (though in the real world there are always deviations from this ideal). The flight path for spaceborne SAR follows an orbital ephemeris. Nonlinear flight paths such as a circular path around a target can also be used, if the motion is precisely recorded and the data is processed with an appropriate algorithm that does not rely upon a linear flight path assumption.

For purposes of this discussion, we assume a geometry as illustrated in Fig. 2.10. A target is at slant-range  $R$ . The distance in the along-track direction from the radar to the target is  $a$ . The distance in the cross-track direction from the nadir track of the radar to the target is  $r$ . The platform is operating at an altitude of  $H$  meters and travelling at a velocity of  $v$  m/s. The angle of the target from antenna broadside is  $\gamma$ . In this case, the Doppler shift relative to the transmitted frequency is:

$$f_d = \frac{2v \cdot \sin \gamma}{\lambda} = \frac{2v \cdot a}{\lambda \cdot R} \quad (2.30)$$

Thus, if the radar signal is frequency analyzed, any energy that is at a delay corresponding to range  $R$  and at Doppler frequency  $f_d$  is associated with a target located at  $a$  distance:

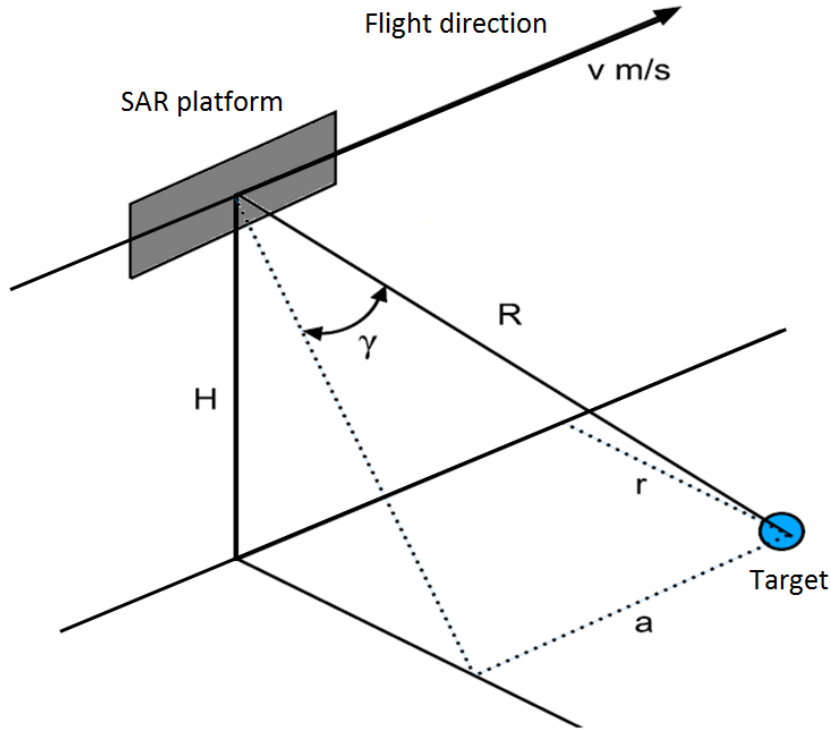


Figure 2.10: SAR imaging geometry for discussion of azimuth resolution.

$$a = \frac{\lambda \cdot R \cdot f_d}{2v} \quad (2.31)$$

from the point on the ground directly below the platform in the along-track direction.

The azimuth resolution of the SAR is dependent on the resolution,  $\Delta f_d$ , of the measurement of the Doppler frequency because we are using analysis of the Doppler shift to differentiate targets in the along-track direction. From (2.31) it follows that

$$\Delta z = \left( \frac{\lambda \cdot R}{2v} \right) \Delta f_d \quad (2.32)$$

We also note that the frequency domain resolution is approximately the inverse of the time span  $S$  of the waveform being analyzed i.e.  $\Delta f_d = 1/S$ . For SAR,  $S$  is the time during which a target is being illuminated by the radar. Since we are essentially using signal processing techniques to combine data from this entire time

span  $S$ , we refer to the distance that the platform travels in time  $S$  as the “synthetic aperture”, which is:

$$S = \frac{R \cdot \theta_a}{v} = \frac{R \cdot \lambda}{v \cdot l_{az}} \quad (2.33)$$

When we combine (2.32) and (2.33) with the given definition of  $\Delta f_d$ , the result is follows:

$$\Delta z = \left( \frac{\lambda \cdot R}{2v} \right) \left( \frac{v \cdot l_{az}}{R \cdot \lambda} \right) = \frac{l_{az}}{2} \quad (2.34)$$

This is the much celebrated result which relates the azimuth resolution of a SAR to the length of the antenna. The upshot is that a SAR is capable of obtaining very high-resolution imagery whether it is operating at a few hundred meters altitude, or several hundred kilometers altitude. Even though (2.34) expresses the theoretical limit for azimuth resolution, modern SAR systems are able to obtain resolutions very close to this ideal.

### 2.7.2 Change in range and signal phase history

With the platform moving during data collection, the range to a target changes slightly from one chirp to the next. While this change in range is much less than the resolution of the system, it is a measurable fraction of a wavelength and results in a change in the phase of the return echo. Tracking this phase history over the length of time that the target is in the illuminated antenna beam footprint allows us to compress the target, focusing it in azimuth. If we were to transmit a single frequency,

$$s_t = 2\pi f_0 t \quad (2.35)$$

and receive the echo at

$$\tau = \frac{2 \cdot R(\eta)}{c_0} \quad (2.36)$$

where  $R(\eta)$  is the range to target that changes from pulse to pulse, or in other words is dependent on “slow time”  $\eta$ , then the received signal is:

$$s_r = 2\pi f_0(t - \tau) = 2\pi f_0 \left( t - \frac{2R(\eta)}{c_0} \right) = 2\pi f_0 t - \frac{4\pi f_0 R(\eta)}{c_0} \quad (2.37)$$

Thus, the “expected phase” for a SAR signal is often expressed as:

$$\Phi_{ex} = \frac{4\pi R(\eta)}{\lambda} \quad (2.38)$$

For a linear flight path, an expression for  $R$  is:

$$R(\eta) = \sqrt{R_0^2 + (\mathbf{v} \cdot \boldsymbol{\eta})^2} \quad (2.39)$$

where  $R_0$  is the range of closest approach and  $\mathbf{v}$  is the velocity.

Most traditional SAR processing algorithms are derived using this expression for  $R(\eta)$ . When real world deviations from this ideal flight path result in defocusing, motion compensation can be applied to adjust the signal phase to match the ideal expression. Also, algorithms that are more precise and more computationally taxing can be employed to process SAR data with an arbitrary change in range, inherently correcting for non-ideal motion and allowing for a variety of nonlinear flight paths (e.g. circular). In any case, the basic idea behind SAR processing involves matching the expected phase of the signal form a target in order to compress, or focus, the energy from that target.

## 2.8 Basic signal processing for pulsed mode SAR

In modern digital SAR processing, there are three main steps to properly focusing the data: range compression, range cell migration correction, and azimuth compression. While different algorithms perform these operations in different ways, the basic concepts are the same. This section uses examples from a pulsed SAR processed with RDA [23].

### 2.8.1 Range compression

The received signal from a point target is an attenuated copy of the transmit signal delayed by the two-way time of flight to the target,  $\tau$ , expressed as [6]:

$$s_r(t) = A''(t) \exp \left( j \left( 2\pi(f_0 - f_{md})t - 2\pi f_0 \tau + \pi k_r (t - \tau)^2 + \phi \right) \right) \quad (2.40)$$

The return echo is an attenuated copy of the transmit signal, so we define a reference chirp equal to the transmit signal. When the received signal is convolved with the reference chirp, the result is a peak where the signals line up. This peak corresponds to the target range. In processing, this is efficiently done with an FFT, a complex-phase multiply, and an inverse-FFT. In other words, a matched filter for the transmitted chirp. For simplification let  $f_{md} = f_0$ . Mathematically we express the Fourier transform of the received signal in range direction,

$$S_r = \int_{\tau}^{\tau+t_p} s_r \cdot \exp(-j 2\pi f_r t) dt = B(f_r) \cdot \exp \left( -j \cdot \frac{2\pi \tau k_r f_0 + 2\pi \tau k_r f_r + \pi f_r^2}{k_r} \right) \quad (2.41)$$

where  $B(f_r)$  is a complex function which principally limits values of  $S_r$  to within the bandwidth of the chirp and it can be approximated by a rect function.

The Fourier transform of the time-reversed conjugate of the reference chirp is:

$$H_{rc} = \int_0^{t_p} \exp(-j \pi k_r (-t)^2) \cdot \exp(-j 2\pi f_r t) dt = B'(f_r) \cdot \exp \left( j \cdot \frac{\pi f_r^2}{k_r} \right) \quad (2.42)$$

where  $B'(f_r)$  is approximately the same as  $B(f_r)$ , and is approximated by the same rect function.

Then,  $S_r$  and  $H_{rc}$  are multiplied together:

$$S_r \cdot H_{rc} = B(f_r) \cdot B'(f_r) \cdot \exp(-j 2\pi \tau (f_0 + f_r)) \quad (2.43)$$

and the inverse Fourier transform is taken to obtain range-compressed signal:

$$\begin{aligned} s_{rc} &= \int_0^{t_p k_r} S_r \cdot H_{rc} \cdot \exp(2\pi f_r t) df_r = -j \frac{(\exp(j2\pi k_r t_p(t-\tau)) - 1)\exp(-j2\pi f_0 \tau)}{2\pi k_r(t-\tau)} \\ &= -j \frac{(\exp(j\pi k_r t_p(t-\tau)) - \exp(j\pi k_r t_p(\tau-t)))\exp(j\pi k_r t_p(t-\tau) - j2\pi f_0 \tau)}{2\pi k_r(t-\tau)} \\ &= \frac{\sin(t_p \pi k_r(t-\tau)) \cdot \exp(j\pi k_r t_p(t-\tau) - j2\pi f_0 \tau)}{\pi k_r(t-\tau)} \quad (2.44) \\ &= t_p \cdot \text{sinc}(t_p \pi k_r(t-\tau)) \cdot \exp(j\pi k_r t_p(t-\tau) - j2\pi f_0 \tau) \\ &\approx t_p \cdot \text{sinc}(t_p \pi k_r(t-\tau)) \cdot \exp(-j2\pi f_0 \tau) \end{aligned}$$

The result shows the peak of the sinc function at the range to the target. We can also see that the peak is higher when the pulse length is longer. The simplification that gives the last line of (2.44) is due to the fact that the exponential term dependent on  $(t - \tau)$  is unity when the sinc function is at a maximum. The phase of the range-compressed signal is identical to the expected phase from (2.38).

### 2.8.2 Range cell migration correction

When a series of range compressed pulses are stacked together, the change in range from one pulse to the next (the target trajectory) is clearly visible. Using an antenna with a wide enough azimuth beamwidth results in targets moving through multiple range bins (range resolution elements) across the length of the synthetic aperture; this is called range cell migration. To properly focus a target in azimuth, the data along the entire target trajectory is used, but doing so is complicated by the range cell migration.

One solution is to shift the trajectories such that the returns from a single target remain in the same range bin for the duration of the synthetic aperture. This allows us to use an FFT based matched filter along each range bin to focus all the energy from a target. The RDA performs range cell migration correction (RCMC) by employing an interpolation as described below.

A summary of the derivation of the SAR signal in the wavenumber domain that is presented by Cumming and Wong in [23] is included in this subsection. The derivation consists of taking the range and azimuth Fourier transforms of (2.40). We approximate the Fourier transforms using the principle of stationary phase (POSP), which is valid except in the extreme case of having radar frequencies very close to zero. The signal phase after the range Fourier transform using (2.40) is:

$$\Phi_R = -j \cdot 2\pi\tau (f_0 + f_r) - \frac{\pi f_r^2}{k_r} \quad (2.45)$$

Using the derivation for  $\tau$  in (2.39), we expand the (2.45) as

$$\Phi_R = -j \cdot \frac{4\pi R(\eta)(f_0 + f_r)}{c_0} - \frac{\pi f_r^2}{k_r} = -j \cdot \frac{4\pi \sqrt{R_0^2 + (v \cdot \eta)^2} (f_0 + f_r)}{c_0} - \frac{\pi f_r^2}{k_r} \quad (2.46)$$

where  $R_0$  is the range of closest approach,  $v$  is the velocity,  $f_r$  is range frequency,  $k_r$  is chirp rate, and  $f_0$  is carrier frequency.

In order to evaluate the phase signal after the azimuth Fourier transform, again the POSP is used. Building the azimuth Fourier transform adds the term  $-2\pi f_\eta \eta$  to the signal phase. Then the first derivative with respect to  $\eta$  is set to zero and solved for  $\eta$ .

$$\Phi_{Rd} = -j \cdot \frac{4\pi \sqrt{R_0^2 + (v \cdot \eta)^2} (f_0 + f_r)}{c_0} - \frac{\pi f_r^2}{k_r} - 2\pi f_\eta \eta \quad (2.47)$$

$$\frac{\partial \Phi_{Rd}}{\partial \eta} = \frac{-4\pi f_0 v^2 \eta}{c_0 \sqrt{R_0^2 + (v \cdot \eta)^2}} + \frac{-4\pi f_r v^2 \eta}{c_0 \sqrt{R_0^2 + (v \cdot \eta)^2}} - 2\pi f_\eta \eta = 0, \quad (2.48)$$

$$\begin{aligned} \eta &= -\frac{c_0 f_\eta R_0}{v \sqrt{-f_\eta^2 c_0^2 + 4v^2 f_0^2 + 8v^2 f_0 f_r + 4v^2 f_r^2}} \\ &= -\frac{c_0 f_\eta R_0}{2(f_0 + f_r)v^2 \sqrt{1 - \frac{c_0^2 f_\eta^2}{4(f_0 + f_r)^2 v^2}}} \end{aligned} \quad (2.49)$$

Substitute this into (2.47) and simplify with some algebraic manipulation to get the phase of the SAR signal in the wavenumber domain.

$$\Phi_{RD} = -\frac{4\pi R_0 f_0}{c} \sqrt{D^2(f_\eta) + \frac{2f_r}{f_0} + \frac{f_r^2}{f_0^2}} - \frac{\pi f_r^2}{k_r} \quad (2.50)$$

where

$$D(f_\eta) = \sqrt{1 - \frac{c_0^2 f_\eta^2}{4v^2 f_0^2}} \quad (2.51)$$

and  $f_\eta$  is azimuth frequency.

The RDA approximation is formed using a Taylor series approximation of (2.50). The square root term can be expanded as:

$$\Gamma(f_r) = \sqrt{D^2(f_\eta) + \frac{2f_r}{f_0} + \frac{f_r^2}{f_0^2}} \approx \Gamma(0) + \frac{\Gamma'(0)}{1!} f_r + \frac{\Gamma''(0)}{2!} f_r^2 + \frac{\Gamma'''(0)}{3!} f_r^3 \dots \quad (2.52)$$

The RDA keeps only the 0th order term,

$$\Phi_{RDA} \approx -\frac{4\pi R_0 f_0}{c_0} \cdot [D(f_\eta)] - \frac{\pi f_r^2}{k_r} \quad (2.53)$$

which makes the algorithm relatively simple. The first term of (2.53) is the azimuth modulation, corrected in the range-Doppler domain during azimuth compression. The second term is the chirp modulation corrected in the range compression step.

The signal returns from targets with equal range-of-closest-approach are co-located in the range-Doppler domain with the same trajectory shape. A migration factor,  $D(f_\eta)$ , can be used to calculate target trajectories in the range-Doppler domain. The curved trajectory of all targets with range of closest approach  $R_0$  is expressed as:

$$R_{RD}(f_\eta) = \frac{R_0}{D(f_\eta)} \quad (2.54)$$

To straighten the curved trajectories so that all the energy returned from a target is contained in the single range bin  $R_0$ , an azimuth frequency dependent interpolation can be used, shifting the trajectories by  $R_{RD}(f_\eta) - R_0$ .

### 2.8.3 Azimuth compression

While range compression is performed using a matched filter with the range chirp, azimuth compression uses a matched filter of the Doppler chirp. With the SAR signal range-compressed and the range cell migration removed, the signal can be expressed in the range-Doppler domain as:

$$s_{RD}(\tau, f_\eta) = C(\tau, f_\eta) \cdot \exp\left(-j \frac{4\pi f_0 R_0 D(f_\eta)}{c_0}\right) \quad (2.55)$$

where  $C(\tau, f_\eta)$  is a complex function which includes the signal limits in range and azimuth. The azimuth chirp is range dependent, so the matched filter is recalculated for each range bin. The filter is applied by multiplying the signal by:

$$H_{az} = \exp\left(j \frac{4\pi f_0 R_0 D(f_\eta)}{c_0}\right) \quad (2.56)$$

An inverse azimuth Fourier transform returns the signal to the time domain where the targets are now fully compressed. The quality of the focused image depends on how well the processing algorithm performs each step in forming the image. Approximations in deriving the signal model and other variations from the ideal signal can cause degradation in image quality.

## 2.9 Summary

In this Chapter, an introduction to SAR consisting of a short history of SAR, SAR image interpretation, applications, and different functional modes is presented. Then, an overview is given of the radar operation, introducing hardware components and system parameters crucial to any SAR processing theory. Two

SAR operating modes, pulsed SAR and continuous wave SAR, are compared and contrasted. As noted CW SAR needs less power than pulsed SAR, which would lower the cost and weight to the SAR sensor. Next, the importance of platform motion is discussed, including the SAR imaging geometry, and the motion-induced signal phase history. Finally, basic SAR processing is explained including range compression, range cell migration correction, and azimuth compression.

## Chapter 3. Problems definition and related review

In this Chapter, the research subjects that are examined in this dissertation consisting of SAR signal processing using NLFM waveform and phase error compensation using autofocus method with BP algorithm will be described. In addition, an overview of the various algorithms and problems related to them are performed.

### 3.1 Introduction

A major challenge in SAR system development involves compensation for undesirable variations in the azimuth SAR phase history. Primary causes of these phase variations include oscillator and other subsystem phase instabilities, uncompensated sensor motion, and atmospheric propagation.

The uncompensated along-track motions errors can cause a severe loss of geometry accuracy and degrade SAR image quality. In atypical airborne SAR system, an inertia navigation unit (INU) and a global positioning system (GPS) are employed to provide real-time data for motion compensation (MC). To achieve highly precise MC, the measurements have to be performed at sub-wavelength scale from pulse to pulse, which would exceed the accuracy of navigation systems. Therefore, navigation measurements usually provide only coarse MC, such as removal of the nonsystematic range cell migration and partial phase errors [24-25].

After conventional motion compensation (coarse MC), autofocus techniques are widely used to improve image focus. Autofocus refers to the computer-automated estimation and compensation of residual phase errors in SAR imagery.

Phase errors may be categorized as low-frequency phase errors and high-frequency phase errors. The detail classification of phase errors can be found in [26]. Depending on its nature and magnitude, phase errors can significantly degrade the image quality in terms of geometry linearity, resolution, image contrast, and SNR. The low-frequency phase errors affect the main-lobe of the system impulse response while high-frequency phase errors affect the sidelobe region.

Many autofocus algorithms have been proposed and developed since the early SAR development. A common approach in existing autofocus algorithms is to model the phase error as one-dimensional multiplicative noise in the azimuth domain. In general, autofocus techniques can be divided into two groups, namely model-based and non-parametric. Model-based autofocus techniques estimate the coefficients of an expansion that models the phase error. Elementary model-based autofocus may determine only the quadrature phase error (QPE), while more elaborate methods estimate higher order polynomial-like phase errors as well. The mapdrift (MD) and multiple aperture mapdrift (MAM) are examples of model-based autofocus algorithms for low-frequency phase errors compensation [27]. The MD and MAM's performance is only guaranteed if the phase error estimated is correctly modeled. However, these types of techniques are often unable to extract high-frequency phase errors due to the complexity of the problem.

Another group of autofocus techniques, commonly known as nonparametric autofocus, does not require explicit knowledge of the phase errors when estimate the phase errors. The Eigenvector method (EV) [28] and phase gradient autofocus (PGA) [29] are among nonparametric autofocus algorithms capable of estimating a variety of phase errors. However, these algorithms are generally time-consuming as their implementation involve long Fourier Transform operations and require large memory storage to store the entire synthetic aperture length. In addition, the

performance of PGA will be degraded if the window size is not properly selected for high-frequency sinusoidal phase errors estimation.

The SAR processing algorithms assume that the platform moves at a constant speed in a straight line. In any actual data collection this is not the case, as the platform experiences a variety of deviations from the ideal path. During data collection, whether in a manned aircraft or a UAV, there are deviations from this ideal as the platform changes its attitude, speed, or is subjected to turbulence in the atmosphere. These deviations introduce errors in the collected data which degrade the SAR image.

Translational motion causes platform displacement from the nominal, ideal path. This results in the target scene changing in range during data collection. This range shift also causes inconsistencies in the target phase history. Variations in along-track ground speed result in non-uniform spacing of the radar pulses on the ground. This non-uniform sampling of the Doppler spectrum results in erroneous calculations of the Doppler phase history. Traditionally the data is interpolated in the azimuth direction to correct for the velocity variations across the synthetic aperture. Alternatively, the filters used in processing can be modified to match the changes in velocity.

Changes in pitch, roll, and yaw introduce errors of a different kind. The pitching displaces the antenna footprint on the ground, the roll changes the antenna gain pattern over the target area, and the yaw introduces a squint. Pitch and yaw shift the Doppler centroid, with the shift being range dependent in the yaw case. If the Doppler spectrum is shifted so that a portion lies outside the Doppler bandwidth, then aliasing occurs. The azimuth compression produces ghost images at the azimuth locations where the Doppler frequency is aliased to zero.

Hardware- and software-based techniques are proposed in [30] to compensate non-ideal motion of SAR platform. The main idea is to use a system of GPS/INU to measure instantaneous speed, antenna rotation angles (yaw, pitch and roll), and platform trajectory. The along-track motion error comes of the non-uniform spatial sampling because of the ground velocity variation. The correction of the variations

of the forward velocity is performed by real time controlling of PRI. The antenna servo is used to stabilize the antenna direction to the look angle whether the attitude of the platform changes or not. MC across the track will be done in the real-time image formation flow after the antenna stabilization step and the along-track MC step.

In [31] a new method is proposed for MC of LFM-CW SAR signal. In this study, the LFM-CW SAR signal model is presented, and processing algorithms are discussed. The effects of non-ideal motion on the SAR signal are derived, and new methods for motion correction are developed, which correct for motion during the pulse. This new method is suitable for use with both the RDA and the FSA (or CSA), which accounts for the motion during the chirp. The proposed algorithm also corrects the range shift introduced by translational motion of magnitude greater than a single range bin without interpolation. This new MC algorithm is verified with simulated data and with actual data collected using the BYU $\mu$ SAR system.

In [32], the effect of antenna movements in different directions (pitch, roll and yaw) along the SAR sensor trajectory is investigated. Because of this antenna movement, the Doppler spectrum shifts with the value of Doppler centroid frequency (it is estimated from the raw data). Using a weighting window along with BP algorithm, tried to remedy this situation, so that the phase of SAR data where it is not within the Doppler bandwidth does not include for processing. In addition, a weighting applies within the Doppler bandwidth.

In [33], a new parametric autofocus algorithm is proposed using particle swarm optimization (PSO) algorithm. PSO is a population-based stochastic optimization technique based on the movement of swarms and inspired by social behavior of bird flocking or fish schooling. This paper presents a novel approach to solve the low-frequency high-order polynomial and high-frequency sinusoidal phase errors. The power-to-spreading noise ratio (PSR) and image entropy (IE) are used as the focal quality indicator to search for optimum solution. The algorithm is tested on both simulated two-dimensional point target and real SAR raw data from RADARSAT-1.

The reference [34] presents a new auto-focus method. Three types of possible distortions in directions of  $x$  (along-track),  $y$  (across-track) and  $z$  (the height of the platform) are modeled within the raw SAR signal, and the formulation for phase error caused by them are derived. Taking into accounts of range changes in the phase error model is one of the highlights of this method. Specifically, SAR signal is divided by blocks, and within each block, phase error is estimated using weighted phase gradient autofocus algorithm.

As we have discussed, deviation from the ideal case for SAR system happens in different situations. One classification for these deviations can be as follows: changing of the center of gravity of the platform, changing the platform speed, sliding SAR antenna in different directions. Using the information obtained by GPS/INS system one can partly compensate the phase error caused by these kind of deviations. The algorithms that use the motion information are almost obtained as deterministic relations to compensate the phase error [31]. The main issue is to compensate the remaining phase error in the SAR signal. In the following, problems definitions along with related review of research topics presented in this thesis will be discussed

### 3.2 Using of NLFM waveform in SAR imaging

Conventional SAR systems use LFM waveform for imaging. NLFM waveform can be used as an alternative in order to get better SAR imaging quality. In this thesis, both the linear and nonlinear frequency modulated waveforms are discussed.

Pulse compression is used in radar applications to enhance the range resolution of the radar system without increasing the peak transmitted power [35]. This compression is achieved by modulating the frequency of the transmitted pulse during a pulse width. The most common form of pulse compression waveform is LFM chirp. The matched filter (MF) response of this waveform has a sidelobe level about 13 dB, which can be improved by applying many methods like windowing, adaptive filtering [36], and optimization techniques [37]. These techniques can decrease side-lobes level but at the cost of reduced SNR and wider main-lobe. Low

side-lobes level makes detection of weak echo signals accompanied by strong signals from target with high RCS difficult or even impossible.

Another pulse compression method is NLFM, which can obtain fine resolution, and good SNR. It has a spectrum weighting function, which results in a pure MF giving low side-lobes. Therefore, the loss in SNR associated with weighting or with the traditional mismatching methods is eliminated [35].

Amplitude tapering of the transmitted signal is an alternative to NLFM for shaping the spectrum. However, this is not practical since efficient power amplification of the waveform requires operating the hardware in a non-linear way. This considerably reduces the ability to maintain accurate amplitude tapering. In addition, this implementation will lead to reduction of transmitted power, and therefore a SNR loss will occur.

Using the range-compressed signal or MF profiles across a series of radar transmissions is the basic of the SAR signal processing algorithms. Improving SNR and side-lobes levels of range-compressed signal results in a better SAR imaging quality. Therefore, using NLFM waveform can improve SAR imagery and this is the main objective to research of NLFM waveforms for SAR imaging.

By the current progress in developing digital-to-analog converters and large-scale field programmable gate arrays (FPGA) [38], generating accurate digital NLFM waveforms is not still a problem. Prior reports detailed designing and generating precision NLFM waveforms [39-40]. The drawback of some NLFM waveforms is its Doppler intolerance. Generally, as Doppler shifts, the MF output value decreases from its peak value. For Doppler tolerant signals such as a wide bandwidth LFM pulse, a fast Fourier transform (FFT) based filtering method can be used for match filtering to simplify receiver complexity.

The Doppler intolerance of NLFM waveforms may not be problematic for SAR related applications. This is because the Doppler bandwidth in SAR is small as compared to the radar applications. For example, for a C-band SAR sensor with 60 m/s speed, and 5-degree antenna azimuth beamwidth, the Doppler frequency will be between -100 Hz to 100 Hz, therefore the mismatch condition is tolerable for

match filtering of NLFM waveforms as compared to weather radar with a mismatch condition with 50 kHz Doppler frequency.

There is no reported real world application of NLFM waveforms for SAR in the literature. There are some papers, which theoretically investigate the usage of NLFM chirp signal in the SAR related applications. Zych [41] proposed a new NLFM waveform for ground penetrating radar to get better resolution compared to the LFM signal. There is no explicit formula for the NLFM signal proposed in the paper, and improvement for side-lobes level and resolution were not provided. In addition, signal processing algorithm for the NLFM waveform is not mentioned in the paper, there is only a formula for SAR raw signal generation and probably the algorithm for processing is time domain reconstruction (TDC), which is very time consuming.

Doerry [42] suggests the usage of NLFM waveform for SAR in a report for Sandia. The focus of the report is the effect of intra-pulse Doppler in SAR signal processing. He started with the fact that for NLFM waveforms, the effect of intra-pulse Doppler is more problematic in the signal processing procedure and it should be considered. The report is mainly discussed about the significance of intra-pulse Doppler effect on different processing algorithms and the way of its compensation. However, there is no simulation results concern with using a NLFM waveform in SAR signal processing in this report.

Ignoring the intra-pulse Doppler is the basis for assuming the “stop and go” model for range-Doppler processing, which admits that the radar position with respect to the target changes from pulse to pulse, but during any single pulse all relative motion stops and range is presumed constant. The intra-pulse Doppler is typically ignored by pulsed mode SAR systems, although it can become significant and needs to be accounted for FMCW mode SAR systems [6]. In FMCW SAR mode, the pulse duration or pulse width is higher than pulsed mode SAR; therefore, the Doppler shift caused by motion during the chirp becomes significant and should be compensated [43]. In FMCW mode SAR, a technique called de-chirping or de-ramping is used in contrast with pulsed mode SAR [6]. Its principle is that if a LFM

signal is de-chirped then the MF of signal degenerates into a Fourier transform of the de-chirped result. This is only true for LFM waveforms. No similar methods for NLFM waveforms have been reported in the literature. Therefore, we cannot use NLFM waveform in the FMCW mode SAR and it is beyond the scope of this dissertation.

Bayindir [44] proposed a new NLFM waveform for SAR imaging and its application to generate a synthetic data for testing the change detection methodology and algorithms. This NLFM waveform has the form of  $\exp(j\eta t^{1.75})$  and named as  $t^{0.75}$  frequency modulated ( $t^{0.75}$  FM) chirp signal, and is used to improve the SAR image resolution. He used spotlight SAR imaging geometry together with 2D polar and Stolt format reconstruction algorithms to validate the new NLFM chirp signal. However, there is no information in the thesis toward the choice of the new NLFM, and there is no comparison with other alternative NLFM waveforms in terms of sidelobe ratio reduction, resolution, loss in SNR and Doppler sensitivity.

In this study, we have proposed a new NLFM waveform using piecewise linear (PWL) functions. Compared to the generally used LFM, this chirp is shown to be capable of reducing the side-lobes level of MF response without having an adverse effect on SNR and main-lobe width. Popular methods of NLFM signal are investigated and their performances are assessed by measuring their side-lobes level reducing, main-lobe widening and Doppler sensitivity.

The idea of using PWL functions for NLFM waveform was raised by the previous work of Chan et.al [45]. The authors used a tri-stage PWL functions for NLFM waveform to reduce the sidelobe ratio of MF response as compared to LFM. It constructed of three LFM segments that increase the chirp rate at the leading and trailing edges of the waveform. The phase of this tri-stages NLFM signal is derived by integrating the instantaneous frequency. The problem with the method proposed by Chan et.al [45] is that the integration constants of instantaneous phase function, which preserve the continuity between different stages of NLFM waveform, are not considered. In addition, it is not mentioned in the paper that how the parameters of

the tri-stages PWL functions is obtained, the authors just mentioned that several potentially suitable functions have been investigated with varying the parameters. The result of match filtering are not good enough because of the phase discontinuity and the improvement for MF response is around 3 dB for peak sidelobe ratio compared to LFM.

### 3.3 Autofocus algorithm for flight trajectory optimization

The SAR processing algorithms assume that the radar platform moves at a constant speed in a straight trajectory. Nevertheless, this is not true as the platform experiences a variety of deviations from the ideal path in actual data collection. These deviations introduce errors in the stored data, which decrease SAR image quality. Coherent processing of SAR data requires precise knowledge of the relative geometric between the flight trajectory and the scene being imaged. This geometry information is typically acquired using navigation systems such as IMUs and GPS receivers. In a typical SAR system, navigation data are employed for MC. To achieve highly precise MC, motion measurements have to be achieved at sub-wavelength scale from pulse to pulse. However, these sensors could be too expensive and may not provide the accuracy required for high-resolution imaging. Thus, navigation measurements usually provide only coarse MC. Consequently, signal based MC, i.e., autofocus, is a crucial step that provides a necessary enhancement to IMU/GPS devices, especially for airborne SAR processing, to achieve a very fine resolution. The automatic estimation and compensation of phase errors in SAR image formation using the information in raw data is referred as autofocus algorithm.

Autofocus methods typically can be divided into two categories including the parametric and non-parametric methods. Parametric autofocus methods estimate a set of coefficients that parameterize a model, which is used to compensate for phase errors. Non-parametric methods estimate a phase function, which is used to compensate for phase errors. Many kinds of autofocus algorithms have been proposed over the years. Conventional autofocus methods are applicable for the

frequency domain data processing algorithms such as RDA, and FSA, and cannot be applied by BP image formation method. In the frequency domain algorithms, a coarse MC using navigation data is performed followed by an autofocus algorithm for estimating remaining phase error. However, BP algorithm uses the navigation data directly in the image formation procedure, and therefore conventional autofocus algorithm cannot be used. The BP image formation algorithm places few limitations on SAR imaging; therefore, it is desirable to have an autofocus algorithm that is likewise unconstrained.

In this dissertation, an autofocus method that is accordant with BP is presented. In the literature, some works reported the usage of autofocus for BP algorithm [45-48]. Hellsten et al. [46] proposed a method in which antenna path parameters is determined in order to get focused image using fast factorized BP algorithm. Antenna path parameters are determined in different sub-apertures using an optimization-based method in which the cost function is the integral of sub-image energy. Liu et.al [47] suggest a metric-based autofocus for BP algorithm in which only the platform speed is varied in order to get focused image. The platform speed is optimized by minimizing the entropy of SAR image, which is constructed by BP algorithm. Ash [48] proposes an autofocus routine for BP imaging for spotlight-mode SAR data. In this method, optimal phase error correction for each pulse is determined in a closed form within the coordinate descent framework, where focusing the image is equivalent to maximize the sharpness in standard BP algorithm.

The problem with the previous autofocus methods for BP algorithm is that the computational load of the metric-based method incorporating with the BP algorithm is generally high. This is because in each iteration of the optimization algorithm there should be an image or sub-image constructed by BP algorithm, which has high computational complexity. In addition, they have specific assumptions about the imaging geometry such as spotlight or circular modes.

To improve the efficiency but to keep the advantages, we present a new metric-based approach to modify the flight trajectory for BP imaging. This new method

makes no assumption about the imaging geometry. Knowing the initial path of the SAR sensor using the navigation data, we can obtain the optimum trajectory by optimizing a proper objective function. The flight trajectory is modeled using polynomial functions in a three dimensional space. Specifically, we propose an approximate model to obtain the objective function for optimization without using BP algorithm in order to lower the computational complexity.

Constructions of very small SAR systems are possible by using a LFM-CW signal in the radar transmitter [7-12]. Combined with an analog dechirp in the receiver, these systems can be made with hardware which is simpler, cheaper, and consumes less power than the conventional pulsed SAR systems. This enables the use of low cost SARs on UAS, which makes possible SAR imagery to be obtained in harsh climates or in environments too dangerous for manned aircraft or expensive SAR systems. The motion error problem is particularly apparent to the UAS SAR, because it is easily disturbed by the atmospheric turbulence due to its small size and lightweight. Moreover, the UAS SAR may not be equipped with a highly accurate navigation system due to weight capacity restriction [13]. Therefore, for the UAS SAR imaging, MC strategies are important and advisable based on the raw data or autofocus. For this reason, we have considered SAR in LFM-CW mode for theoretical discussions in this dissertation and the following chapter; however, it can be generalized for pulsed mode SAR.

### **3.4 Summary**

In this chapter, an overview of the methods of motion compensation, and autofocus algorithms to improve efficiency in non-ideal conditions (such as non-linear platform motion and phase errors) were discussed. Next, the issue of using NLFM waveform in SAR imaging is investigated. Finally, the use of autofocus algorithm with BP image reconstruction method and disadvantages of previous methods have been studied.

# Chapter 4. SAR signal processing using NLFM

In this Chapter, a new NLFM waveform is proposed, which can be used as a transmitted chirp in SAR imaging to improve the imaging quality compared to LFM chirp signal. The new NLFM is constructed based on piecewise linear functions which is optimized using multi-objective optimization. Different signal prospecting algorithms including time domain correlation, back-projection, omega-k, and range-Doppler algorithm are investigated in order to use NLFM as the transmitted chirp in SAR system. In addition, a modified motion compensation algorithm using navigation data is proposed for frequency domain algorithm [49-50].

## 4.1 Introduction

In this study, we have proposed a new NLFM waveform using PWL functions. Compared to the generally used LFM, this chirp is shown to be capable of reducing the side-lobes level of MF response without having an adverse effect on SNR and main-lobe width. Popular methods of NLFM signal are investigated and their performances are assessed by measuring their side-lobes level reducing, main-lobe widening and Doppler sensitivity. In order to validate the new offered chirp signal, strip-map SAR imaging geometry together with different reconstruction algorithms are considered. Both time and frequency domain signal processing methods are analyzed to process the SAR raw data generated based on NLFM chirp signal.

RDA [2], omega-K ( $\omega$ -K) [3], TDC, and BP [4] algorithms are chosen to investigate the new NLFM chirp signal.

The SAR processing algorithms assume that the platform moves at a constant speed in a straight line. However, this is not true in any actual data collection, as the platform experiences a variety of deviations from the ideal path. These deviations introduce errors in the collected data, which degrade the SAR image. Traditional motion compensation method is reviewed and a modified algorithm for NLFM chirp signal is proposed, which is suitable for use with the RDA.

The remainder of this Chapter is organized as follows. Subsection 4.2 gives the description of the new NLFM chirp signal using PWL functions. In subsection 4.3, SAR Signal processing for NLFM chirp signal is presented. Motion Compensation algorithm for NLFM waveform is explained in subsection 4.4. Finally, summary is given in subsection 4.5.

## 4.2 The proposed NLFM waveform

There are many research works to study the NLFM waveforms, and attempt to design the optimum form [51-54]. Generally, there are two NLFM designing procedures. One is based on PoSP for shaping the spectrum using a window function [51, 53]. The other one is called the explicit functions cluster method, which requires understanding of modulation rules for various NLFM waveforms [55].

In the following, we have described synthesizing NLFM waveforms by the stationary phase principle taking into account of the expected signal's auto-correlation function (ACF) [56]. Using the concept of spectrum shaping, we can control the frequency modulation of a LFM to produce an ambiguity function with the desired side-lobes level.

### 4.2.1 NLFM design based on PoSP

A real band-pass signal  $x(t)$  can be mathematically represented as:

$$x(t) = r(t) \cos(2\pi f_0 t + \phi(t)) \quad (4.1)$$

the corresponding analytical form is

$$\psi(t) = \tilde{x}(t) e^{2\pi f_0 t} \quad (4.2)$$

where

$$\tilde{x}(t) = r(t) e^{\phi(t)}$$

The PoSP states that the main influence to the spectrum at any frequency  $f$  is made by that part of the signal, which has instantaneous frequency  $f$ . This indicates that the PSD of a NLFM chirp at any frequency is inversely proportional to the chirp rate at the frequency  $f$ . Base on this principal (see Appendix), the relation between the modulus of the transmitted signal and the rate of change of the instantaneous frequency is given by [52]:

$$|X(f)| = 2\pi \frac{r(t)}{\sqrt{|\phi''(t)|}} \quad (4.3)$$

$$|\tilde{x}(t)|^2 = |r(t)|^2 = 2\pi \frac{|X(f)|^2}{|\Phi''(f)|} \quad (4.4)$$

From (4.3) and (4.4), it is clear that the spectral density of the low pass signal  $\tilde{x}(t)$  is related to the inverse of the frequency rate of change  $|\phi''(t)|$ , and to the amplitude of the signal at that time  $r(t)$ .

One principal feature of NLFM designing is to keep  $r(t)$  constant and shape the spectrum through  $|\phi''(t)|$ . However, the designing concept in LFM is based on keeping  $|\phi''(t)|$  constant and shaping the spectrum through  $r(t)$ .

The design can be performed by approximating  $X(f)$  by a function  $V(f)$ , which is determined independent of the amplitude function  $r(t)$ , then calculating the frequency modulation function. That means:

$$\Phi''(f) = k V^2(f) \quad (4.5)$$

If  $V(f)$  is defined over the frequency interval  $-B/2 \leq f \leq B/2$ , a constant power should be used in order to have good efficiency in a transmitter:

$$|r(t)|^2 = 1/T, \quad |t| \leq \frac{T}{2} \quad (4.6)$$

The first derivative  $\Phi'(f)$  is obtained by integrating the second derivative:

$$\Phi'(f) = \int_{-B/2}^f \Phi''(x)dx \quad (4.7)$$

The group delay function  $T_g(f)$  is then calculated by:

$$T_g(f) = -\frac{1}{2\pi} \Phi'(f) \quad (4.8)$$

Replacing (4.7) in (4.8), we obtain:

$$T_g(f) = \int_{-B/2}^f k_1 V^2(f) df + k_2 \quad (4.9)$$

where the integration constants  $k_1$  and  $k_2$  are chosen so that  $T_g(-B/2) = -T/2$  and  $T_g(B/2) = T/2$  ( $T$  is pulse length).

The instantaneous frequency as a function of time is the inverse of  $T_g(f)$  [40], that is:

$$f(t) = T_g^{-1}(f) \quad (4.10)$$

Finally, the phase function of the designed NLFM signal is obtained from the frequency function:

$$\phi(t) = 2\pi \int_0^t f(x) dx \quad (4.11)$$

As of the designing steps of NLFM, it appears that the NLFM sidelobe reduction depends on the choice of a correct spectrum shape or an appropriate window function. Harris [57] provides a complete review of the most common windows and their properties. To obtain a compressed pulse in the time domain with low side-lobes, a signal spectrum that decreases towards the band edges is required, which

has also low discontinuities in the frequency domain [58]. To generate such spectrum shape, it is necessary to determine the phase function  $\phi(t)$ , which produces this type of spectrum. In the following, phase functions of some of well-known NLFM waveforms are derived.

#### 4.2.1.1 Cosine spectrum shape

One class of the FM waveforms, which takes advantage of the PoSP to control (shape) the spectrum, is [51]:

$$V^2(f) = \left( \cos\left(\frac{\pi f}{B}\right) \right)^n, \quad |f| \leq \frac{B}{2} \quad (4.12)$$

The phase function is obtained for  $n = 1$  in (4.12) using the procedure explained in this Chapter as follows:

$$\begin{aligned} T_g(f) &= \int_{-B/2}^f k_1 V^2(f) df + k_2 = k_1 \frac{B(\sin(\frac{\pi f}{B})+1)}{\pi} + k_2 \\ \left\{ T_g\left(-\frac{B}{2}\right) = -\frac{T}{2}, T_g\left(\frac{B}{2}\right) = \frac{T}{2} \right\} &\rightarrow k_1 = \frac{T\pi}{2B}, k_2 = -\frac{T}{2} \\ f(t) &= T_g^{-1}(f) \rightarrow f(t) = \frac{B}{\pi} \arcsin\left(\frac{2t}{T}\right) \\ \phi(t) &= 2\pi \int_0^t f(x) dx = B \left( 2t \arcsin\left(\frac{2t}{T}\right) + \sqrt{(T-2t)(T+2t)} - T \right), |t| \leq \frac{T}{2} \quad (4.13) \end{aligned}$$

and the NLFM signal using (4.13) is obtained as:

$$x(t) = r(t) \cos\left(2\pi f_0 t + B \left( 2t \arcsin\left(\frac{2t}{T}\right) + \sqrt{(T-2t)(T+2t)} - T \right)\right) \quad (4.14)$$

For  $n$  higher than one, the phase functions are not simply expressed, and should be evaluated numerically.

### 4.2.1.2 Tangent-based waveform

Tangent function is an alternative class of NLFM waveform. The instantaneous frequency modulation function of this class is specified by [52]:

$$f(t) = \frac{B \tan\left(\frac{2\beta t}{T}\right)}{2 \tan(\beta)}, \quad |t| \leq \frac{T}{2} \quad (4.15)$$

where  $\beta = \tan^{-1}(\alpha)$ ,  $\alpha \geq 0$ , is a time sidelobe level control factor.

The phase function is obtained using the integration of the instantaneous frequency (4.15):

$$\phi(t) = 2\pi \frac{-B T \ln\left(\cos\left(\frac{2 \tan^{-1}(\alpha)t}{T}\right)\right)}{4\alpha \tan^{-1}(\alpha)}, \quad |t| \leq \frac{T}{2} \quad (4.16)$$

### 4.2.1.3 Truncated Gaussian

Truncated Gaussian spectrum shaping function is defined by [53]:

$$V^2(f) = \exp\left(-k\left(\frac{f}{2B}\right)^2\right), \quad |f| \leq \frac{B}{2} \quad (4.17)$$

$T_g(f)$  is obtained by integration of the spectrum:

$$T_g(f) = k_1 B \sqrt{\pi} \operatorname{erf}\left(\frac{\sqrt{k} f}{2B}\right) + k_2 \quad (4.18)$$

$$\left\{ T_g\left(-\frac{B}{2}\right) = -\frac{T}{2}, T_g\left(\frac{B}{2}\right) = \frac{T}{2} \right\} \rightarrow k_1 = \frac{T \sqrt{k}}{2B \sqrt{k} \operatorname{erf}\left(\frac{\sqrt{k}}{4}\right)}, k_2 = 0$$

where  $\operatorname{erf}$  is Gaussian error function.

The phase function for (4.18) is not simply expressed, and should be evaluated numerically.

#### 4.2.1.4 Hybrid NLFM

Hybrid NLFM is a result of an experimental research done by Price [54]. He suggested combining LFM and NLFM as:

$$f(t) = \frac{t}{T} \left( B_l + B_c \frac{1}{\sqrt{1-4t^2/T^2}} \right), |t| \leq \frac{T}{2} \quad (4.19)$$

where  $B_l$  is the total frequency sweep of the LFM part (left term), and  $B_c$  is the total frequency sweep, which is caused by LFM having the slope of the second term at  $t = 0$ .

The phase function is obtained using integration of the instantaneous frequency (4.19):

$$\phi(t) = 2\pi \left( -\frac{1}{4} B_c \sqrt{T^2 - 4t^2} + \frac{1}{4} TB_c + \frac{B_l t^2}{2T} \right), |t| \leq \frac{T}{2} \quad (4.20)$$

#### 4.2.2 New NLFM waveform using PWL functions

The implementation of spectrum shaping may lead to the penalty of main-lobe widening. In other words, there is no control on main-lobe requirement. In this study, NLFM waveform is designed such that its MF response satisfies both the side-lobes and main-lobe requirements altogether.

In this study, a new method based on generalized PWL functions is proposed to generate NLFM waveform. Specifically, instantaneous frequency function is constructed using  $n + 1$  stages PWL functions as shown in Fig. 4.1.

Most of well-known NLFM waveforms [51-55], have a form of first half reflected, i.e. the second half of the instantaneous frequency is the first half reflection. In addition, it is shown through experiments that this kind of transformation leads to a better MF results. Therefore, first half reflection function is used to generate the second half of the NLFM waveform. The first half of instantaneous frequency of the proposed NLFM waveform can be formulated as follows:

$$f(t) = \begin{cases} c_0 t & 0 \leq t < T_1 \\ B_1 + c_1(t - T_1) & T_1 \leq t < T_2 \\ \dots & \dots \\ B_n + c_n(t - T_n) & T_n \leq t < T/2 \end{cases} \quad (4.21)$$

where  $B$  is the frequency bandwidth,  $T$  is the pulse width, and

$$c_0 = \frac{B_1}{T_1}, \quad \underset{1 \leq m < n}{c_m} = \frac{B_{m+1} - B_m}{T_{m+1} - T_m}, \quad c_n = \frac{B/2 - B_n}{T/2 - T_n}$$

and the second half of the proposed NLFM waveform is:

$$f(t) = \begin{cases} B/2 + c_n(t - T/2) & T/2 \leq t < T - T_n \\ B - B_n + c_{n-1}(t + T_n - T) & T - T_n \leq t < T - T_{n-1} \\ \dots & \dots \\ B - B_1 + c_0(t + T_1 - T) & T - T_1 \leq t \leq T \end{cases} \quad (4.22)$$

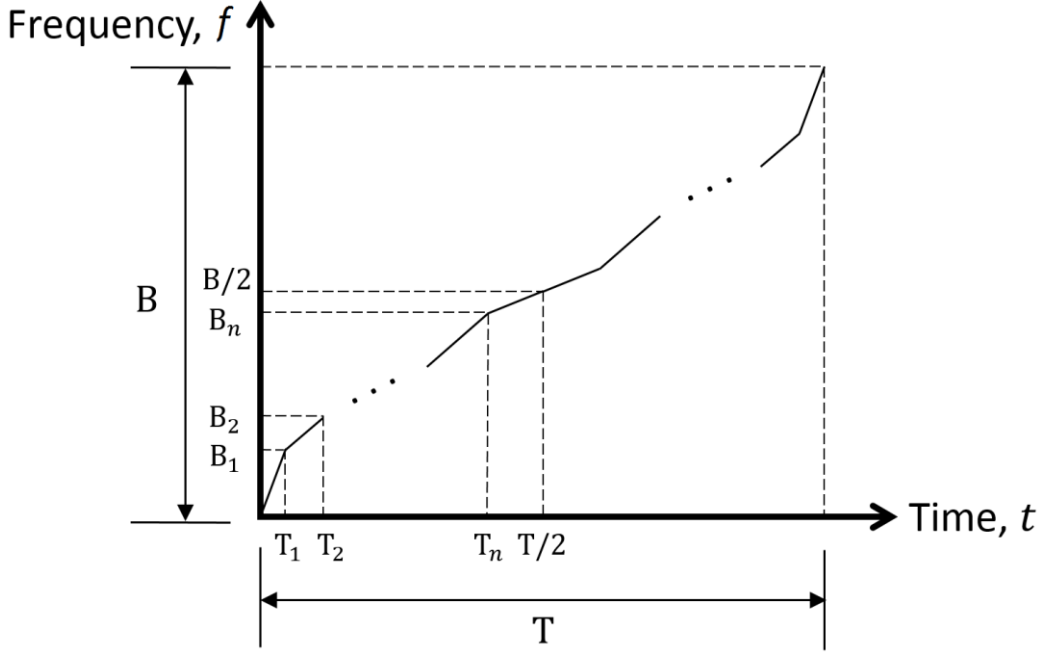
Then, the phase of this  $n + 1$  stages NLFM waveform can be derived by integrating (4.21) and (4.22) as:

$$\varphi(t) = 2\pi \begin{cases} c_0 t^2 / 2 + l_0 & 0 \leq t < T_1 \\ B_1 t + c_1(t^2 / 2 - T_1 t) + l_1 & T_1 \leq t < T_2 \\ \dots & \dots \\ B_n t + c_n(t^2 / 2 - T_n t) + l_n & T_n \leq t < T/2 \end{cases} \quad (4.23)$$

and the phase function for the second half is:

$$\varphi(t) = 2\pi \begin{cases} t \cdot \frac{B}{2} + c_n \left( \frac{t^2}{2} - t \cdot T/2 \right) + h_0 & T/2 \leq t < T - T_n \\ t \cdot (B - B_n) + c_{n-1} \left( \frac{t^2}{2} + t \cdot (T_n - T) \right) + h_1 & T - T_n \leq t < T - T_{n-1} \\ \dots & \dots \\ t \cdot (B - B_1) + c_0 \left( \frac{t^2}{2} + t \cdot (T_1 - T) \right) + h_n & T - T_1 \leq t \leq T \end{cases} \quad (4.24)$$

where  $l_0 \dots l_n$  and  $h_0 \dots h_n$  are used to preserve the continuity between different stages of the phase function. Using simple mathematical operations, these parameters are obtained as:


 Figure 4.1: Frequency modulation signal for  $n + 1$  stages PWL functions.

$$l_0 = 0, l_1 = -\frac{1}{2}B_1T_1 + \frac{1}{2}c_1T_1^2 \quad (4.25)$$

$$\sum_{2 \leq m \leq n} l_m = (B_{m-1} - B_m)T_m + \frac{1}{2}T_m^2(c_{m-1} + c_m) - c_{m-1}T_mT_{m-1} + l_{m-1} \quad (4.26)$$

$$h_0 = -\frac{1}{4}BT + \frac{1}{4}c_nT^2 + \frac{1}{2}B_nT - \frac{c_nT_nT}{2} + l_n \quad (4.27)$$

$$h_1 = (T - T_n) \left( \left( B_n - \frac{B}{2} \right) + \frac{c_{n-1}}{2}(T - T_n) - \frac{c_nT_nT}{2} \right) + h_0 \quad (4.28)$$

$$\sum_{2 \leq m \leq n} h_m = (T - T_{n-m+1}) \left( (B_{n-m+1} - B_{n-m+2}) + \frac{c_{n-m+1}}{2}(T - T_{n-m+1}) - \frac{c_{n-m+2}}{2}(T_{n-m+1} + T - 2T_{n-m+2}) \right) + h_{m-1} \quad (4.29)$$

### 4.2.3 Parameters selection based on multi-objective optimization

Having the model to generate the phase function for NLFM waveform, there are  $2n$  parameters ( $B_1 \dots B_n$ , and  $T_1 \dots T_n$ ) to be determined to have optimum MF response. The following measures are often used to determine the performance of MF response:

- Sidelobe-to-peak level ratio (SPLR): ratio between the returned signal of the first sidelobe of the MF response and the peak power of main-lobe:

$$\text{SPLR} = 10 \log \left( \frac{\text{first sidelobe power}}{\text{peak power of mainlobe}} \right) \quad (4.30)$$

- Integrated sidelobe level ratio (ISLR): ratio between the returned energy of the main-lobe and that integrated over several (usually 10 to 20) side-lobes on both sides of the main one:

$$\text{ISLR} = 10 \log \left( \frac{\text{power integrated over sidelobes}}{\text{total mainlobe power}} \right) \quad (4.31)$$

- Impulse response width (IRW): The impulse response width is defined as the width of the main-lobe of the impulse response, measured 3dB below the peak value.

In order to find the optimum parameters of the new NLFM waveform, a multi-objective optimization method should be used to minimize these three objectives simultaneously. One challenge is to use these three objectives at the same time and the other one is the choice of multi-objective optimizer.

For a convex optimization, all the objective functions and constraints should be convex functions. Note that the objective functions defined by (4.30), (4.31) and IRW are not convex over  $x$ , and hence, standard convex optimization techniques cannot be used to solve the optimization problem. Global optimization is a branch of applied mathematics that is capable of guaranteeing convergence in finite time to the actual optimal solution of a non-convex problem. Global optimization is distinguished from regular optimization by its focus on finding the maximum or minimum over all input values, as opposed to find local minima or maxima.

It is well-known that all of the optimization methods have at least some limitations. There is no single method or algorithm, which works the best on all class of problems. Because of the unknown and complicated design space for our non-convex multi-objective optimization problem, a reliable global optimization

algorithm should be used which works for a broad class of optimization problems. Therefore, we have chosen multi-objective goal attainment optimization [59], which is implemented in MATLAB optimization toolbox. It is possible to use another multi-objective solver to get better results, but it is beyond the scope of this paper.

Given a set of positive weights  $w_i$ , the goal attainment problem tries to find  $x$  to minimize the maximum of:

$$(F_i(x) - G_i)/w_i \quad (4.32)$$

where  $x$  is the parameter that should be estimated,  $F_i$  is objective function,  $G_i$  is the goal,  $w_i$  is a weight, and  $i$  is the index for the objective function.

Generally, this minimization is supposed to be accomplished while satisfying all types of constraints including:

$$c(x) \leq 0, ceq(x) = 0, A.x \leq b, Aeq.x = beq, \text{and } l \leq x \leq u \quad (4.33)$$

where the matrix  $A$  and vector  $b$  are, respectively, the coefficients of the linear inequality constraints and the corresponding right-side vector. The matrix  $Aeq$  and vector  $beq$  are, respectively, the coefficients of the linear equality constraints and the corresponding right-side vector.  $x$  is the solution found by the optimization function.  $l$  and  $u$  are lower and upper bound vectors of solutions space.  $c(x)$  is the function that computes the nonlinear inequality constraint and  $ceq(x)$  computes the nonlinear equality constraint.

In other words, the goal attainment problem is to minimize a slack variable  $\gamma$ , defined as the maximum over  $i$  of the expressions (4.32). This suggests an expression, which is the formal statement of the goal attainment problem:

$$\min_{x,y} \gamma, \text{such that } F(x) - w.\gamma \leq G, c(x) \leq 0, ceq(x) = 0, A.x \leq$$
 (4.33)

$$b, Aeq.x = beq, \text{and } l \leq x \leq u$$

The term  $w \cdot \gamma$  introduces an element of slackness into the problem, which otherwise forces the optimization algorithm satisfying strictly the goals. The weighting vector,  $w$ , allows the relative compromises between the objectives. The goal attainment technique is shown geometrically in Fig. 4.2 for two objectives. Specification of the goals,  $\{G_1, G_2\}$ , defines the goal point,  $P$ . The weighting vector defines the search direction from point  $P$  to the possible function space,  $\Lambda(\gamma)$ . During the optimization,  $\gamma$  is changed, which varies the size of the possible region. Finally, the constraint boundaries converge to the single solution point  $G_{1s}, G_{2s}$ .

The preceding details have been implemented in “fgoalattain” function of MATLAB optimization toolbox. Here, we have used SPLR( $x$ ) and ISLR( $x$ ) as two objectives ( $F_1$  and  $F_2$ ), and IRW( $x$ ) is used in the nonlinear inequality constraint  $c(x) \leq 0$ , where  $c(x) = \text{IRW}(x) - v \cdot \text{IRW}_{\text{LFM}}$ .  $\text{IRW}_{\text{LFM}}$  is the impulse response width of MF in the LFM waveform case, and  $v$  is a widening factor, which is chosen in order to control the impulse response width in the optimization procedure and we set it to 1.35. For getting better SPLR and ISLR of MF response, this parameter can be increased. In addition,  $G_1$  and  $G_2$  are set to  $\{-40, -65\}$ , and the weights  $w_1$  and  $w_2$  are  $\{1, 2\}$ , which are obtained through the experiments. In general, some forms of trial-and-error tuning are necessary for each particular instance of optimization problem. The widening factor  $v$ ,  $G_1$ ,  $G_2$ , and the weights can be changed based on the system requirements including IRW, SPLR and ISLR of MF response.

The overall shape of frequency modulation and pulse-compressed response of the proposed waveform is shown in Fig. 4.3. Complete discussions and comparisons with other NLFM waveforms are given in the experimental results chapter.

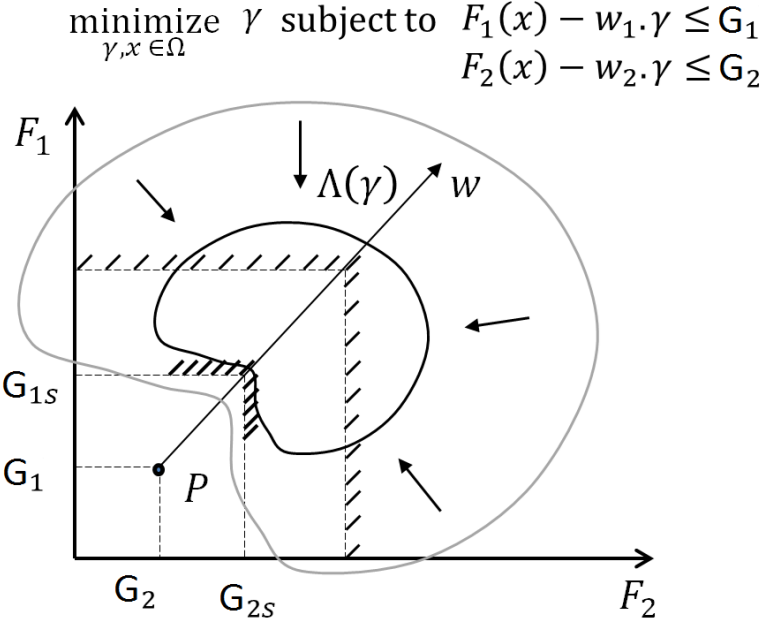
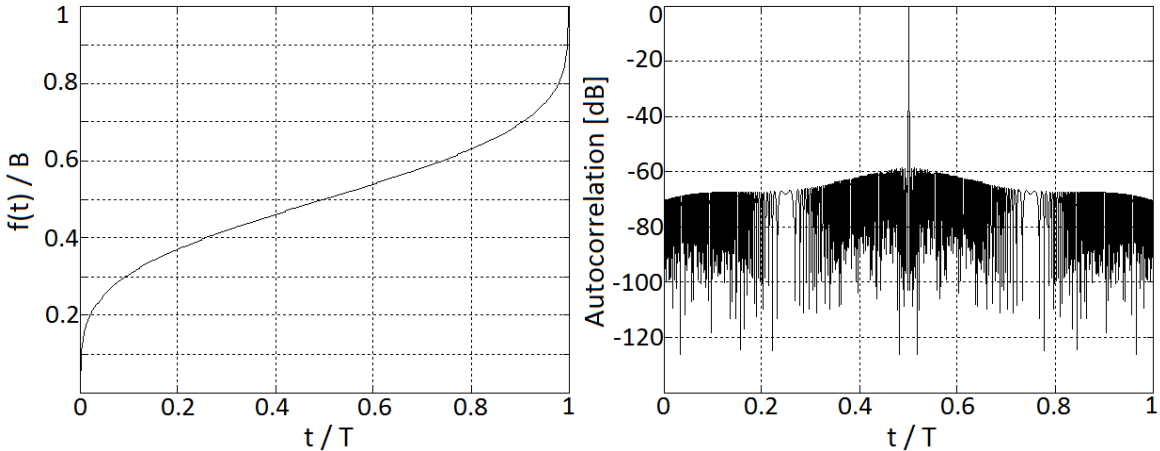


Figure 4.2: Geometrical representation of the goal attainment method [59].


 Figure 4.3: Proposed NLFM waveform using 64 parameters ( $n = 32$ ) (left), and MF output (right).

### 4.3 SAR signal processing for NLFM chirp signal

In this Section, first we will describe how to model the transmitted and received signal based on NLFM waveform. Then, different time and frequency domain algorithms for image formation of received SAR signal are explained.

Before the SAR signal is generated, a number of important system parameters should be determined, including carrier frequency, bandwidth, pulse length, and

PRF. The transmitted signal is a NLFM waveform, where the signal spans the bandwidth over the pulse length. This cycle is repeated at the PRF. The SAR signal is usually generated at or near baseband and then mixed up to the desired operating frequency before transmission. The NLFM transmit signal can be expressed as:

$$s_t(t) = A(t)\exp(j(2\pi f_0 t + \varphi(t) + \varphi_0)) \quad (4.35)$$

where  $A(t)$  is the signal amplitude and defines the pulse length with a Rect function,  $\varphi(t)$  is the phase function expressed in (4.23) and (4.24),  $f_0$  is the frequency at the beginning of the chirp, and  $\varphi_0$  is the starting phase which can usually be neglected.

A power amplifier increases the signal power to a specified level in the transmission chain. The transmitted signal should have enough power so that the SNR is large enough to generate an appropriate image. SNR also depends on the specific imaging parameters, especially the range to target and antenna beamwidth. An antenna propagates the amplified signal to the target area. The propagation environment includes the layers of atmosphere (usually approximated as free space) and the distributed scatterers, which construct the target scene. A very small portion of the transmit signal is reflected back to the radar. By neglecting the time-scaling influences on the pulse envelope, the echoed signal from target can be expressed as:

$$s_r(t, \eta) = A'(t)\exp(j(2\pi f_0(t - \tau) + \varphi(t - \tau) + \varphi_0)) \quad (4.36)$$

where  $t$  is the fast time,  $\eta$  is the slow time (or azimuth time), and  $A'(t)$  is an attenuated version of  $A(t)$  and  $\tau$  is the two-way time of flight to the target at range  $R$ .

The received signal is amplified with a low-noise amplifier (LNA) and mixed down to an appropriate band for sampling. After the signal from (4.36) is mixed down by a frequency,  $f_m$ , the signal ready to be recorded is as:

$$s_{rm}(t, \eta) = A''(t)\exp(j(2\pi f_0(t - \tau) + \varphi(t - \tau) + \varphi_0 - 2\pi f_m t)) \quad (4.37)$$

where  $A''(t)$  is an amplified version of  $A'(t)$ .

For simplification let  $f_m = f_0$ , therefore,

$$s_{rm}(t, \eta) = A''(t) \exp(j(-2\pi f_0 \tau + \varphi(t - \tau) + \varphi_0)) \quad (4.38)$$

SAR systems digitize this data and either store it on board, transmit it to a ground station, or process it on-board. In the following, different time and frequency domain algorithms for processing raw data based on NLFM waveform as the transmitted signal will be described.

### 4.3.1 Time domain correlation

The time domain correlation (TDC) algorithm uses the raw data directly, without range compression. In this case, SAR image from a point target is formed using the following formula:

$$im(x_0, y_0, z_0) = \sum_t \sum_\eta s_{rm}(t, \eta) \exp(j\Phi_{\tau_0}(t, \eta)) \quad (4.39)$$

where  $(x_0, y_0, z_0)$  is the coordinate of the point target,  $\Phi_{\tau_0}$  is negative of the phase in (4.38) which can be expressed as:

$$\Phi_{\tau_0}(t, \eta) = -(-2\pi f_0 \tau_0 + \varphi(t - \tau_0) + \varphi_0) \quad (4.40)$$

and  $\tau_0$  is obtained using the following:

$$\tau_0 = \frac{2R(t, \eta)}{c} = \frac{2\sqrt{(H-z_0)^2 + y_0^2 + (v(t+\eta) - x_0)^2}}{c} \quad (4.41)$$

where  $v$  is the platform velocity,  $H$  is the flight altitude and  $c$  is the light speed.

This is a very exact method, but it is very computationally taxing, which is rarely used in practice. However, it is important, because it gives a reference for measuring the imaging quality of other reconstruction algorithms.

### 4.3.2 Back-projection

Since the TDC algorithm is computationally intensive for practical purposes, it is natural to use approximations, which reduce the cost of the algorithm. BP normally operates on the range-compressed data [4]. For SAR data, range compression can be performed using MF. Using the stop and go approximation,  $\tau_0$  does not depend in fast time  $t$ , and we can rewrite (4.39) as:

$$im(x_0, y_0, z_0) = \sum_{\eta} \exp(j2\pi f_0 \tau_0) \sum_t s_{rm}(t, \eta) \exp(-j\varphi(t - \tau_0)) \quad (4.42)$$

The inner sigma in (4.42) is the definition of MF. For range compression, we define a reference chirp equal to the transmit signal. When the received signal is convolved with the reference chirp, the result is a peak where the signals line up. This peak corresponds to the target range. In processing, this is efficiently done with a FFT, a complex-phase multiply, and an inverse FFT. Therefore, for range-compressed signal we have:

$$s_{rc}(\tau_0, \eta) = \sum_t s_{rm}(t, \eta) \exp(-j\varphi(t - \tau_0)) \approx a \operatorname{Sinc}(b(t - \tau_0)) \quad (4.43)$$

where  $a$  and  $b$  are constants.

Using (4.43), (4.42) can be reformulated as:

$$im(x_0, y_0, z_0) = \sum_{\eta} \exp(j2\pi f_0 \tau_0) s_{rc}(\tau_0, \eta) \quad (4.44)$$

The benefits of BP include the simplicity of the algorithm, the parallel computation structure, and the ability to process data from an arbitrary platform path. The shortcomings are that the motion of the platform must be precisely known and the algorithm is very computationally taxing. However, using the parallel nature of the algorithm and the parallel processing of modern general-purpose graphic processor units can significantly improve the processing time. Similar to TDC method, the motion of the platform must be precisely known for BP algorithm.

### 4.3.3 Omega-K algorithm

Omega-K algorithm [43] works on the wavenumber or 2-D frequency domain of SAR signal, which is based on LFM waveform. In order to derive the algorithm for NLFM chirp signal, some modifications should be done. First, FFT is performed to transform the SAR signal data into the range frequency domain:

$$\begin{aligned} S_{rm}(f_r, \eta) &= \mathcal{F}_t\{s_{rm}(t, \eta)\} = A \cdot B(f_r) \cdot \exp(-j2\pi f_0 \tau) \cdot \mathcal{F}_t\{\exp(j\varphi(t - \tau))\} \\ &= A \cdot B(f_r) \cdot \exp(-j2\pi f_0 \tau) \cdot \exp(-j2\pi f_r \tau) \cdot \mathcal{F}_t\{\exp(j\varphi(t))\} \end{aligned} \quad (4.45)$$

where  $A$  is a constant, and  $B(f_r)$  is a complex function which limits the values of  $S_{rm}$  to within the bandwidth of the chirp.  $B(f_r)$  can be approximated by a Rect function.

For NLFM chirp signal,  $\mathcal{F}_t\{\exp(j\varphi(t))\}$  cannot be easily expressed unlike the LFM waveform. Therefore, we should eliminate this expression in (4.45) in order to obtain the SAR signal formula in 2-D frequency domain. To aim this, we obtain the Fourier transform of the time-reversed conjugate of the reference chirp as:

$$H_r(f_r, \eta) = A' \cdot B'(f_r) \cdot \mathcal{F}_t\{\exp(-j\varphi(-t))\} \quad (4.46)$$

where  $A'$  is a constant, and  $B'(f_r)$  is a complex function, which can be approximated by a Rect function.

Then, (4.45) and (4.46) are multiplied together,

$$S_r(f_r, \eta) = H_r(f_r, \eta) \times S_{rm}(f_r, \eta) \approx A'' \cdot B''(f_r) \cdot \exp(-j2\pi(f_0 + f_r)\tau) \quad (4.47)$$

where  $A''$  is a constant, and  $B''(f_r)$  is approximately the same as  $B'(f_r)$ .

We now expand the time delay  $\tau$  in (4.47) to the range to target  $R(\eta)$ . The phase function after the range Fourier transform is obtained as:

$$\phi_r(f_r, \eta) = -4\pi(f_0 + f_r) \cdot R(\eta)/c \quad (4.48)$$

where  $R(\eta) = \sqrt{r_0^2 + (\nu \cdot \eta - x_0)^2}$ , and  $r_0$  is closest approach from platform to the target,  $r_0 = \sqrt{H^2 + y_0^2}$ .

We can approximate the azimuth Fourier transform using the PoSP. An expression for the signal phase in the azimuth Fourier transform integral is computed by adding the phase term  $-2\pi f_a \eta$  to the (4.48), where  $f_a$  is the azimuth frequency.

$$\phi = -4\pi(f_0 + f_r) \cdot R(\eta)/c - 2\pi f_a \eta \quad (4.49)$$

Take the derivative of the phase with respect to  $\eta$ , and solve it for  $\eta$  at the point where the phase is stationary (i.e. where  $d\phi/d\eta = 0$ ).

$$\frac{d\phi}{d\eta} = \frac{-4\pi(f_0 + f_r)(\nu^2 \cdot \eta - \nu \cdot x_0)}{c \sqrt{r_0^2 + (\nu \cdot \eta - x_0)^2}} - 2\pi f_a \eta = 0 \quad (4.50)$$

The stationary point is found by solving it for  $\eta$

$$\eta = \frac{-c \cdot f_a \cdot r_0}{\nu \sqrt{4(f_0 + f_r)^2 \cdot \nu^2 - f_a^2 c^2}} - \frac{x_0}{\nu} \quad (4.51)$$

Substitute obtained  $\eta$  into (4.49) and simplify it to obtain the signal phase after the azimuth Fourier transform of the signal.

$$\phi_r(f_r, f_a) = -\frac{2\pi r_0}{\nu \cdot c} \sqrt{4(f_0 + f_r)^2 \cdot \nu^2 - f_a^2 c^2} - \frac{2\pi f_a x_0}{\nu} \quad (4.52)$$

The exponential, which makes up the signal in 2-D frequency domain can be expressed as:

$$S_r(f_r, f_a) = \exp \left( -j \left( \frac{2\pi r_0}{\nu \cdot c} \sqrt{4(f_0 + f_r)^2 \cdot \nu^2 - f_a^2 c^2} + \frac{2\pi f_a x_0}{\nu} \right) \right) \quad (4.53)$$

Then, the reference function multiplication (RFM) is applied [23]. The reference function is computed for a reference range,  $r_{ref}$ . A target at the reference range is correctly focused by the RFM, but targets away from that range are only partially

focused. For this reason, the RFM can be considered as a “bulk compression” [23]. The RFM filter can be expressed as:

$$\text{RFM}(f_r, f_a, r_{ref}) = \exp\left(j \frac{2\pi r_{ref}}{v.c} \sqrt{4(f_0 + f_r)^2 \cdot v^2 - f_a^2 c^2}\right) \quad (4.54)$$

where  $r_{ref}$  denotes the reference range, which is generally defined as the closest slant range from the scene center to the receiver.

After RFM filtering, the remaining signal becomes:

$$\begin{aligned} S'_r(f_r, f_a) &= S_r(f_r, f_a) \times \text{RFM}(f_r, f_a, r_{ref}) = \\ &\exp\left(-j \left(\frac{2\pi(r_0 - r_{ref})}{v.c} \sqrt{4(f_0 + f_r)^2 \cdot v^2 - f_a^2 c^2} + \frac{2\pi f_a x_0}{v}\right)\right) \end{aligned} \quad (4.55)$$

The next step is the Stolt interpolation [60]. It completes the focusing of targets away from the reference range  $r_{ref}$  by re-mapping the range frequency axis. The Stolt interpolation is defined as [23]:

$$\sqrt{(f_0 + f_r)^2 - \left(\frac{f_a c}{2 \cdot v}\right)^2} \rightarrow f_0 + f'_r \quad (4.56)$$

To achieve perfect range compression and registration, the mapping in (4.56) transforms the original range frequency variable  $f_r$  into the new range frequency variable,  $f'_r$ . In this manner, the phase is now linear with the new range frequency variable  $f'_r$ , i.e.,

$$\phi_{\text{Stolt}}(f_r, f_a) \approx \frac{4\pi(r_0 - r_{ref})(f_0 + f'_r)}{c} + \frac{2\pi f_a x_0}{v} \quad (4.57)$$

From (4.57), we can find that the Stolt interpolation completely removes the range–azimuth coupling and azimuth modulation. Finally, a two-dimensional inverse FFT is performed to transform the data back to the time domain, i.e. the SAR image domain (as the inverse FFT of a sine wave is a Sinc function):

$$im(t, \eta) = p_r \left( t - \frac{2(r_0 - r_{ref})}{c} \right) \cdot p_a \left( \eta - \frac{x_0}{v} \right) \quad (4.58)$$

where  $p_r(t)$  and  $p_a(\eta)$  are the compressed pulse envelope in the range and the azimuth directions, respectively.

One of the shortcomings of omega-K algorithm is the computationally costly Stolt interpolation step. In addition, since, all the processing is done in the wavenumber or 2-D frequency domain; there is no chance for applying range-dependent motion compensation for non-ideal platform motion.

#### 4.3.4 Range-Doppler algorithm

The most frequently used algorithm for SAR signal processing is the RDA [2]. It was developed for processing SEASAT SAR data in 1978. There are three main steps to correctly focusing the data using RDA: range compression, range cell migration correction, and azimuth compression. In order to *use* RDA for processing the raw signal based on NLFM chirp signal, we rewrite (4.53) as:

$$S_r(f_r, f_a) = \exp \left( -j \left( \frac{4\pi r_0 f_0}{c} \sqrt{D^2(f_a) + \frac{2f_r}{f_0} + \left( \frac{f_r}{f_0} \right)^2} + \frac{2\pi f_a x_0}{v} \right) \right) \quad (4.59)$$

where

$$D(f_a) = \sqrt{1 - \left( \frac{c f_a}{2 v f_0} \right)^2}$$

The RDA is obtained as a result of using Taylor series approximation of (4.59). The square root term in (4.59) can be expanded as:

$$\Gamma(f_a) = \sqrt{D^2(f_a) + \frac{2f_r}{f_0} + \left( \frac{f_r}{f_0} \right)^2} \approx \Gamma(0) + \frac{\Gamma'(0)}{1!} f_r + \frac{\Gamma''(0)}{2!} f_r^2 + \frac{\Gamma'''(0)}{3!} f_r^3 + \dots \quad (4.60)$$

The RDA keeps only up to the first order,

$$\emptyset_{RDA} = - \left( \frac{4\pi r_0 f_0}{c} \cdot \left[ D(f_a) + \frac{f_r}{f_0 \cdot D(f_a)} \right] + \frac{2\pi f_a x_0}{v} \right) \quad (4.61)$$

which makes the algorithm relatively simple. Using this approximation, the inverse Fourier transform of (4.59) in range direction give us the signal in the range-Doppler domain:

$$S_r(\tau, f_a) \approx p_r \left( \tau - \frac{2r_0}{c \cdot D(f_a)} \right) \cdot \exp \left( -j \left( \frac{4\pi r_0 f_0}{c} \cdot D(f_a) + \frac{2\pi \cdot f_a x_0}{v} \right) \right) \quad (4.62)$$

As it can be seen from (4.62), the target is compressed in range direction with the curved trajectory  $r(f_a)$ , which is called the range cell migration:

$$r(f_a) = \frac{r_0}{D(f_a)} \quad (4.63)$$

To compensate the range cell migration so that all the energy returned form a target is contained in the single range bin  $r_0$ , an azimuth frequency dependent interpolation should be used, shifting the trajectories by  $r(f_a) - r_0$ .

While the range-compression is performed using a MF with the reference chirp, azimuth compression uses a MF of the Doppler chirp. With the SAR signal range-compressed and the range cell migration removed, the signal can be expressed in the range-Doppler domain as:

$$S_r(\tau, f_a) \approx p_r \left( \tau - \frac{2r_0}{c} \right) \cdot \exp \left( -j \left( \frac{4\pi r_0 f_0}{c} \cdot D(f_a) + \frac{2\pi \cdot f_a x_0}{v} \right) \right) \quad (4.64)$$

The azimuth chirp is range dependent, so the MF is recalculated for each range bin. The MF is applied by multiplying the signal by the following:

$$H_{az}(r_0, f_a) = \exp \left( j \frac{4\pi r_0 f_0}{c} \cdot D(f_a) \right) \quad (4.65)$$

After azimuth match filtering, the remaining signal becomes

$$S'_r(\tau, f_a) = p_r \left( \tau - \frac{2r_0}{c} \right) \cdot \exp \left( -j \frac{2\pi \cdot f_a x_0}{v} \right) \quad (4.66)$$

Finally, an inverse azimuth FFT returns the signal to the time domain where the targets are now fully compressed:

$$im(\tau, \eta) = p_r \left( \tau - \frac{2r_0}{c} \right) \cdot p_a \left( \eta - \frac{x_0}{v} \right) \quad (4.67)$$

One drawback of RDA is a computationally taxing interpolation to correct the range cell migration. Another limitation is the incapability to handle squint-mode or wide-beam SAR. However, there is a modification to the RDA, which can help by introducing a secondary range-compression (SRC). The SRC keeps an additional term of a Taylor series approximation of (4.60) in the phase function, but only at a reference range [2].

#### 4.4 Motion compensation algorithm for NLFM chirp signal

The SAR processing algorithms described in previous subsection assume that the platform moves at a constant speed in a straight line. Translational motion causes a platform displacement from the nominal, ideal path as shown in Fig. 4.4 (a). This results in the target scene changing in range during data collection. This range shift also causes inconsistencies in the target phase history. A target at range  $R_0$  measured at range  $R = R_0 + \Delta R_0$  results in a phase error in (4.38):

$$s_{\Delta rm}(t, \eta) = A''(t) \exp \left( j(-2\pi f_0(\tau_0 + \Delta\tau_0) + \varphi(t - (\tau_0 + \Delta\tau_0)) + \varphi_0) \right) \quad (4.68)$$

where  $\tau_0 = 2R_0/c$ ,  $\Delta\tau_0 = 2\Delta R_0/c$ ,  $\Delta R_0$  is small deviation from  $R_0$  due to nonlinear motion,  $\Delta R_0 = R - R_0$  (see Fig. 4.4), and  $\varphi_0$  is the starting phase, which is unknown and will be neglected in the remaining discussion.

Unlike for the LFM case, the phase error in (4.68) cannot be simply expressed in time domain for NLFM chirp signal. Fortunately, if the motion is known (using an on-board INS/GPS sensor), then the motion errors can be compensated. In general, the motion data is collected at a much slower rate than the SAR data. The motion data must be interpolated so that every sample of SAR data has corresponding position information. Each data point also needs to have a corresponding location

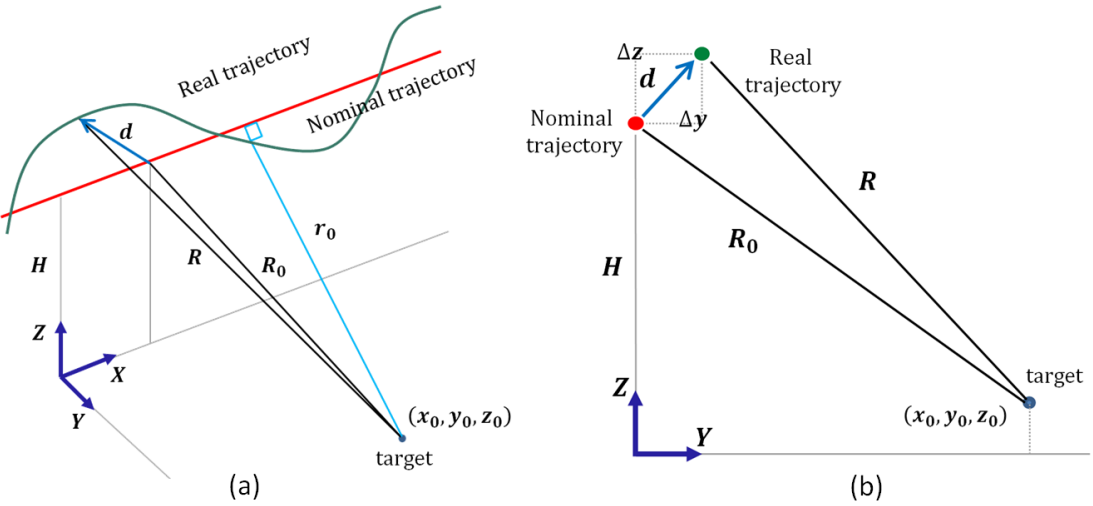


Figure 4.4: (a) SAR geometry, and (b) normal plane of the ideal trajectory.

on the ideal path to find the error for compensation. Using the GPS to Cartesian transform, we can find the real trajectory of SAR platform.

For time-domain reconstruction algorithms including TDC and BP, we can directly use the motion data to compensate the phase error. Here, the strip-map SAR geometry of Fig. 4.4 (a) is assumed. The instantaneous motion error vector  $d$ , defined by the displacement between the real and nominal trajectories, is  $[\Delta x(\eta), \Delta y(\eta), \Delta z(\eta)]$ , where  $\Delta y(\eta)$  and  $\Delta z(\eta)$  represent the cross-track displacement as shown in Fig. 4.4 (b). Knowing the coordinates of target  $(x_0, y_0, z_0)$ , the real trajectory, and the nominal trajectory, the distances  $R$  and  $R_0$  can be calculated from geometry:

$$\begin{aligned} R(\eta; x_0, y_0, z_0) &= \sqrt{(\nu \cdot \eta + \Delta x(\eta) - x_0)^2 + (\Delta y(\eta) - y_0)^2 + (H + \Delta z(\eta) - z_0)^2} \\ &= R_0(\eta; x_0, y_0, z_0) + \Delta R_0(\eta; x_0, y_0, z_0) \end{aligned} \quad (4.69)$$

$$R_0(\eta; x_0, y_0, z_0) = \sqrt{(\nu \cdot \eta - x_0)^2 + y_0^2 + (H - z_0)^2} \quad (4.70)$$

However, for frequency domain algorithms it is not possible to directly use the motion data for phase error correction. The traditional motion compensation method for RDA involves two steps. First, the corrections are calculated for a

reference range,  $R_{ref}$ , usually in the center of the swath. The first step of phase correction is as:

$$H_{mc_1} = \exp(j2\pi f_0 \Delta\tau_{ref}) \quad (4.71)$$

where  $\Delta\tau_{ref} = 2\Delta R_{ref}/c$ , and  $\Delta R_{ref} = R - R_{ref}$  ( $R$  and  $R_{ref}$  distances are respectively calculated from real and nominal trajectories to a target in the center of the swath).

Then, the SAR data is range-compressed. This is the center-beam approximation [24] and is used in many MC algorithms. A second order correction is applied to each range, according to the differential correction from the reference range. For each  $R$ ,  $\Delta R_0$  is calculated and the correction is formed as:

$$H_{mc_2} = \exp(j2\pi f_0(\Delta\tau_0 - \Delta\tau_{ref})) \quad (4.72)$$

This method introduces error after the range compression, which is not acceptable for a high-resolution SAR system. In this study, an efficient MC method is proposed to apply on the range-compressed data. The range-compressed signal of (4.68) can be obtained using matched filtering as follows:

$$\begin{aligned} s_{\Delta rc}(\tau, \eta) &= \mathcal{F}_{f_r}^{-1} \left\{ \mathcal{F}_t \{s_{\Delta rm}(t, \eta)\} \cdot \mathcal{F}_t \{\exp(-j\varphi(-t))\} \right\} \\ &= \mathcal{F}_{f_r}^{-1} \left\{ A \cdot B(f_r) \cdot \exp(-j2\pi(f_0 + f_r)(\tau_0 + \Delta\tau_0)) \right. \\ &\quad \left. \cdot \mathcal{F}_t \{\exp(j\varphi(t))\} \cdot \mathcal{F}_t \{\exp(-j\varphi(-t))\} \right\} \\ &= \mathcal{F}_{f_r}^{-1} \left\{ A \cdot B(f_r) \cdot \exp(-j2\pi f_r(\tau_0 + \Delta\tau_0)) \right. \\ &\quad \left. \cdot \mathcal{F}_t \{\exp(j\varphi(t))\} \cdot \mathcal{F}_t \{\exp(-j\varphi(-t))\} \right\} \cdot \exp(-j2\pi f_0(\tau_0 + \Delta\tau_0)) \\ &\approx p_r(\tau - (\tau_0 + \Delta\tau_0)) \cdot \exp(-j2\pi f_0(\tau_0 + \Delta\tau_0)) \end{aligned} \quad (4.73)$$

where  $\mathcal{F}_t \{s_{\Delta rm}(t, \eta)\}$  is obtained using (24),  $A$  is a constant,  $B(f_r)$  is a complex function which limits the values of  $\mathcal{F}_t \{s_{\Delta rm}(t, \eta)\}$  to within the bandwidth of the chirp ( $B(f_r)$  can be approximated by a Rect function), and  $p_r(\tau)$  is the compressed pulse envelope in the range direction. The simplification that gives the last line of

(43) is due to the fact that the multiplication in the frequency domain corresponds to convolution in the time domain. Therefore, the compressed pulse envelope  $p_r(\tau)$  is the result of the NLFM signal autocorrelation.

From (4.73) we can find a correction filter, which works on the range-compressed data as:

$$H(\tau, \eta) = \exp(j2\pi f_0 \Delta\tau_0) \quad (4.74)$$

After the filtering, the range-compressed data becomes:

$$s_{\Delta r c}(\tau, \eta) = p_r(\tau - (\tau_0 + \Delta\tau_0)) \exp(-j2\pi f_0 \tau_0) \quad (4.75)$$

For exactly removing phase error from data, an azimuth dependent interpolation should be used to compensate the range shift  $\Delta\tau_0$  due to motion error:

$$f_r - k_r(\tau_0 + \Delta\tau_0) \rightarrow f'_r - k_r \tau_0 \quad (4.76)$$

The mapping in (4.76) transforms the original range frequency variable  $f_r$  into the new range frequency variable,  $f'_r$ . In this manner, (4.75) can be obtained using:

$$s_{rc}(\tau, \eta) \approx p_r(\tau - \tau_0) \exp(-j2\pi f_0 \tau_0) \quad (4.77)$$

At the end, we have a range-compressed signal with phase error compensated. It should be mentioned that the proposed method can also be used for motion compensation of raw data from the pulsed and FMCW modes, which are based on LFM signal waveform.

## 4.5 Summary

In this Chapter, a new NLFM waveform is proposed, which can be used as a transmitted chirp in SAR imaging to improve the imaging quality compared to LFM chirp signal. Time domain signal processing algorithms (TDC and BP) and frequency domain methods (RDA and omega-K) are modified in order to use NLFM waveform as the transmitted chirp for SAR imaging. In addition, a modified

MC algorithm is developed for phase error compensation in NLFM waveform case.  
It can be used with RDA algorithm.

## Chapter 5. Autofocus algorithm based on flight trajectory optimization

In this Chapter, a new autofocus algorithm is presented for BP image formation of SAR imaging. The approach is based on maximizing an objective function obtained by prominent points in different sub-apertures of constructed SAR image by varying the flight trajectory parameters. While image-quality-based autofocus approach together with BP algorithm can be computationally intensive, we use approximations that allow optimal corrections to be derived. The approach is applicable for focusing different signal processing algorithms by obtaining modified flight trajectory parameters [61-62].

### 5.1 Introduction

Another subject that we have considered in this dissertation is a new autofocus algorithm working with BP image formation method. To improve the efficiency but to keep the advantages of BP algorithm, we present a new metric-based approach to modify the flight trajectory for BP imaging. This new method makes no assumption about the imaging geometry. Knowing the initial path of the SAR sensor using the navigation data, we can obtain the optimum trajectory by optimizing a proper objective function. The flight trajectory is modeled using polynomial functions in a three dimensional space. Specifically, we propose an approximate model to obtain the objective function for optimization without using BP algorithm in order to lower the computational complexity.

Constructions of very small SAR systems are possible by using a LFM-CW signal in the radar transmitter [7-12]. Combined with an analog dechirp in the receiver, these systems can be made with hardware which is simpler, cheaper, and consumes less power than the conventional pulsed SAR systems. This enables the use of low cost SARs on UAS, which makes possible SAR imagery to be obtained in harsh climates or in environments too dangerous for manned aircraft or expensive SAR systems. The motion error problem is particularly apparent to the UAS SAR, because it is easily disturbed by the atmospheric turbulence due to its small size and lightweight. Moreover, the UAS SAR may not be equipped with a highly accurate navigation system due to weight capacity restriction [13]. Therefore, for the UAS SAR imaging, MC strategies are important and advisable based on the raw data or autofocus. For this reason, we have considered SAR in LFM-CW mode for theoretical discussions; however, it can be generalized for pulsed mode SAR.

The remainder of this Chapter is organized as follows. The fundamental of SAR signal processing in LFM-CW mode is briefly reviewed in subsection 5.2. Subsection 5.3 gives the description of the MC using navigation data. In subsection 5.4, trajectory optimization for BP image formation is presented. Finally, a short summary is given in Section 5.5.

## 5.2 LFM-CW synthetic aperture radar signal processing

In this subsection, first we will describe how to model the transmitted and received signal based on LFM-CW. Then, back projection algorithm for image formation of received SAR signal is explained. SAR system illuminates the scene with a series of coherent pulses while passing by a target. The series of radar echoes from the target area are digitized and processed to form the image. Before the SAR signal is generated, a number of important system parameters should be determined, including carrier frequency, bandwidth, pulse length, and PRF. The transmitted signal is a LFM waveform, where the signal spans the bandwidth over

the pulse length. This cycle is repeated at the PRF. The SAR signal is usually generated at or near baseband and then mixed up to the desired operating frequency before transmission. The LFM transmit signal can be expressed as:

$$s_t(t) = A(t)\exp(j(2\pi f_0 t + \pi k_r t^2 + \varphi_0)) \quad (5.1)$$

where  $A(t)$  is the signal amplitude as a function of time  $t$  and defines the pulse length with a rect function,  $k_r$  is the chirp rate,  $f_0$  is the frequency at the beginning of the chirp, and  $\varphi_0$  is the starting phase which can usually be neglected.

In the transmission chain, a power amplifier increases the power to a specified level. The transmitted signal needs to have enough power so that the SNR is large enough to generate a good image. The amplified signal transmitted through the antenna propagates to the target area. A very small portion of the transmit signal is reflected back to the radar. By neglecting the time-scaling influences on the pulse envelope, the echoed signal from target can be expressed as:

$$s_r(t, \eta) = A'(t)\exp(j(2\pi f_0(t - \tau) + \pi k_r(t - \tau)^2 + \varphi_0)) \quad (5.2)$$

where  $t$  is fast time,  $\eta$  is slow time (or azimuth time), and  $A'(t)$  is an attenuated version of  $A(t)$  and  $\tau$  is the two-way time of flight to the target at range  $R$ . It should be mentioned that  $\tau$  is a function of  $t$  and  $\eta$  and is obtained using the following:

$$\tau(t, \eta) = \frac{2R(t, \eta)}{c} = \frac{2\sqrt{r_0^2 + (v(t + \eta) - x_0)^2}}{c} \quad (5.3)$$

where  $v$  is the platform velocity,  $r_0$  is the range of closest approach,  $x_0$  is target position in azimuth direction, and  $c$  is the light speed.

In the pulsed mode, the pulse duration is short about a few microseconds; however, for the LFM-CW mode, the pulse duration is about milliseconds, corresponding to the pulse repetition interval. Therefore, the number of samples for LFM-CW mode could be too many. The dechirp-on-receive technology is generally used in the LFM-CW SAR system to reduce the sampling requirements and data

rate [3, 63]. In LFM-CW SAR, the pulse length is maximized. Maximizing the pulse length maximizes the SNR for a given transmit power. This requires bistatic operation in which one antenna transmits and another antenna receives. One problem with this is that the direct feedthrough from the transmitter to the receiver can have much higher power than the radar echoes from the target area. This feedthrough must be managed to prevent it from drowning out the desired signal. The dechirp-on-receive converts the feedthrough to a single frequency that can be filtered out in hardware. The analog dechirp also offers some other advantages particularly useful for CW SAR: a reduced sampling bandwidth and a simplified range compression computation.

With an analog dechirp, the received signal is mixed with a copy of the transmit signal, and low-pass filtered in hardware, which is mathematically equivalent to multiplying (5.1) by the complex conjugate of (5.2). This results in the dechirped signal:

$$s_{dc}(t, \eta) = s_t \cdot s_r^* = A''(t) \exp(j(2\pi f_0 \tau + 2\pi k_r t \tau - \pi k_r \tau^2)) \quad (5.4)$$

SAR systems digitize this data and either store it on board, transmit it to a ground station, or process it on-board. The last exponential term of (5.4) is well known as the residual video phase (RVP) [3]. Removing the RVP needs Fourier transformation (FT), phase multiplication, and inverse FT [3]. For range compression of de-chirped LFM signal, only one FT is necessary [20]. Assuming no motion during the chirp is equivalent to assuming that  $R$  is not a function of  $t$ . Thus, the range-compressed signal is obtained using the following:

$$s_{rc}(f_r, \eta) = \int_{\tau}^{\tau+T} s_{dc}(t, \eta) \cdot \exp(-j2\pi f_r t) dt = T \cdot \text{sinc}(T(f_r - k_r \tau)) \cdot \exp(j\pi(k_r \tau T - f_r T + k_r \tau^2 + 2f_0 \tau - 2f_r \tau)) \quad (5.5)$$

where  $T$  is pulse width, and  $f_r$  is the frequency in range direction.

From (5.5), we can see that the RVP term  $\exp(-j\pi k_r \tau^2)$  has been removed after FT. Since the peak value of the range-compressed signal lies on  $f_r = k_r \tau$ , (5.5) can be simplified as follows:

$$s_{rc}(f_r, \eta) \approx T \cdot \text{sinc}(T(f_r - k_r \tau)) \cdot \exp(j\pi(2f_0 \tau - f_r \tau)) \quad (5.6)$$

In (5.6), there are two parts of phase item: one is the Doppler item, which is necessary for azimuth focusing, and the second part is slope factor, which not only affecting adding window in range, but also impacting the azimuth focusing. Thus, it must be compensated before azimuth compression. Let the de-sloping factor be:

$$\varphi_{ds}(f_r, \eta) = \exp(j\pi f_r \tau) \quad (5.7)$$

From (5.7), the de-sloping factor is linear with  $\tau$ , which means different compensation should be done with different slant range. However, the signal in range frequency domain is a Sinc function with very narrow width, the peak value lies on  $f_r = k_r t_d$ , so, the de-sloping factor can be written as:

$$\varphi_{ds}(f_r, \eta) \approx \exp(j\pi f_r^2 / k_r) \quad (5.8)$$

Multiplying (5.7) by (5.8), then transforming inversely to range time domain, the range de-sloping is finished.

$$\begin{aligned} s_{ds}(t, \eta) &\approx \int_0^\infty T \cdot \text{sinc}(T(f_r - k_r \tau)) \cdot \exp(j2\pi f_0 \tau) \cdot \exp(j2\pi f_r t) df_r \\ &\approx \exp(j2\pi f_0 \tau) \exp(j2\pi k_r t \tau) \end{aligned} \quad (5.9)$$

After de-sloping, the range compression can be accomplished by adding window and performing FT in range direction. Performing the time-frequency substitution of  $f_r = k_r t$ , the new range-compressed signal is obtained as follows:

$$s_{rc}(f_r, \eta) \approx \exp(j2\pi \tau(f_r + f_0)) \quad (5.10)$$

We approximate the FT using the POSP, which is valid except in the extreme case of having radar frequencies very close to zero. An expression for the signal phase after the azimuth FT is computed by adding the phase term  $-2\pi f_a \eta$  to (5.10), where  $\eta$  is azimuth frequency:

$$\phi = 2\pi\tau(f_r + f_0) - 2\pi f_a \eta = \frac{4\pi}{c} R(\eta)(f_r + f_0) - 2\pi f_a \eta \quad (5.11)$$

where

$$R(\eta) = \sqrt{r_0^2 + (\nu\eta - x_0)^2} \quad (5.12)$$

Take the derivative of the phase with respect to  $\eta$ , and solve for  $\eta$  at the point where the phase is stationary (i.e. where  $d\phi/d\eta = 0$ ).

$$\frac{d\phi}{d\eta} = \frac{\frac{4\pi(f_r+f_0).(\nu^2\eta-\nu.x_0)}{c\sqrt{r_0^2+(\nu.\eta-x_0)^2}} - 2\pi f_a}{0} = 0 \quad (5.13)$$

The stationary point is found by solving for  $\eta$

$$\eta = \frac{\frac{f_a.c.r_0}{\nu\sqrt{-f_a^2c^2+4(f_r+f_0)^2\nu^2}} + \frac{x_0}{\nu}}{} \quad (5.14)$$

Substitute into (5.11) and simplify to obtain the signal phase after the azimuth FT.

$$\phi = -\frac{2\pi r_0}{\nu c} \sqrt{-f_a^2 c^2 + 4(f_r + f_0)^2 \nu^2} - \frac{2\pi f_a x_0}{\nu} \quad (5.15)$$

The exponential that makes up the signal in 2-D frequency domain can be expressed as:

$$s_{2d}(f_r, f_a) \approx \exp \left( -j \left( \frac{2\pi r_0}{\nu c} \sqrt{-f_a^2 c^2 + 4(f_r + f_0)^2 \nu^2} + \frac{2\pi f_a x_0}{\nu} \right) \right) \quad (5.16)$$

### 5.2.1 Time domain signal processing algorithms

In this subsection, we focus on time-domain reconstruction algorithms for LFM-CW SAR. The main advantage of these algorithms when compared with frequency-domain algorithms is their natural use of the available information on the sensor's trajectory, which makes them best suited when facing highly nonlinear trajectories of the platform [32].

Time-domain correlation (TDC) algorithm uses the raw data directly, without range-compression. The platform position for each sample of raw data is used. In this case, SAR image from a point target is formed using the following formula:

$$im(y_0, x_0, z_0) = \sum_t \sum_\eta s_{dc}(t, \eta) \exp(j\Phi_{\tau_0}(t, \eta)) \quad (5.17)$$

where  $(x_0, y_0, z_0)$  is the coordinate of the point target,  $\Phi$  is the conjugate of the signal phase in (5.4), and  $\tau_0$  is obtained using the following:

$$\tau_0(t, \eta) = \frac{2R(t, \eta)}{c} = \frac{2\sqrt{(H-z_0)^2 + y_0^2 + (v(t+\eta)-x_0)^2}}{c} \quad (5.18)$$

where  $v$  is the platform velocity,  $H$  is the flight altitude and  $c$  is the light speed.

This is a very exact method, but it is very computationally taxing, which is rarely used in practice. However, it is important, because it gives a reference for measuring the imaging quality of other reconstruction algorithms.

Since the TDC algorithm is computationally intensive for practical purposes, it is natural to use approximations, which reduce the cost of the algorithm. BP normally operates on the range-compressed data. For dechirped SAR, interpolation and range compression can be performed by means of zero-padding and a range FT. Using the start and stop approximation,  $\tau_0$  does not depend in fast time  $t$ , and we can rewrite (5.18) as:

$$im(y_0, x_0, z_0) = \sum_\eta \exp(-j2\pi f_0 \tau_0) \exp(j\pi k_r \tau_0^2) \sum_t s_{dc}(t, \eta) \exp(-j2\pi k_r \tau_0 t) \quad (5.19)$$

Using the definition of discrete FT, we can obtain the following formula:

$$im(x_0, y_0, z_0) = \sum_{\eta} s_{rc}(k_r \tau_0, \eta) \cdot \exp(-j2\pi f_0 \tau_0) \cdot \exp(j\pi k_r \tau_0^2) \quad (5.20)$$

where  $s_{rc}$  is the range-compressed SAR data using range FT, interpolated to  $k_r \tau_0$ .

The benefits of BP include the simplicity of the algorithm, the parallel computation structure, and the ability to process data from an arbitrary platform path. The shortcomings are that the motion of the platform must be precisely known and the algorithm is very computationally taxing. However, using the parallel nature of the algorithm and the parallel processing of modern general-purpose graphic processor units can significantly improve the processing time.

### 5.2.2 Frequency domain signal processing algorithm

The most frequently used algorithm for SAR signal processing is the RDA [2]. It was developed for processing SEASAT SAR data in 1978. There are three main steps to correctly focusing the data using RDA: range compression, range cell migration correction, and azimuth compression. In order to use RDA for processing the raw signal, we rewrite (5.16) as:

$$s_{2d}(f_r, f_a) \approx \exp\left(-j\left(\frac{4\pi r_0 f_0}{c} \sqrt{D^2(f_a) + \frac{2f_r}{f_0} + \left(\frac{f_r}{f_a}\right)^2} + \frac{2\pi f_a x_0}{v}\right)\right) \quad (5.21)$$

where

$$D(f_a) = \sqrt{1 - \left(\frac{cf_a}{2vf_0}\right)^2}$$

The RDA is obtained as a result of using Taylor series approximation of (5.21). The square root term in (5.21) can be expanded as:

$$\Gamma(f_r) = \sqrt{D^2(f_a) + \frac{2f_r}{f_0} + \left(\frac{f_r}{f_0}\right)^2} \approx \Gamma(0) + \frac{\Gamma'(0)}{1!} f_r + \frac{\Gamma''(0)}{2!} f_r^2 + \frac{\Gamma'''(0)}{3!} f_r^3 + \dots \quad (5.22)$$

The RDA keeps up to the first order term,

$$\emptyset_{\text{RDA}} = - \left( \frac{4\pi r_0 f_0}{c} \left[ D(f_a) + \frac{f_r}{f_0 \cdot D(f_a)} \right] + \frac{2\pi \cdot f_a x_0}{v} \right) \quad (5.23)$$

which makes the algorithm relatively simple. Using this approximation, the inverse FT of (5.21) in range direction give us the signal in the range-Doppler domain:

$$s_{rd}(\tau, f_a) \approx p_r \left( \tau - \frac{2r_0}{c \cdot D(f_a)} \right) \cdot \exp \left( -j \left( \frac{4\pi r_0 f_0}{c} D(f_a) + \frac{2\pi \cdot f_a x_0}{v} \right) \right) \quad (5.24)$$

As it can be seen from (5.24), the target is compressed in range direction with the curved trajectory  $r(f_a)$ , which is called the range cell migration:

$$r(f_a) = \frac{r_0}{D(f_a)} \quad (5.25)$$

To compensate the range cell migration so that all the energy returned form a target is contained in the single range bin  $r_0$ , an azimuth frequency dependent interpolation should be used, shifting the trajectories by  $r(f_a) - r_0$ . Azimuth compression is performed using a MF with the Doppler chirp. With the SAR signal range-compressed and the range cell migration removed, the signal can be expressed in the range-Doppler domain as:

$$s_{rd}(\tau, f_a) \approx p_r \left( \tau - \frac{2r_0}{c} \right) \cdot \exp \left( -j \left( \frac{4\pi r_0 f_0}{c} D(f_a) + \frac{2\pi \cdot f_a x_0}{v} \right) \right) \quad (5.26)$$

The azimuth chirp is range dependent, so the MF is recalculated for each range bin. The MF is applied by multiplying the signal by the following:

$$H_{az}(r_0, f_a) = \exp \left( j \frac{4\pi r_0 f_0}{c} D(f_a) \right) \quad (5.27)$$

After azimuth MF, the remaining signal becomes:

$$S'_r(\tau, f_a) = p_r \left( \tau - \frac{2r_0}{c} \right) \cdot \exp \left( -j \frac{2\pi \cdot f_a x_0}{v} \right) \quad (5.28)$$

An inverse azimuth FT returns the signal to the time domain where the targets are now fully compressed:

$$im(\tau, \eta) = p_r \left( \tau - \frac{2r_0}{c} \right) \cdot p_a \left( \eta - \frac{x_0}{v} \right) \quad (5.29)$$

One drawback of RDA is a computationally taxing interpolation to correct the range cell migration. Another limitation is the incapability to handle squint-mode or wide-beam SAR. However, there is a modification to the RDA, which can help by introducing a secondary range-compression (SRC). The SRC keeps an additional term of a Taylor series approximation of (5.22) in the phase function, but only at a reference range [2].

### 5.3 Motion compensation using navigation data

The SAR processing method described in previous subsection assume that the platform moves at a constant speed in a straight line. Translational motion causes a platform displacement from the nominal, ideal path as shown in Fig. 5.1 (a). This results in the target scene changing in range during data collection. This range shift also causes inconsistencies in the target phase history. A target located at range  $R_0$ , measured at range  $R = R_0 + \Delta R_0$  results in a phase error in dechirped signal as:

$$s_{\Delta dc}(t, \eta) = A''(t) \exp(j(2\pi f_0(\tau_0 + \Delta\tau_0) + 2\pi k_r t(\tau_0 + \Delta\tau_0) - \pi k_r(\tau_0 + \Delta\tau_0)^2)) \quad (5.30)$$

where  $\tau_0 = 2R_0/c$ , and  $\Delta\tau_0 = 2\Delta R_0/c$ .

#### 5.3.1 Flight trajectory estimation using GPS data

The motion errors can be compensated if the platform motion is measured using an on-board INS/GPS sensor. In general, the motion data is collected at a much slower rate than the SAR data. The motion data must be interpolated so that every sample of SAR data has corresponding position information. Each data point also needs to have a corresponding location on the ideal path to find the error for compensation. Using the GPS to Cartesian transform, we can find the real

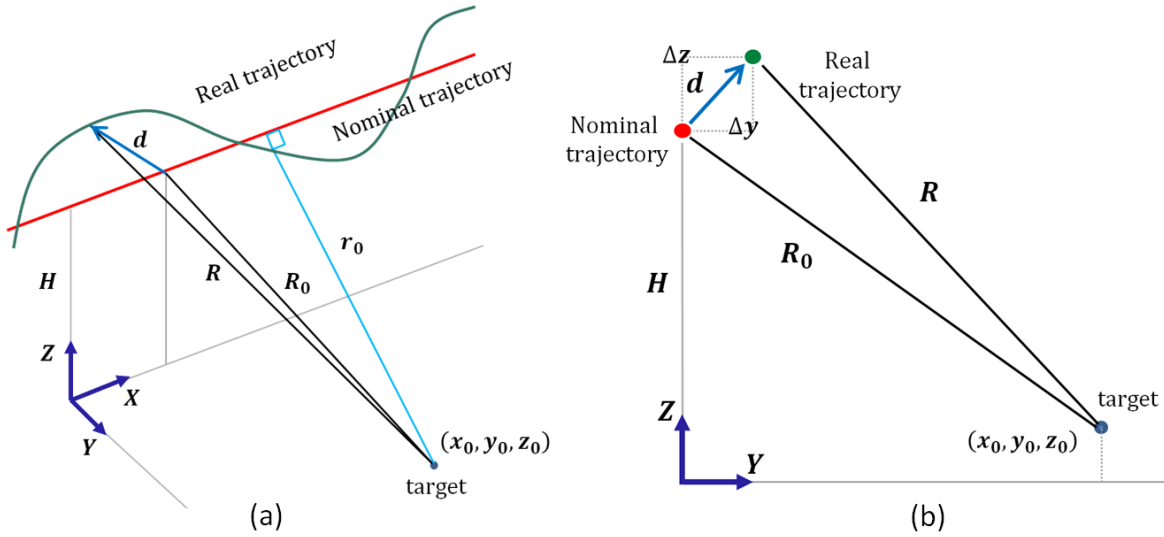


Figure 5.1: (a) Stripmap SAR geometry, (b) Normal plane of the ideal trajectory.

trajectory of SAR platform. Fig. 5.2 shows a sample of 10 Hz GPS data and corresponding flight trajectory in three-dimensional space. The flight trajectory obtained by GPS to Cartesian transform has two evident problems: 1) fluctuations of flight trajectory because of GPS error, and 2) altitude bias, because the height information is relative to sea level. These two problems should be resolved for MC. A common and completely reasonable response in selecting an interpolation strategy for improving motion data is to use the following:

$$C(t) = A_0 + A_1 t + A_2 t^2 + A_3 t^3 + \dots + A_N t^N \quad (5.31)$$

a simple polynomial as the analytic function approximating the data in the interpolator [64-65]. Here,  $C$  represents the  $X$ ,  $Y$ , or  $Z$  coordinate value,  $t$  is time and  $A_0$  through  $A_N$  are the coefficients of the polynomial, which are adjusted to fit the measured motion data.

The values of the coefficients will be determined by fitting the polynomial to the source data. This can be done by minimizing an error function that measures the misfit between the  $C(t)$  (for any given value of  $A$ ) and the source data points. One simple choice of error function, which is widely used, is given by the sum of the squares of the errors. There remains the problem of choosing the order  $N$  of the

polynomial, which affects the result of phase error compensation. Here, we have used a metric-based approach to automatically determine the polynomial order, which will be described in next subsection.

In addition to polynomial fitting, we have used nadir return to improve the height estimation and remove GPS altitude bias. Note that SAR platform travels forward in the flight direction with the nadir directly beneath the platform. The platform height can be accurately estimated from the range-compressed SAR data. To illustrate, Fig. 5.3 plots a sample of range-compressed data. The nadir echo is evident in the range-compressed data where it corresponds to the top of the horizontal dark band in the plot. Note that there is no return signal for slant ranges shorter than the platform height. In the following, the theoretical treatment of full MC using navigation data for RDA is described.

### 5.3.2 Full motion compensation using flight trajectory information

For time-domain reconstruction algorithms including TDC and BP, we can directly use the motion data to compensate the phase error. Here, the strip-map SAR geometry of Fig. 5.1 (b) is assumed. The instantaneous motion error vector  $d$ , defined by the displacement between the real and nominal trajectories, is  $[\Delta x(\eta), \Delta y(\eta), \Delta z(\eta)]$ , where  $\Delta y(\eta)$  and  $\Delta z(\eta)$  represent the cross-track displacement as shown in Fig. 5.1 (b). Knowing the coordinates of target  $(x_0, y_0, z_0)$ , the real trajectory, and the nominal trajectory, the distances  $R$  and  $R_0$  can be calculated from geometry:

$$\begin{aligned} R(\eta; x_0, y_0, z_0) &= \sqrt{(v\eta + \Delta x(\eta) - x_0)^2 + (\Delta y(\eta) - y_0)^2 + (H + \Delta z(\eta) - z_0)^2} \\ &= R_0(\eta; x_0, y_0, z_0) + \Delta R_0(\eta; x_0, y_0, z_0) \end{aligned} \quad (5.32)$$

$$R_0(\eta; x_0, y_0, z_0) = \sqrt{(v\eta - x_0)^2 + y_0^2 + (H - z_0)^2} \quad (5.33)$$

However, for frequency domain algorithms it is not possible to directly use the motion data for phase error correction. The traditional MC method for RDA

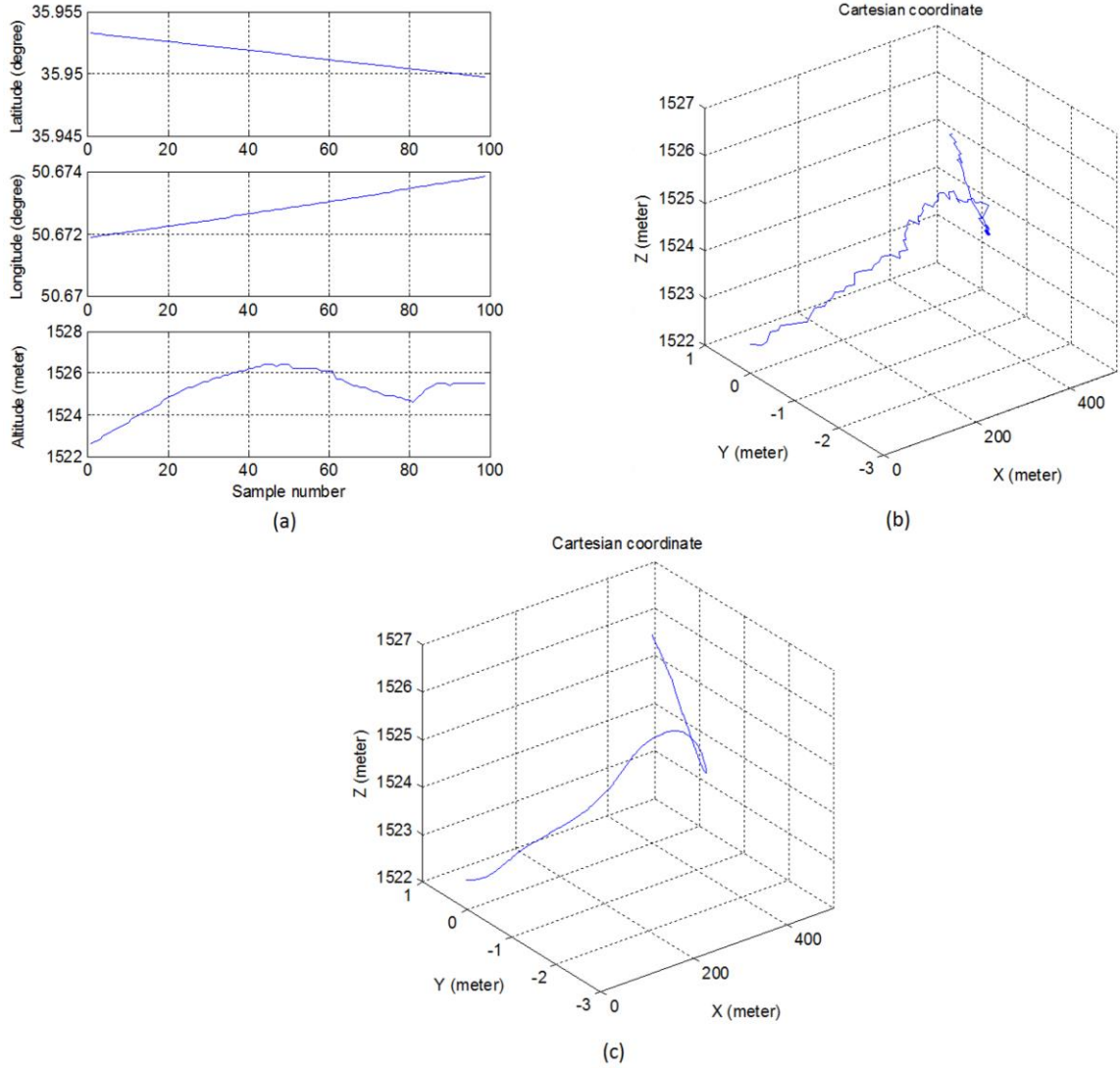


Figure 5.2: (a) A sample of 10 Hz GPS data for 10 seconds flight, (b) corresponding flight trajectory, and (c) flight trajectory after fitting 10-order polynomial functions.

involves two steps. First, the corrections are calculated for a reference range,  $R_{ref}$ , usually in the center of the swath. The first step of phase correction is as:

$$H_{mc_1} = \exp(-j2\pi f_0 \Delta\tau_{ref}) \quad (5.34)$$

where  $\Delta\tau_{ref} = 2\Delta R_{ref}/c$ . Then, the SAR data is range-compressed. This is the center-beam approximation [2] and is used in many MC algorithms. A second order correction is applied to each range, according to the differential correction from the reference range. For each  $R$ ,  $\Delta R$  is calculated and the correction is formed as:

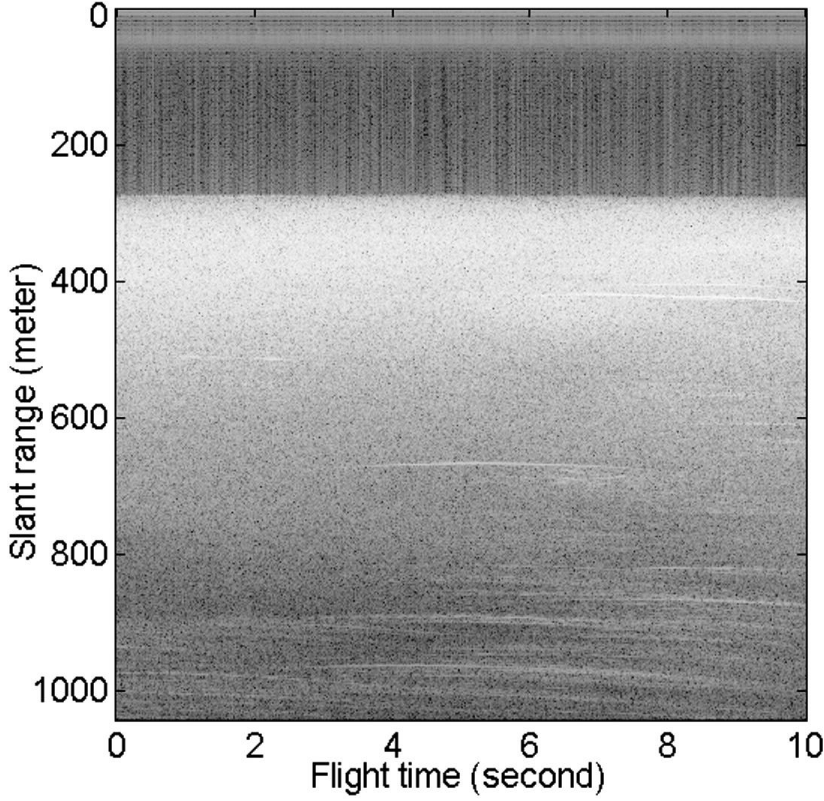


Figure 5.3: Range-compressed data with nadir return at top of the image (slant range extends from the top of the image).

$$H_{mc_2} = \exp(j2\pi f_0(\Delta\tau_0 - \Delta\tau_{ref})) \quad (5.35)$$

This method introduces error after the range compression, which is not acceptable for a high-resolution SAR system. In this study, an efficient MC method is proposed to apply on the range-compressed data. The range-compressed signal of (5.30) can be obtained using FT as follows:

$$s_{\Delta rc}(f_r, \eta) \approx T \cdot \text{sinc}\left(T(f_r - k_r(\tau_0 + \Delta\tau_0))\right) \cdot \exp\left(j\pi(2f_0(\tau_0 + \Delta\tau_0) - f_r(\tau_0 + \Delta\tau_0))\right) \quad (5.36)$$

Since the peak value of the range compressed signal lies on  $f_r = k_r(\tau_0 + \Delta\tau_0)$ , (5.36) can be simplified as follows:

$$s_{\Delta rc}(f_r, \eta) \approx T \cdot \text{sinc}\left(T(f_r - k_r(\tau_0 + \Delta\tau_0))\right) \cdot \exp(j\pi(2f_0(\tau_0 + \Delta\tau_0) - k_r(\tau_0 + \Delta\tau_0)^2)) \quad (5.37)$$

From (5.37) we can find a correction filter, which works on the range-compressed data as:

$$H_{mc}(f_r, \eta) = \exp(j\pi(-2f_0\Delta\tau_0 + k_r\Delta\tau_0^2 + 2k_r\tau_0\Delta\tau_0)) \quad (5.38)$$

After the filtering, the range-compressed data becomes:

$$s_{\Delta rc}(f_r, \eta) \approx T \cdot \text{sinc}\left(T(f_r - k_r(\tau_0 + \Delta\tau_0))\right) \cdot \exp(j\pi(2f_0\tau_0 - k_r\tau_0^2)) \quad (5.39)$$

For exactly focusing the data, an azimuth dependent interpolation should be used to compensate the range shift due to motion error. This is similar to the Stolt interpolation applied in omega-k algorithm [23]. The interpolation is defined as:

$$f_r - k_r(\tau_0 + \Delta\tau_0) \rightarrow f'_r - k_r\tau_0 \quad (5.40)$$

To achieve perfect range compression and registration, the mapping in (39) transforms the original range frequency variable  $f_r$  into the new range frequency variable,  $f'_r$ . By doing this, (5.39) can be expressed as:

$$\tilde{s}_{rc}(\tau, \eta) \approx T \cdot \text{sinc}\left(T(f_r - k_r\tau_0)\right) \cdot \exp(j\pi(2f_0\tau_0 - k_r\tau_0^2)) \quad (5.41)$$

At the end, we have a range-compressed signal with compensated phase error.

## 5.4 Trajectory optimization for BP image formation

In this subsection, the proposed autofocus method for BP image formation is presented. We first derive the general autofocus model for the BP algorithm. Then, the general model is approximated using the RDA to improve the computational complexity.

### 5.4.1 General autofocus model

The proposed autofocus model is based on trajectory optimization using prominent points (PPs) in different sub-apertures of constructed SAR image. This

new method makes no assumption about the imaging geometry. Knowing the initial path of the SAR sensor using the navigation data, we can obtain the optimum trajectory by optimizing a proper objective function. Specifically, the proposed autofocus method involves analysis of the formed image (i.e., range and azimuth compressed) in order to estimate proper correction factors to modify flight trajectory. Fig. 5.4 gives block diagram of the proposed autofocus for BP algorithm. The flight trajectory optimization is composed of the following essential steps:

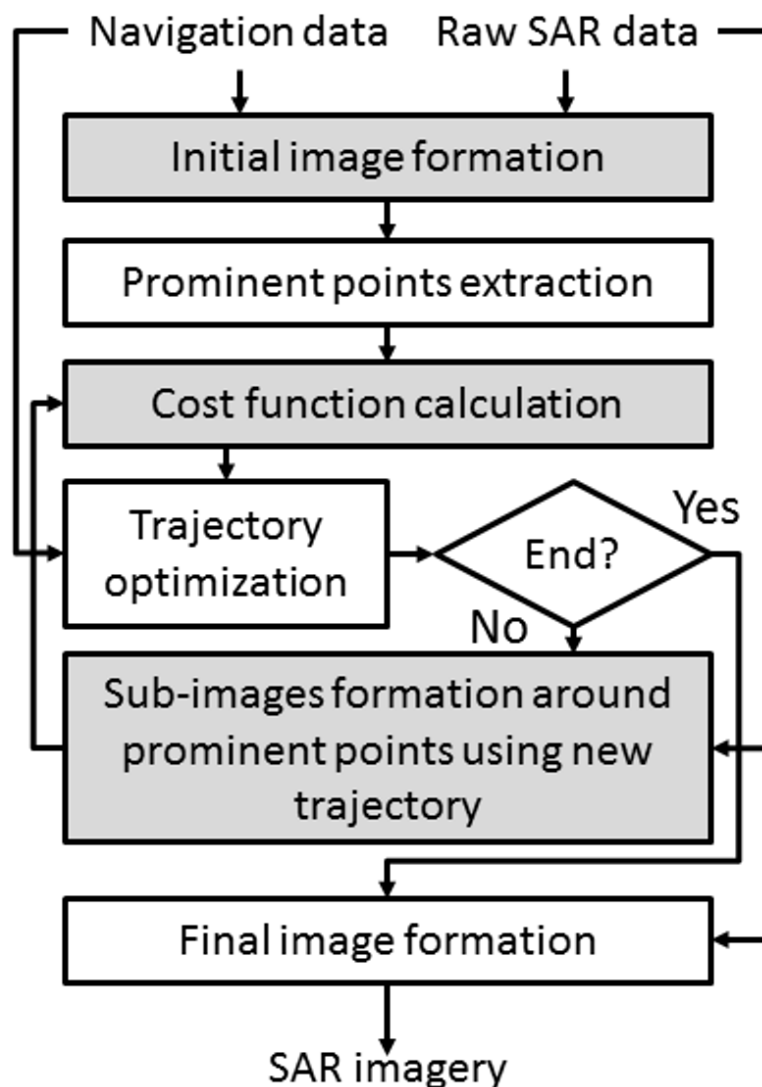


Figure 5.4: Block diagram of the proposed autofocus for BP algorithm using navigation and SAR raw data.

**Initial image formation:** In first step, an initial SAR image is formed using BP algorithm. BP algorithm formulated in (5.20) uses complex raw SAR data and initial flight trajectory. Initial flight trajectory is obtained from the navigation data by GPS to Cartesian transform after two modifications, which are described in subsection 5.3.

**Prominent points extraction:** In this step, the initial SAR image is divided by N sub-apertures and in each sub-aperture, one PP is selected. First, the initial SAR image is smoothed by a Gaussian filter and de-speckled by median filtering. Then, local maximums are obtained in each sub-aperture. Finally, a point with maximum average peak-side-lobe level-ratio (PSLR) in both azimuth and range directions is selected as a PP in each sub-aperture.

The PPs are used to obtain the objective function in the trajectory optimization process. The objective function should be a function of different parts of flight trajectory. For this reason, we have considered different sub-apertures for selecting PPs. PPs selection can also be extended to different range blocks for improving the objective function calculation. Specifically, we can divide SAR image into N sub-apertures and M range blocks. In this way, we can use more than one PP in each sub-aperture for objective function calculation.

**Objective function calculation:** After finding the PPs in the SAR image, a objective function is obtained for flight trajectory optimization. Phase error collected in SAR raw data due to non-linear flight trajectory, in one-hand results in widening the target response in azimuth direction, and in another hand results in lowering the target peak level. Therefore, a proper objective function should consider these effects.

It can be shown theoretically that a SAR image has its maximum amplitude without any phase error. The magnitude of a point target of a SAR image with phase error using BP algorithm can be written as follows:

$$\begin{aligned}
im(x_0, y_0, z_0) &= \sum_{\eta} |s_{\Delta rc}(k_r \tau_0, \eta) \cdot \exp(-j2\pi f_0 \tau_0) \exp(j\pi k_r \tau_0^2)| = \sum_{\eta} |s_{\Delta rc}(k_r \tau_0, \eta)| \\
&\sum_{\eta} \left| \sigma_0 \cdot T \cdot \text{sinc}\left(T(k_r \tau_0 - k_r(\tau_0 + \Delta\tau_0))\right) \cdot \exp\left(j\pi(2f_0(\tau_0 + \Delta\tau_0) - k_r \tau_0(\tau_0 + \Delta\tau_0))\right) \right| = \\
&\sum_{\eta} \left| \sigma_0 \cdot T \cdot \text{sinc}\left(T(k_r \tau_0 - k_r(\tau_0 + \Delta\tau_0))\right) \right| = \sum_{\eta} |\sigma_0 \cdot T \cdot \text{sinc}(T(-k_r \Delta\tau_0))| \quad (5.42)
\end{aligned}$$

where  $\sigma_0$  is the radar cross section of point target at coordinate  $x_0, y_0, z_0$ ,  $T$  is pulse width,  $\tau_0$  is delay to target,  $k_r$  is chirp rate, and  $\Delta\tau_0$  is phase error.

Since the Sinc function has its maximum value at zero, the resulting magnitude of (5.42) is decreased because of the phase error  $\Delta\tau_0$ . It can be concluded that the target peak level is proportional with phase error and should be included in objective function calculation. It is well known that the phase error causes target defocus in azimuth direction as it can be seen in Fig. 5.5 [46-47]. The target defocus can be measured by integrated sidelobe level ratio (ISLR), which is the ratio between the energy of the main-lobe and that integrated over several (usually 10-20 dB) side-lobes on both sides of the main one. The proposed objective function is defined in order to consider both target peak and target defocus as follows:

$$\text{Objective} = \frac{1}{N} \sum_{i=1}^N PP_i \times \text{ISLR}(PP_i) \quad (5.43)$$

where  $PP_i$  is the absolute values of PPs in SAR image, ISLR is calculated with center of PPs in azimuth direction, and  $N$  is the number of PPs.

It should be mentioned that the locations of PPs are updated in each iteration of optimization algorithm. It is simply performed by selecting the maximum values in a neighborhood around previous PPs locations.

**Trajectory optimization:** In this step, flight trajectory is optimized using the maximization of the objective function defined by (5.43). To aim this, we have modeled the flight trajectory by polynomial functions:

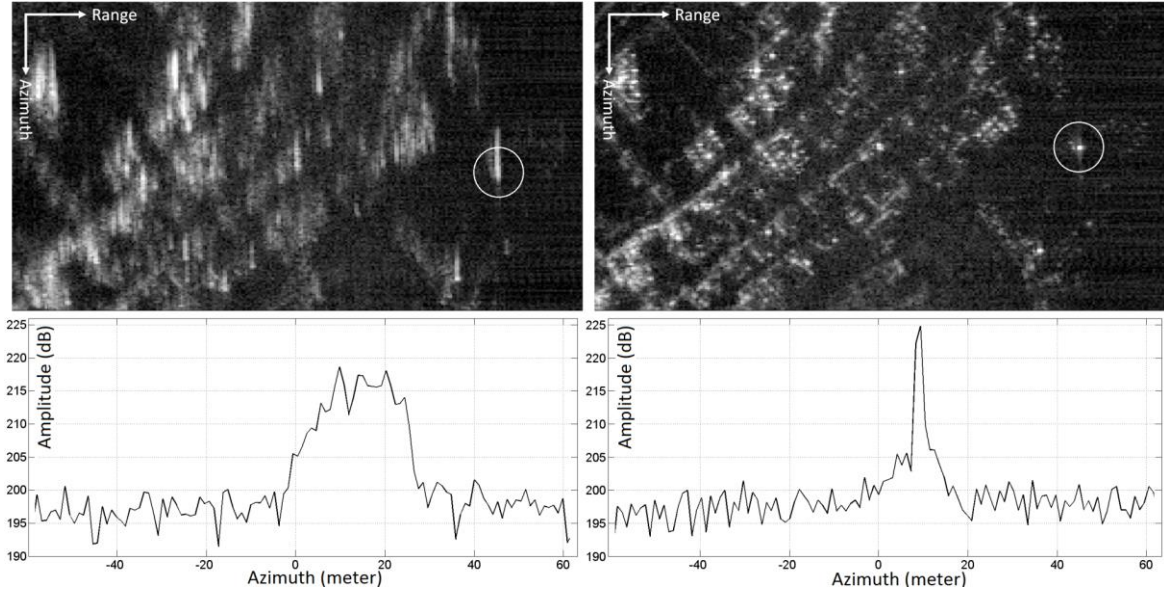


Figure 5.5: Top row: (left) degraded, and (right) focused SAR image, bottom row, azimuth profiles of point targets highlighted in white circles.

$$\begin{aligned} X(t) &= X_0(t) + \sum_{i=1}^{N_x} P_x(i) \cdot t^i & Y(t) &= Y_0(t) + \sum_{i=1}^{N_y} P_y(i) \cdot t^i \\ Z(t) &= Z_0(t) + \sum_{i=1}^{N_z} P_z(i) \cdot t^i \end{aligned} \quad (5.44)$$

where  $t$  is the flight time  $0 < t < t_f$ ,  $P_x, P_y$  and  $P_z$  are polynomial parameters, and  $X_0, Y_0$  and  $Z_0$  are initial flight trajectory obtained by navigation data.

Using the model expressed in (5.44), we have  $P_x + P_y + P_z$  parameters to be optimized. Here, we have used the genetic algorithm (GA) for the optimization problem [66]. This maximization is supposed to be accomplished while satisfying the following constraints:

$$|X(t_f) - X_0(t_f)| \leq Th_x, |Y(t_f) - Y_0(t_f)| \leq Th_y, |Z(t_f) - Z_0(t_f)| \leq Th_z \quad (5.45)$$

where  $Th_x, Th_y$  and  $Th_z$  are some thresholds.

The constraints are considered in the optimization for avoiding large changes in the trajectory.

**Sub-images formation:** After the first iteration of optimization, there is no need to form the whole SAR image for cost function calculation. Only the sub-images

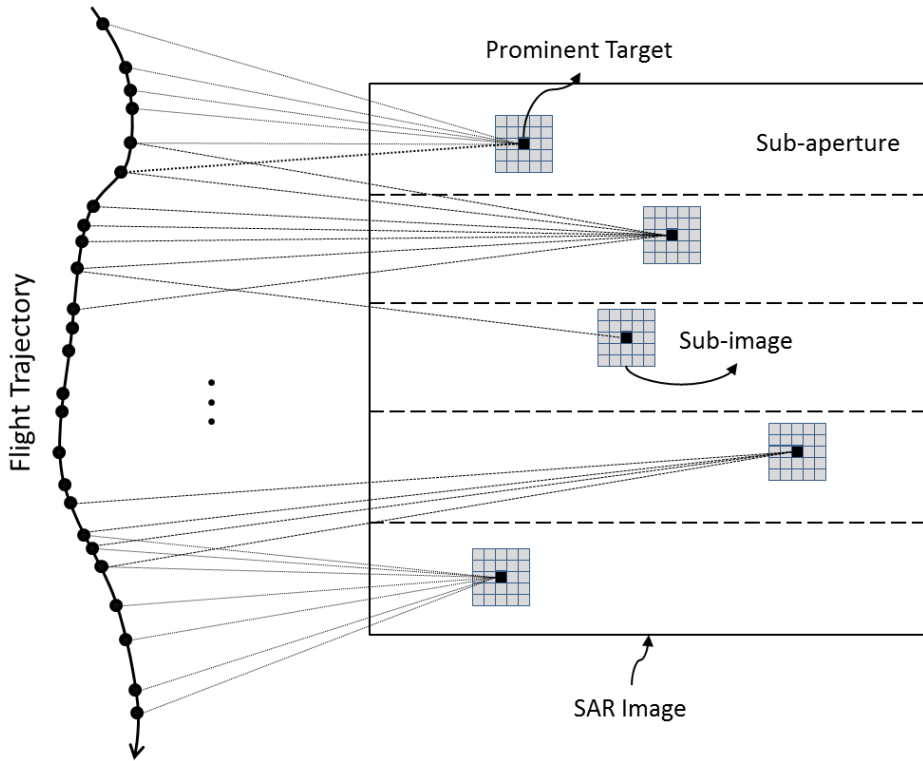


Figure 5.6: Graphical representation of forming the sub-images in different sub-apertures using BP algorithm.

around the PPs are constructed using the BP algorithm. Fig. 5.6 gives the graphical representation of forming the sub-images in different sub-apertures using BP algorithm. After forming the sub-images, maximum absolute values around previous locations of PPs are considered as new PPs, and objective function is obtained by (5.43).

**Final image formation:** After a predefined iteration, final SAR image is formed using the optimized flight trajectory and BP algorithm.

#### 5.4.2 Approximate model

The general autofocus model for BP algorithm is derived in the first part. However, this model is not efficient in term of computational complexity. In this part, we focus on the approximations of the general autofocus model, which is mainly based on RDA instead of BP algorithm. We have presented the flowchart of

the proposed model in Fig. 5.7. For the clarity of the proposed algorithm for flight trajectory optimization, we have employed a feasible procedure as follows:

**Initial image formation:** In this step, RDA together with MC are used to generate an initial SAR image for autofocus algorithm. In contrast with the general model, we have used BP algorithm to do the same. The details about the RDA and MC are described in subsection 5.3.

**Prominent points extraction and range bins selection:** Similar to the general model, a number of PPs are selected in SAR image for cost function calculation in the optimization loop.

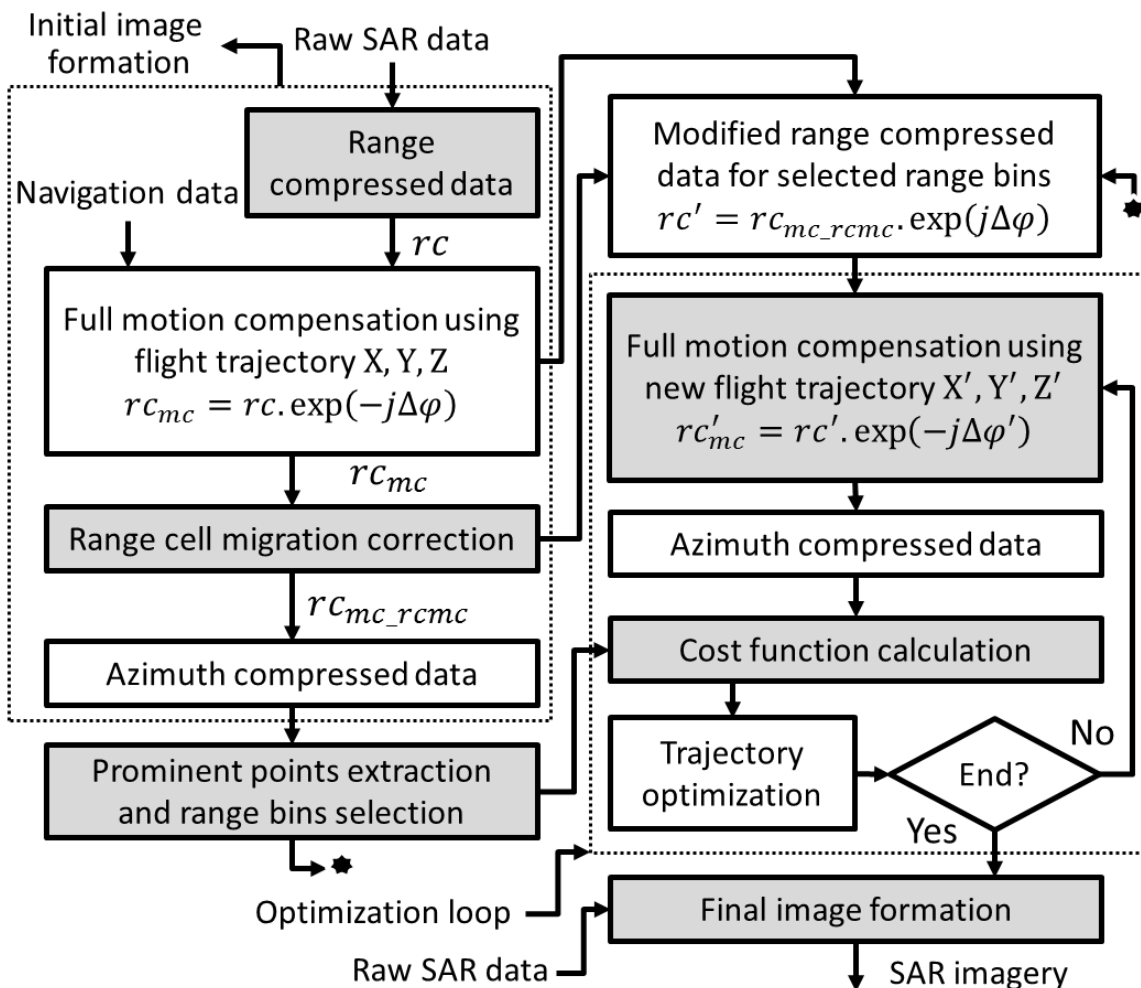


Figure 5.7: Flowchart of the proposed autofocus method.

**Modified range compressed data:** In this step, we have used an inverse procedure after range-cell-migration-correction step in RDA to obtain a modified range-compressed data. By doing this; we can approximately cancel RCM effect in the range-compressed data. In addition, we have only considered range bins around each PP to calculate modified range-compressed data. These two mentioned modifications, decrease computational complexity of generating SAR image in the optimization loop.

**Optimization loop:** In the optimization loop, we need to generate a SAR image to compute the objective function in order to optimize the flight trajectory. By knowing the position of the PPs in the initial SAR image, we can calculate the objective function in the new SAR image, which is obtained by updated flight trajectory. Objective function calculation and trajectory optimization are similar to the general model case.

**Final image formation:** After a predefined iteration, the final SAR image is formed using the optimized flight trajectory and BP algorithm.

For better understanding, step-by-step implementation of the proposed autofocus algorithm for a sample LFM-CW SAR data is demonstrated in Fig. 5.8. Clearly, when compared with the general autofocus model, the computational load of the approximate method is much lower. This autofocus method is advantageous because it requires no general assumptions of platform motion in order to operate. Other methods of autofocus typically only operate on spotlight mode data. In addition, this new method can be used for both time and frequency domain algorithms by providing optimized flight trajectory.

As we have mentioned in previous subsection, the order  $N$  of polynomial in (5.31) should be selected to obtain initial motion data. Here, we have used the same procedure for flight trajectory optimization in order to determine the order of polynomial for initial trajectory. Specifically, we first run the algorithm for

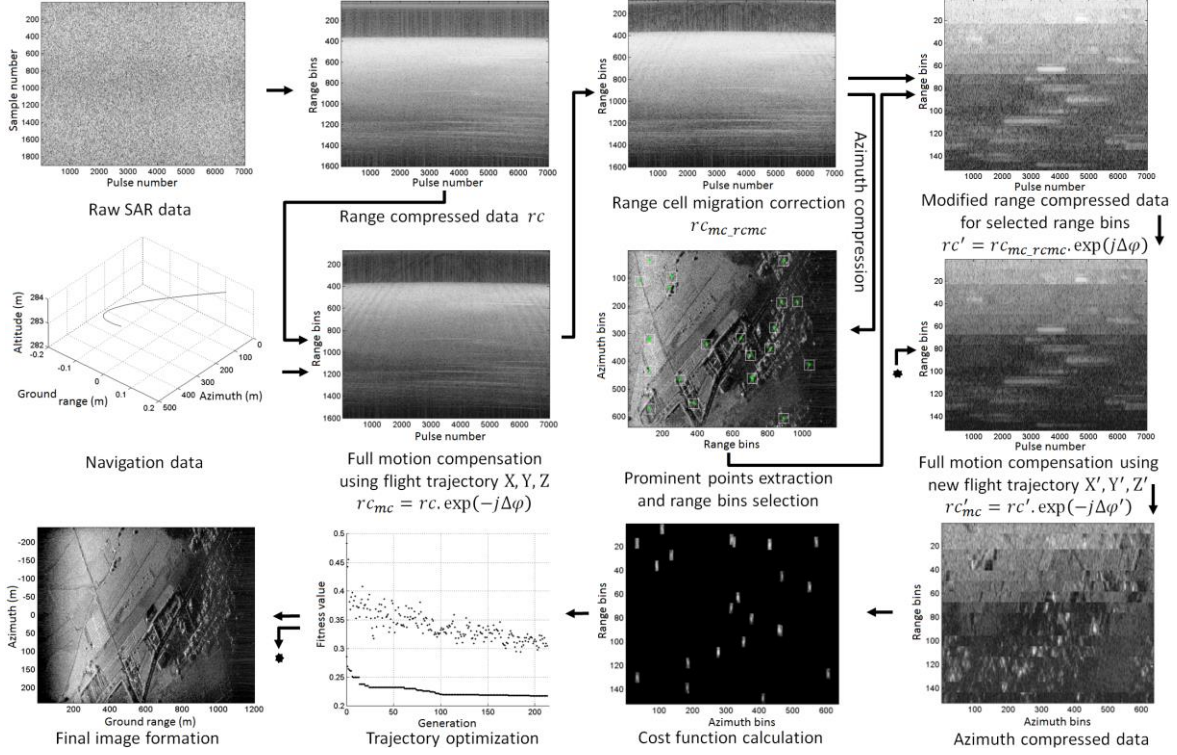


Figure 5.8: Graphical representation of the proposed autofocus algorithm.

determining the initial trajectory in (5.44), and then apply the phase error model for trajectory optimization.

### 5.4.3 Genetic optimization

Having the flight trajectory model, cost function, and constraints, we need an optimization algorithm to optimize the trajectory. Over the years, many real-parameter optimization algorithms have been developed by using point-by-point [67-68] as well as multi-point approaches [66, 69]. While a point-by-point approach begins with one guessed solution and updates the solution iteratively for reaching near the optimum solution, a multi-point method deals with a number of solutions in each iteration. Starting with a number of guessed solutions, the multi-point algorithm updates one or more solutions in a synergistic way for steering the population toward the optimum.

In this dissertation, we have considered GA for the optimization problem [66]. GA is inspired by the nature, and has proved itself to be effective solution to optimization problems. Appropriate setting of control parameters of GA is a key point for its success. In general, some forms of trial-and-error tuning are necessary for each particular instance of optimization problem. In this subsection, we briefly describe GA.

In GA [66], a candidate solution for a specific problem is called an individual or a chromosome and consists of a linear list of genes. Each individual stands for a point in the search space, and therefore a possible solution to the problem. A population consists of a finite number of individuals. Each individual is decided by an evaluating system to obtain its fitness value. Based on this fitness value and undergoing genetic operators, a new population is iteratively generated with each successive population referred to as a generation. Three basic genetic operators are sequentially applied to each individual with certain probabilities during each generation, i.e. selection, crossover (recombination), and mutation. First, a number of best individuals are picked based on a user defined fitness function. The remaining individuals are discarded. Next, a number of individuals are selected and paired with each other. Each individual pair generates one offspring by partially exchanging their genes around one or more randomly selected crossing points. At the end, a certain number of individuals are selected and the mutation operations are applied (i.e. a randomly selected gene of an individual abruptly changes its value). The GA is called a population-based technique because instead of operating on a single potential solution, it uses a population of potential solutions.

The larger the population, the greater the diversity of the members of the population, and the larger the area searched by the population. Here, we have used Matlab optimization toolbox for implementation of GA. Based on the experimental results (see Fig. 5.8) the population size is set to 60 and the generation size is set to 150 for genetic optimization as a good compromise between accuracy and complexity.

## 5.5 Summary

This Chapter presents an autofocus method compatible with the SAR BP image formation algorithm. The proposed autofocus, which is a parametric-based method, utilizes genetic optimization algorithm with a new objective function to find an optimal flight trajectory. The objective function is obtained using PPs in different sub-apertures of SAR image. Thus, this autofocus method is well suited to BP image formation and its versatile imaging geometries. This autofocus method is advantageous because it requires no general assumptions of platform motion in order to operate. In addition, this new method can be used for both time and frequency domain algorithms. For frequency domain algorithm like RDA, the optimized flight trajectory can be used in the MC step.

The computational complexity of the proposed method is lower than the traditional parametric-based autofocus algorithm. This is because of two reasons: 1) it forms SAR image in limited range bins corresponding to PPs in each iteration of optimization algorithm instead of generating whole SAR image, and 2) it avoids RCMC step in RDA algorithm for image formation in the optimization loop because of modifying range-compressed data.

The proposed algorithm is especially important when a SAR is operated on a small aircraft or UAS, which are especially susceptible to the effects of atmospheric turbulence.

# Chapter 6. Experimental results

In this Chapter, first we will compare the proposed NLFM chirp signal with other well-known NLFM waveforms, which are designed based on spectrum shaping method. Then, the proposed NLFM waveform is investigated in SAR scenario, in which different signal processing algorithms for image formation from raw data are analyzed. Next, the simulations and comparisons related to the proposed MC algorithm in case of NLFM waveform for pulsed SAR system are presented. Finally, the proposed autofocus algorithm using real data from FMCW SAR system is examined and analyzed.

## 6.1 Comparison of the proposed NLFM with traditional waveforms

In this subsection, we will compare the proposed NLFM chirp signal with other well-known NLFM waveforms, which are designed based on spectrum shaping method [51-54]. Three different measures including SPLR, ISLR, and IRW are used to determine the performance of different waveforms. The simulation parameters are given in Table 6.1, and the simulation results of different waveforms are illustrated in Table 6.2.

It can be seen from the results that the proposed NLFM has a better compromise between SPLR, ISLR, and IRW indexes as compared to other alternative waveforms. In addition, different NLFM waveforms are investigated based on Doppler sensitivity. The performance of different waveforms versus Doppler shift

is depicted in Fig. 6.1. It can be observed from the results that the proposed NLFM waveform has better tolerance against Doppler shift for IRW measure; however for ISLR and SPLR indexes the behavior of different waveforms are almost similar as Doppler shifts.

Table 6.1: Key simulation parameters.

Parameter	Value
Pulse width ( $\mu\text{s}$ )	13
Bandwidth (MHz)	100
Sampling Frequency (MHz)	360

Table 6.2: Results of pulse compression of different NLFM waveforms.

Frequency Modulation	<b>SPLR<sub>dB</sub></b>	<b>ISLR<sub>dB</sub></b>	<b>IRW<sub>sample</sub></b>	
LFM	-	-13.38	-4.11	3.54
Cosine, $n = 1$ [51]	-	-22.98	-18.71	4.25
Cosine, $n = 2$	-	-29.78	-18.00	5.17
Tangent-based [52]	$\alpha = 5$	-32.27	-30.04	6.09
	$\alpha = 6$	-36.40	-33.76	6.71
Truncated Gaussian [53]	$k = 50$	-31.53	-13.47	5.12
	$k = 90$	-35.25	-13.78	6.73
Hybrid NLFM [54]	-	-38.41	-37.58	6.21
Proposed NLFM	$v = 1.25$	-38.34	-34.25	4.45
	$v = 1.35$	-47.36	-37.50	4.81
	$v = 1.60$	-59.01	-39.84	5.70

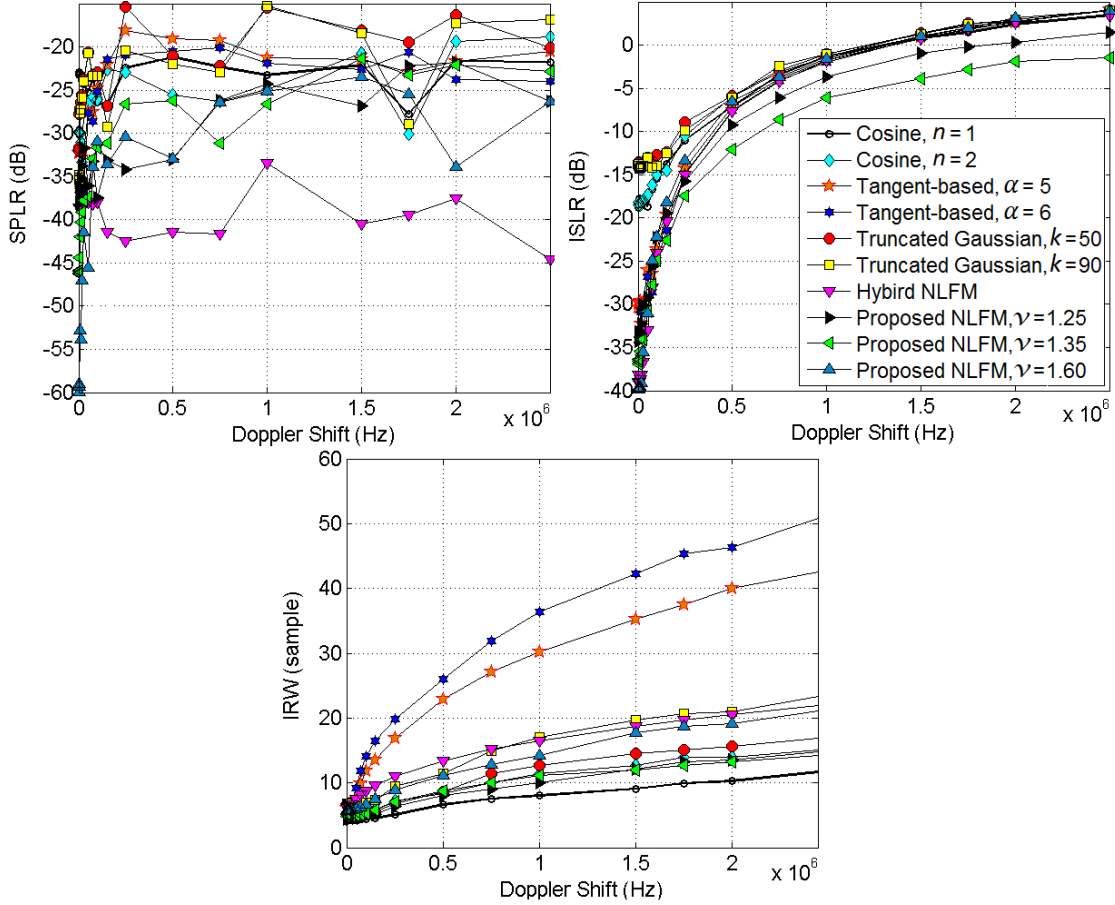


Figure 6.1: Doppler sensitivity results of different NLFM waveforms, left to right: SPLR, ISLR and IRW of pulse compression results versus Doppler shift.

## 6.2 The proposed NLFM waveform in SAR scenario

In order to validate the new offered chirp signal, strip-map SAR imaging geometry together with different reconstruction algorithms derived in Chapter 4 are considered. The synthetic examples are generated for both of point and distributed targets, and it is shown that NLFM chirp can improve imaging quality compared to the LFM chirp. The simulation parameters for SAR system are given in Table 6.3. The raw signal for point target is obtained using the model described in (4.38). To generate raw signal from real SAR image (which is digital complex-valued samples), SAR image should be resampled (or interpolated) based on the simulation parameters including the swath width, flight time, range and azimuth

resolutions. After resampling, each sample in the image should represent a resolution cell on the ground for SAR echo simulation. Then, delay time  $\tau$  should be obtained for each point target or image sample using the SAR imaging geometry, and the raw signal is obtained using the model described in (4.38). Finally, all of the raw signals for image samples are weighted summed with their corresponding amplitudes in the resampled SAR image.

After generating the SAR raw signal, RF noise is added to it (RF noise is simulated through filtering the Gaussian noise). It should be mentioned that because of randomness property of noise, RF noise is generated once, and it is used similarly for different experiments. The results of point target analysis are obtained for three different scenarios including LFM waveform, LFM + windowing, and NLFM waveform. Taylor window are typically used in radar applications, such as weighting SAR images and antenna design. Therefore, we have chosen the Taylor window for sidelobe reduction of MF response. The parameter of Taylor window is chosen to have an approximately same result compared to NLFM waveform in noise free condition.

Table 6.3: SAR system parameters for raw data simulation

Parameter	Value	Parameter	Value
Velocity (m/s)	60	Carrier frequency (GHz)	9
Bandwidth (MHz)	100	Sampling frequency (MHz)	220
Pulse width ( $\mu$ s)	35	Flight time (s)	8
Swath width (m)	700	Minimum Range (m)	4663
PRF (Hz)	300	Maximum Range (m)	5361
Altitude (m)	5000	Signal-to-noise ratio (dB)	-45
Incident Angle	45	Azimuth beamwidth (deg)	4

Four different measures including SPLR, ISLR, IRW, and 2-D ISLR are used to evaluate the performance of different algorithms in different scenarios. The 2-D ISLR is similar to the 1-D ISLR, with the main-lobe defined within a rectangle with the size of the respective IRWs in each direction multiply by a constant (10 or more). The sidelobe power is then the power of the entire 2-D image minus the main-lobe power [23].

The results of different algorithms for point target analysis are shown in Tables 6.4 and 6.5. It can be seen that time domain algorithms (Table 6.4) have better performances compared to the frequency domain methods (Table 6.5). The results for NLFM waveform in both time and frequency domain algorithms have shown improvements compared to the LFM waveform and LFM + windowing scenarios. Because of the mismatch condition between the transmitted and received waveform in LFM + windowing scenario, both the SNR and the resolution are weaker as compared to the NLFM waveform case. Sidelobe reduction results in main-lobe widening of MF response in LFM + windowing and NLFM waveform scenarios as compared to LFM waveform case. However, it is an essential stage in radar imaging to get image with high contrast. Therefore, it is advisable to use NLFM waveform for this purpose.

Table 6.4: Results of point target analysis, for the time domain signal processing algorithms.

<b>Method</b>		TDC (LFM)	TDC (LFM+ Windowing)	TDC (NLFM)	BP (LFM)	BP (LFM+ Windowing)	BP (NLFM)
<b>SPLR<sub>dB</sub></b>	Ground Range	-21.88	-28.39	-30.25	-15.90	-27.03	-29.81
	Azimuth	-29.61	-28.21	-33.54	-20.88	-21.63	-27.59
<b>ISLR<sub>dB</sub></b>	Ground Range	-10.95	-13.32	-13.31	-4.74	-9.35	-10.24
	Azimuth	-12.28	-12.54	-12.58	-6.10	-5.97	-9.27
<b>2D ISLR<sub>dB</sub></b>		-6.28	-5.63	-6.88	-4.95	-4.42	-5.86
<b>IRW<sub>sample</sub>*</b>	Ground Range	1.12	1.74	1.69	1.52	1.93	1.78
	Azimuth	0.73	0.74	0.73	0.74	0.73	0.72

\*Each sample in azimuth direction is equal to 0.25 m, and in ground range direction is 1.5 m.

Table 6.5: Results of point target analysis, for the frequency domain signal processing algorithms.

Method		RDA (LFM)	RDA (LFM+ Windowing)	RDA (NLFM)	$\omega$ -k (LFM)	$\omega$ -k (LFM+ Windowing)	$\omega$ -k (NLFM)
SPLR <sub>dB</sub>	Slant Range	-15.70	-28.99	-32.06	-16.20	-28.71	-29.55
	Azimuth	-23.22	-19.04	-22.46	-23.57	-23.72	-23.91
ISLR <sub>dB</sub>	Slant Range	-4.93	-9.04	-8.71	-5.54	-9.23	-9.67
	Azimuth	-12.50	-9.73	-13.35	-13.75	-13.54	-14.54
2D ISLR <sub>dB</sub>		-1.77	-1.24	-2.64	-2.09	-0.42	-2.697
IRW <sub>sample</sub> *	Slant Range	2.09	2.89	2.87	2.010	2.83	2.81
	Azimuth	1.13	1.13	1.13	1.11	1.11	1.11

\*Each sample in azimuth direction is equal to 0.22 m, and in slant range direction is 0.69 m.

For better clarification, reconstructed image contours of time and frequency domains algorithms in different scenarios for multiple point scatterers are shown in Figs. 6.2 and 6.3, respectively. It should be mentioned that the objective results shown in Tables 6.4 and 6.5 are related to the point target in the center. The reconstructed image contours are in dB scale. In a good reconstructed image, the point targets should be well separated. This needs an image with high SNR and low side-lobes levels. In the results, a contour image with darker (bluer) regions around the point targets has better SNR and lower side-lobes levels. It can be seen from the results that the improvement of using NLFM waveform is superior for TDC method compared to the BP algorithm. This is because the TDC algorithm is a very exact method without any approximation. As we have discussed in Section III, the BP algorithm uses start and stop approximation in order to range compress SAR data via MF.

It can also be seen from the results that the time domain algorithms have better performance compared to the frequency domain methods (this is because the approximations used in deriving the frequency domain algorithms, which is discussed in Chapter 4). It should be mentioned that the results for RDA and

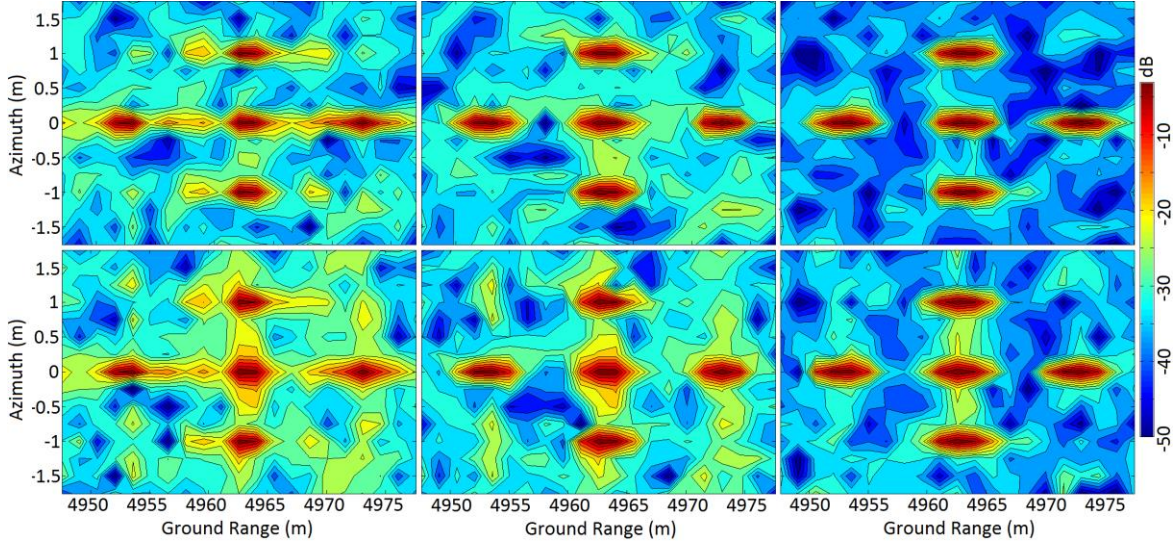


Figure 6.2: Comparison of different time domain algorithms in different scenarios. Top row, left to right: TDC results with LFM, LFM+windowing and NLFM, bottom row: BP algorithm results.

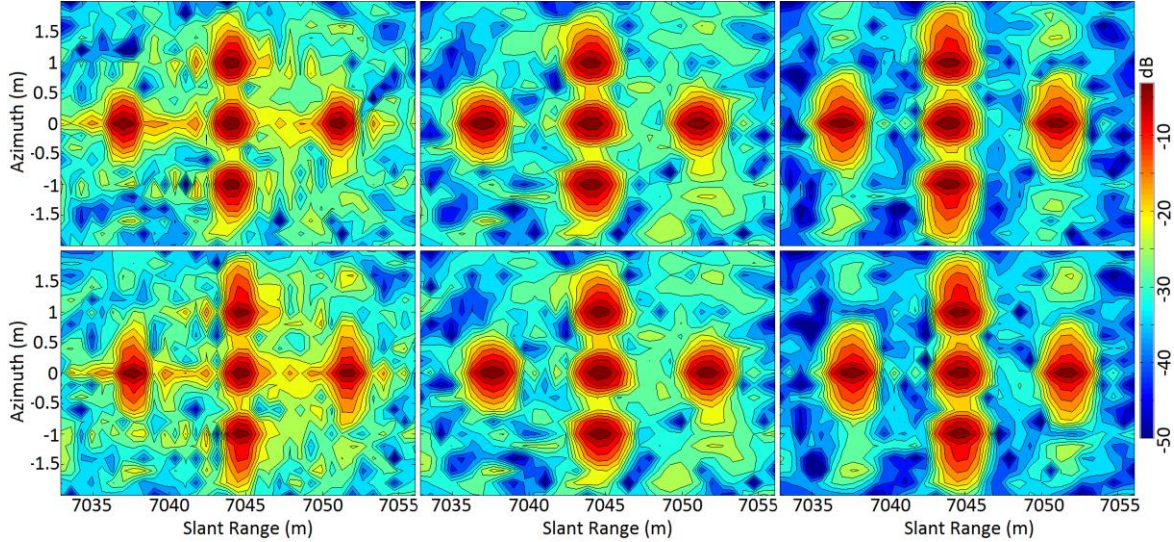


Figure 6.3: Comparison of different frequency domain algorithms in different scenarios. Top row, left to right: RDA results with LFM, LFM+windowing and NLFM, bottom row: omega-K algorithm results.

omega-K algorithms are obtained in the slant range-azimuth surface (to obtain the image in the ground-range azimuth surface, a 1-D interpolation should be used).

Another experiment has been performed in order to show the performances of the different NLFM waveforms in SAR scenario. Since the matching condition is provided between the transmitted and the received signals for NLFM waveforms,

there is no loss in SNR after matched filtering. Therefore, for better demonstration of the improvement using the proposed NLFM waveform, the simulation is performed in noise free condition. SAR system parameters shown in Table 6.3 are used for this simulation. It should be mentioned that the parameters of different NLFM waveforms are selected based on having approximately same resolution in range direction. Fig. 6.4 shows the point target response reconstructed using BP algorithm for different waveforms, which are used in the raw data simulation. It can be seen from the results that the proposed NLFM waveform has better sidelobe reduction with approximately the same resolution as compared to the traditional NLFM waveforms.

We have also performed an experiment to simulate raw signal based on NLFM chirp signal for distributed target. Fig. 6.5 shows a real SAR image which is used as input for raw signal simulation. SAR system parameters shown in Table 6.3 are

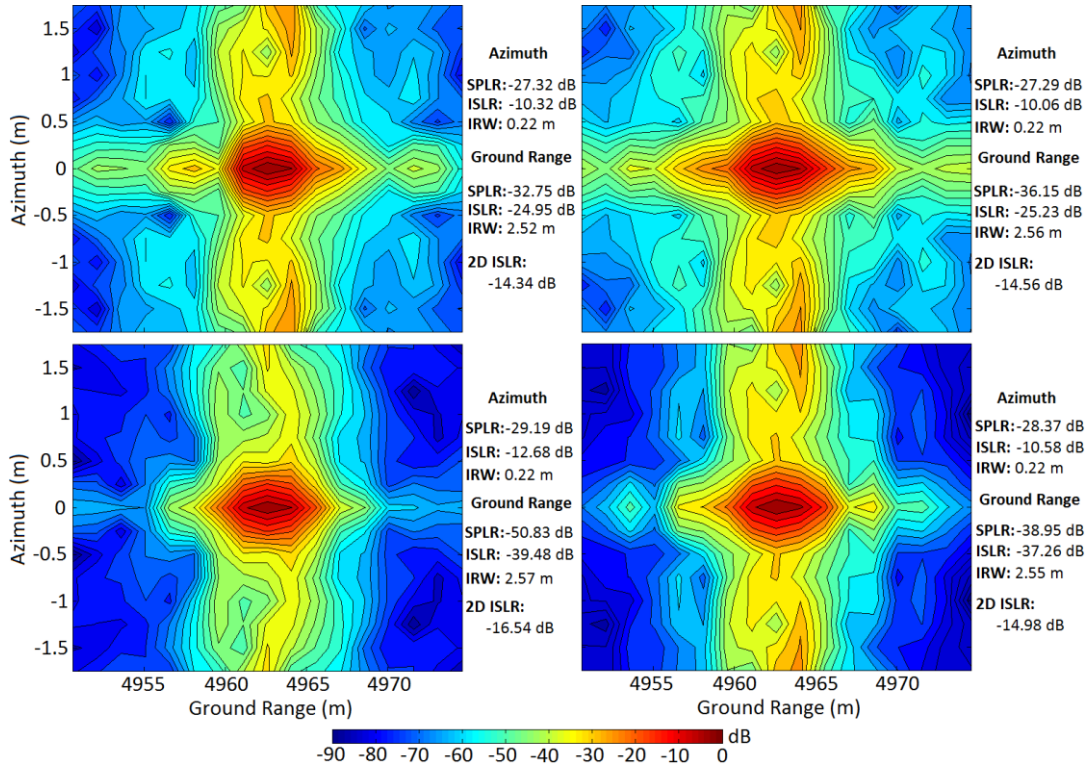


Figure 6.4: Comparison of different NLFM waveforms used in SAR scenario with point target. From top left, clockwise: Cosine,  $n = 1$  [12], Tangent-based [13], Hybrid NLFM [15], and the proposed NLFM.

used for this simulation. Reconstructed images using different signal processing algorithms derived for NLFM signal are shown in Fig. 6.6. From the results, it can be seen that the SNR and resolution are better for time domain algorithms as compared to the frequency domain algorithms.

### 6.3 The proposed MC algorithm in case of using NLFM waveform

In this subsection, the results of the proposed MC algorithm with navigation data in case of using NLFM waveform as transmitting signal are presented. For this experiment, a real flight GPS data is used to generate SAR raw signal for both point and distributed targets to validate the proposed MC algorithm for NLFM waveform. The nominal trajectory versus real trajectory used in the simulation is shown in Fig. 6.7. It should be mentioned that for better demonstration the improvement using the proposed MC algorithm, the simulations are performed in noise free condition.



Figure 6.5: A real SAR image used to simulate raw data (this SAR image shows an area of the sea near a busy port).

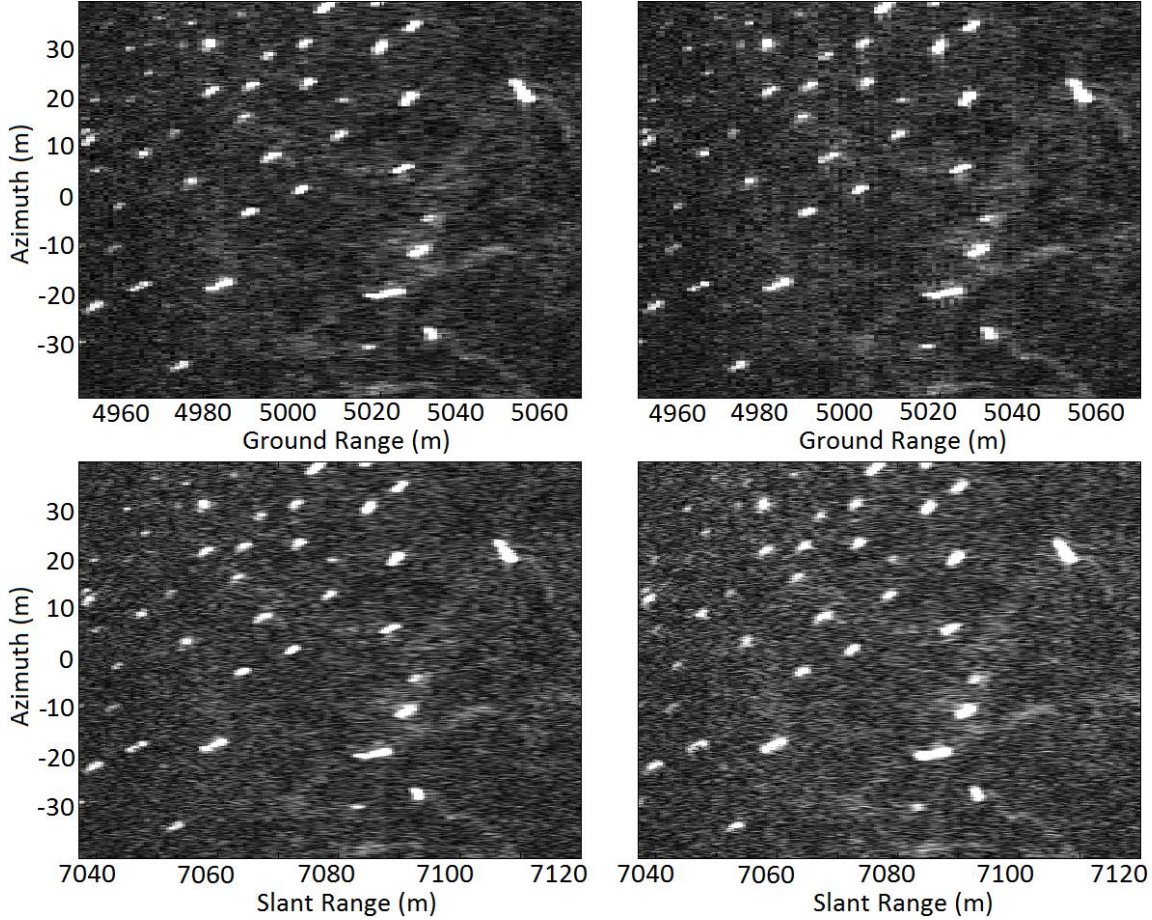


Figure 6.6: Results of distributed target analysis, from top left, clockwise: TDC, BP, RDA, and omega-K algorithms.

The results of traditional and proposed MC algorithms are shown in Figs. 6.8 and 6.9 for point and distributed targets, respectively. In addition, the objective results of point target analysis are shown in Table 6.6. For the point target analysis shown in Fig. 6.8, it can be visually observed that the proposed algorithm outperforms the traditional MC method in terms of resolution, side-lobes levels, and accuracy of target location. In addition, from the numerical results in Table 6.6, we can see that the azimuth resolution of point target obtained by the proposed method is 1.32 samples; however, the azimuth resolution is 2.42 samples for the traditional MC method. Therefore, the objective measures including SPLR, ISLR, and IRW should be considered all together for justification. For distributed target analysis shown in Fig. 6.9, there are improvements in terms of resolution and accuracy of target location for the proposed method.

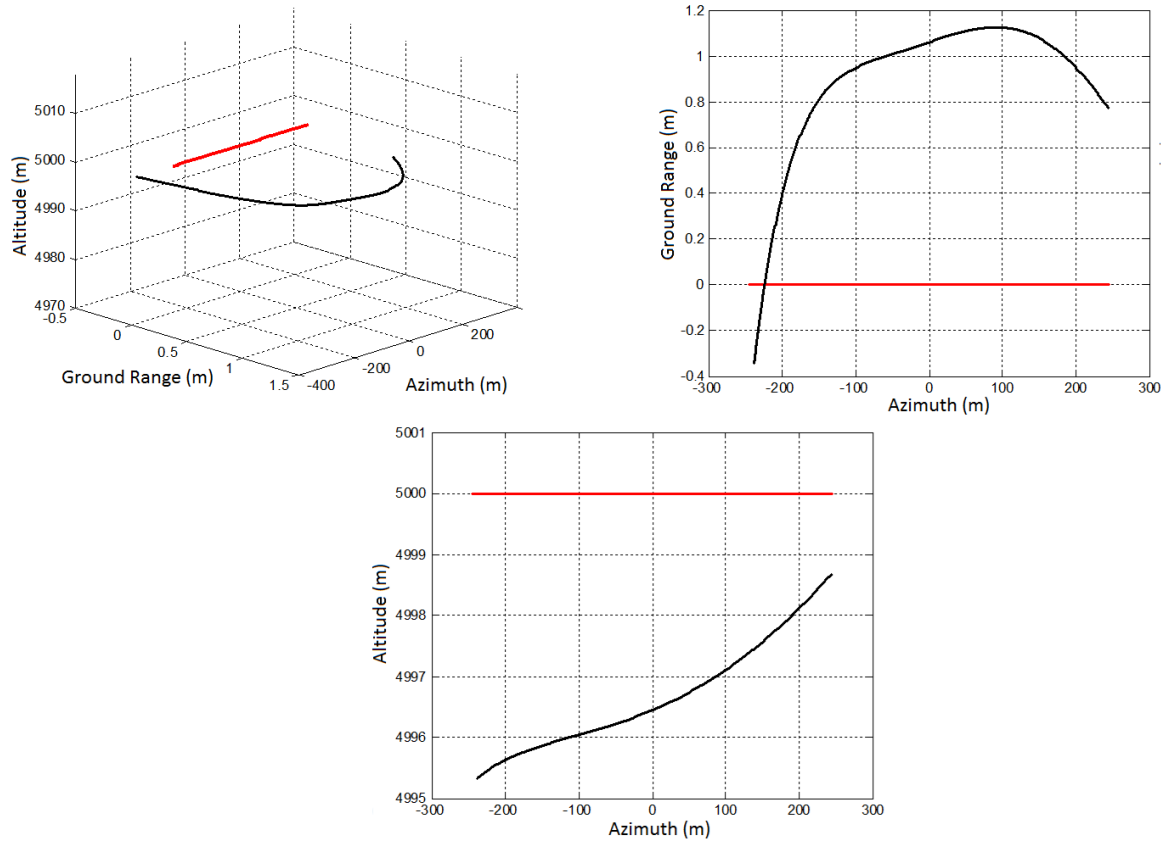


Figure 6.7: Nominal trajectory versus real trajectory used in simulation.

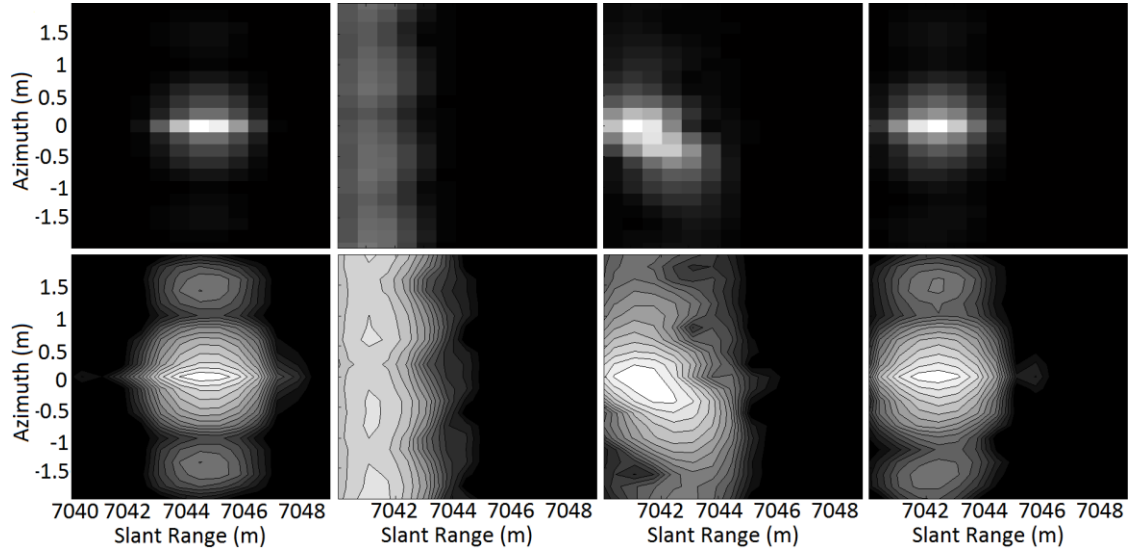


Figure 6.8: MC results. Top row, left to right: Amplitude image obtained in ideal case, without MC, traditional MC [24], and proposed MC. Bottom row: contour image of logarithmic scale for better visual comparison.

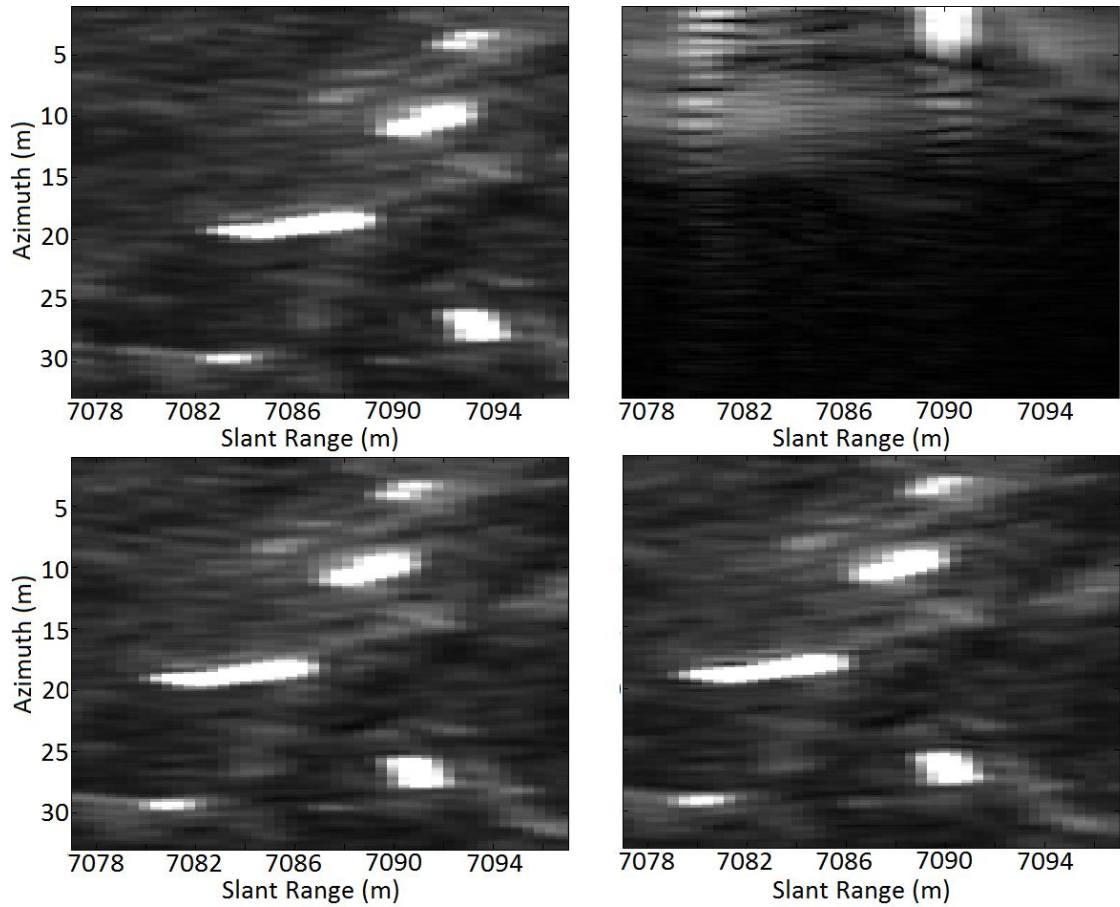


Figure 6.9: MC results. from top left, clockwise: Amplitude image obtained in ideal case, without MC, traditional MC [24], and proposed MC.

Table 6.6: Results of MC experiment for point target.

Method		Ideal Case	Traditional [24]	Proposed
SPLR <sub>dB</sub>	Slant Range	-41.136	-32.570	-35.127
	Azimuth	-23.726	-27.296	-23.766
ISLR <sub>dB</sub>	Slant Range	-28.370	-21.038	-21.722
	Azimuth	-14.888	-14.960	-14.435
2D ISLR <sub>dB</sub>		-19.699	-9.858	-9.879
IRW <sub>sample</sub> *	Slant Range	2.850	2.740	2.880
	Azimuth	1.090	2.420	1.390

\*Each sample in azimuth direction is 0.22 m, and in range direction is 0.69 m.

## 6.4 The proposed autofocus algorithm

In this subsection, we demonstrate results on real data from two different SAR systems. In the first experiment, the raw SAR data with an imaging resolution of  $1.5 \times 1$  m (range×azimuth) are collected by an experimental SAR, which was developed by the PARDIS electronic development company in Iran as shown in Fig. 6.10. A helicopter carried the SAR system. The experimental SAR system operated in C-band (5.20 GHz) with bandwidth 100 MHz. The helicopter flew at a height of about 200-1000 m, at a speed of 30–60 m/s. At C-band, two identical custom microstrip antennas, each consisting of a  $2 \times 8$  patch array, are used in a bi-static configuration. The antennas are constructed from two printed circuit boards sandwiched together, a symmetric feed structure on the back of one board and a microstrip patch array on the front of another, with pins feeding the signal through the boards. The antennas are approximately  $4'' \times 12''$  and have an azimuth 3dB beamwidth of 11 degree and an elevation 3dB beamwidth of 35 degree. The return signal is amplified and mixed with the transmit signal. This de-chirped signal is filtered and then sampled with a 16 bit A/D at 8.33 MHz. A custom FPGA board was designed to sample the signal and store the data on a pair of 32GB Compact Flash disks. The data is collected continuously at a rate of 133 Mb/second and stored on-board. After hardware pre-summing, the effective PRF is 500 Hz.

It was not equipped with highly accurate inertial navigation units and the navigation depended merely on a GPS system. The GPS provided motion information at the frequency of 10 Hz, and its positioning accuracy of GPS was 5 m. Owing to the limitation and inaccuracy of the motion information, navigation-based MC was insufficient for the generation of the high quality imagery. Therefore, we needed a highly precise raw-data-based autofocus. The images generated by the GPS-based MC and our autofocus approach are shown in Figs. 6.11 (b) and (c), respectively. The vertical direction is azimuth, and the horizontal direction is range. Apparently, it can be noted that the image generated by the GPS-based MC is seriously blurred and distorted in geometry due to the lack and

inaccuracy of motion measurements. While the image achieved by our autofocus approach is focused with a high quality. The area under observation is strongly diverse partly sea, coast, and town. By compensating the spatially variant phases, the SAR imagery could be achieved with high precision. The local scene, highlighted in Fig. 6.11 (c) by white rectangle, is amplified in Fig. 6.11 middle row. There are groups of corner reflectors array in the right corner of image. As clearly presented in the magnified image of Fig. 6.11 (c), the corner reflector arrays are focused in a good way. In addition, a point target has been selected to show the azimuth profile in different scenarios.



Figure 6.10: Left: Photograph of antennas mounted on a helicopter, and right: SAR system hardware.

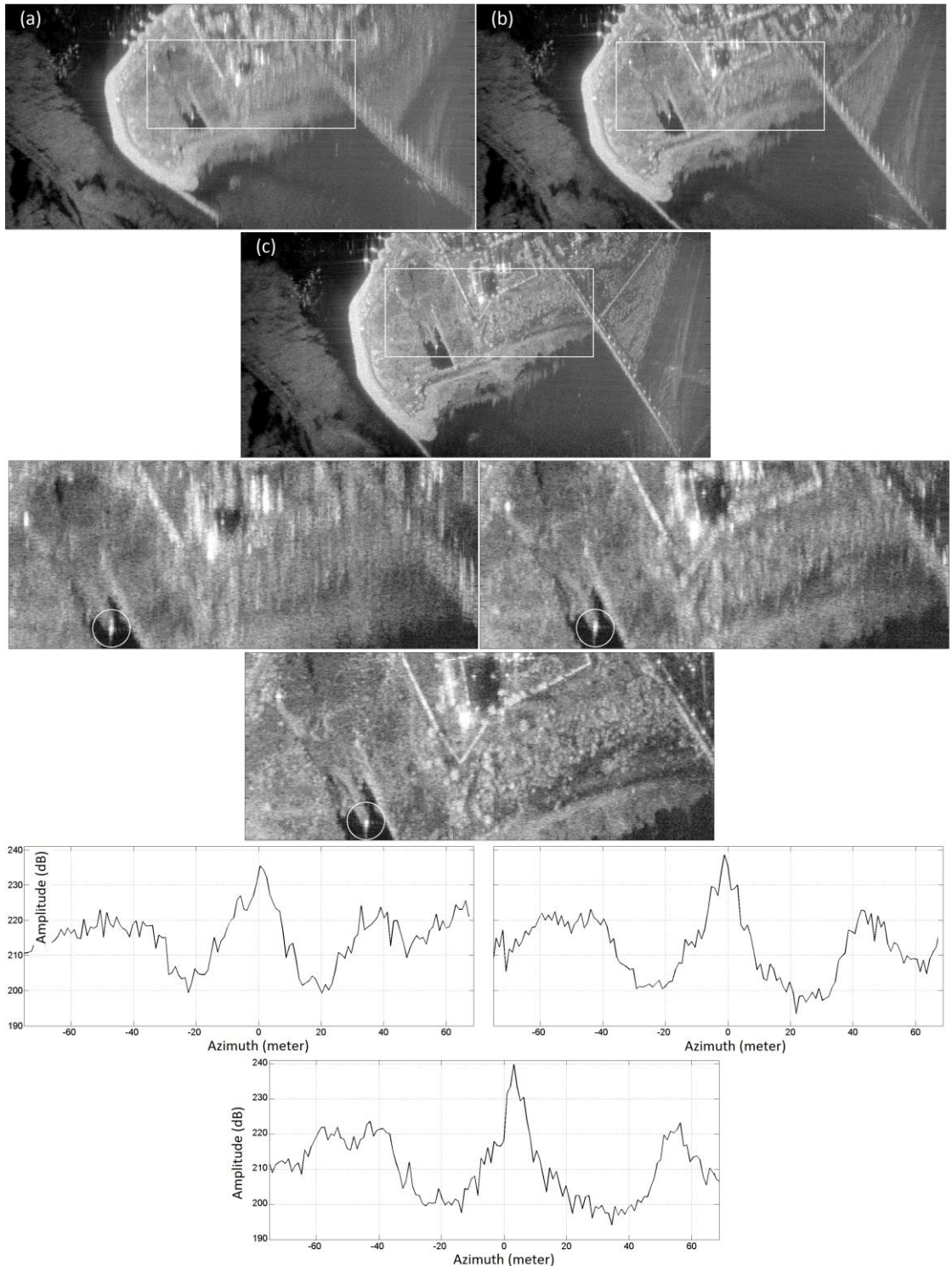


Figure 6.11: A sample SAR image (a) without MC, (b) MC with navigation data, and (c) the proposed autofocus. Middle row: Magnified images highlighted by white rectangles. Bottom row: Azimuth profiles of selected point targets highlighted by white circles.

The presented method also works well in areas with several PPs. An example of a focused SAR image, created using the BP algorithm plus the proposed autofocus technique, is shown in Fig. 6.12 (c). From Fig. 6.12 (c), one can see the towns, freeway, villages, and wild scenes clearly distinguished and well-focused. For better demonstration, we have put the azimuth profiles of selected point targets highlighted by white circles in Figs. 6.11 and 6.12 in different scenarios on a same graph in Fig. 6.13. It can be seen from the results that the target impulse response in azimuth direction becomes narrower with higher peak level for our autofocus approach. The presented algorithm was also tested at a homogenous area with smaller PPs (see Fig. 6.14).

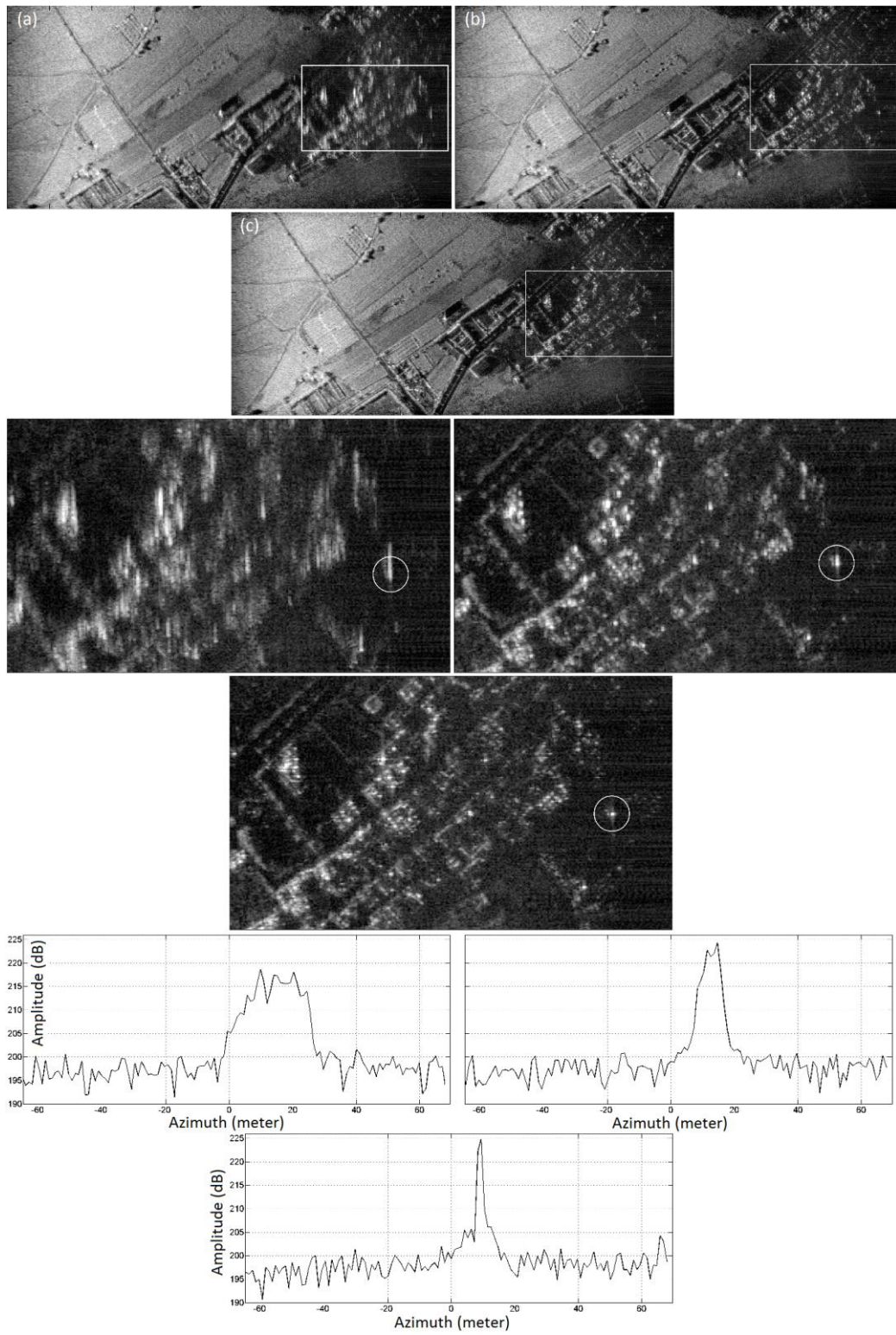


Figure 6.12: A sample SAR image (a) without MC, (b) MC with navigation data, and (c) the proposed autofocus. Middle row: Magnified images highlighted by white rectangles. Bottom row: Azimuth profiles of selected point targets highlighted by white circles.

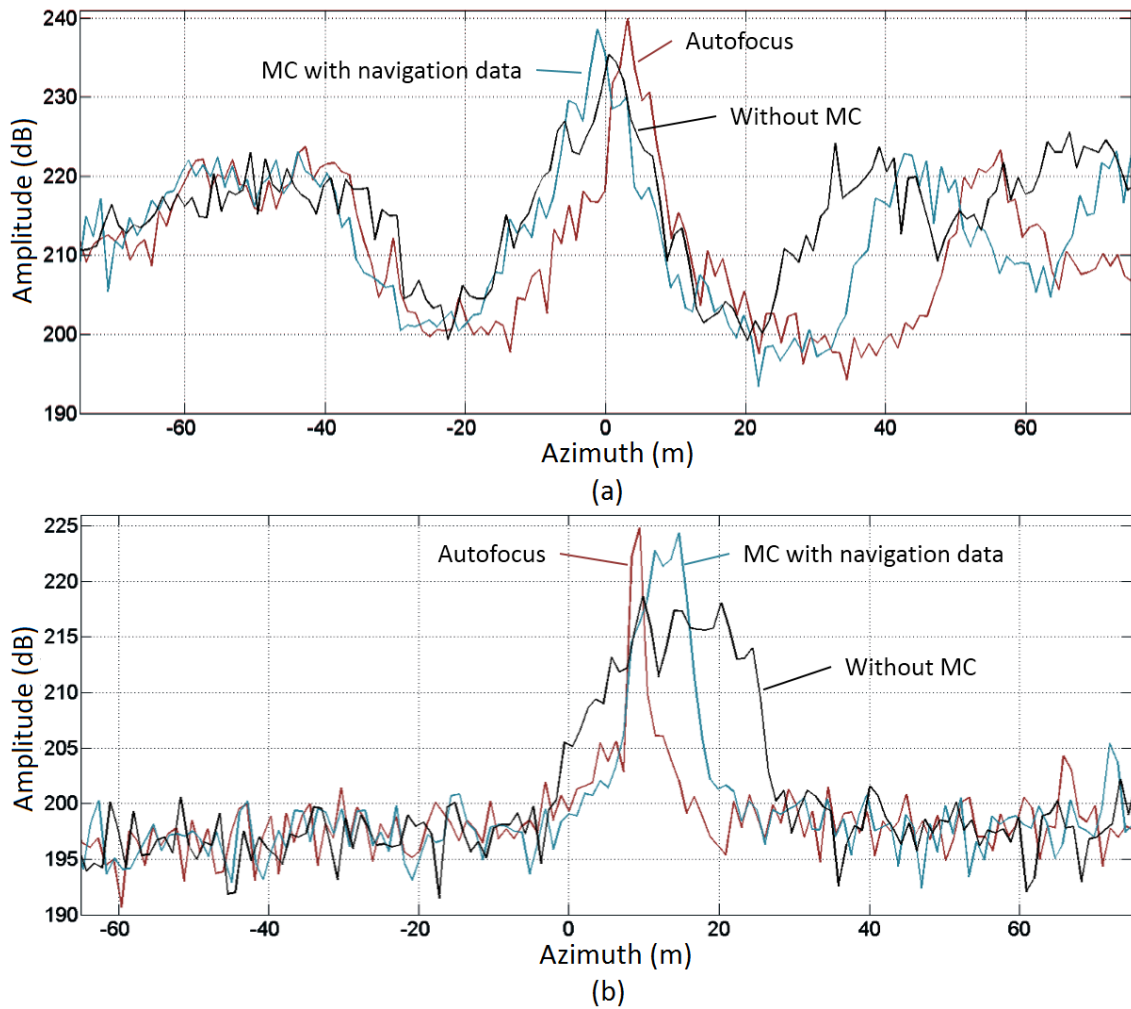


Figure 6.13: Azimuth profiles of selected point targets in different scenarios highlighted by white circles in (a) Figure 6.11, and (b) Figure 6.12.

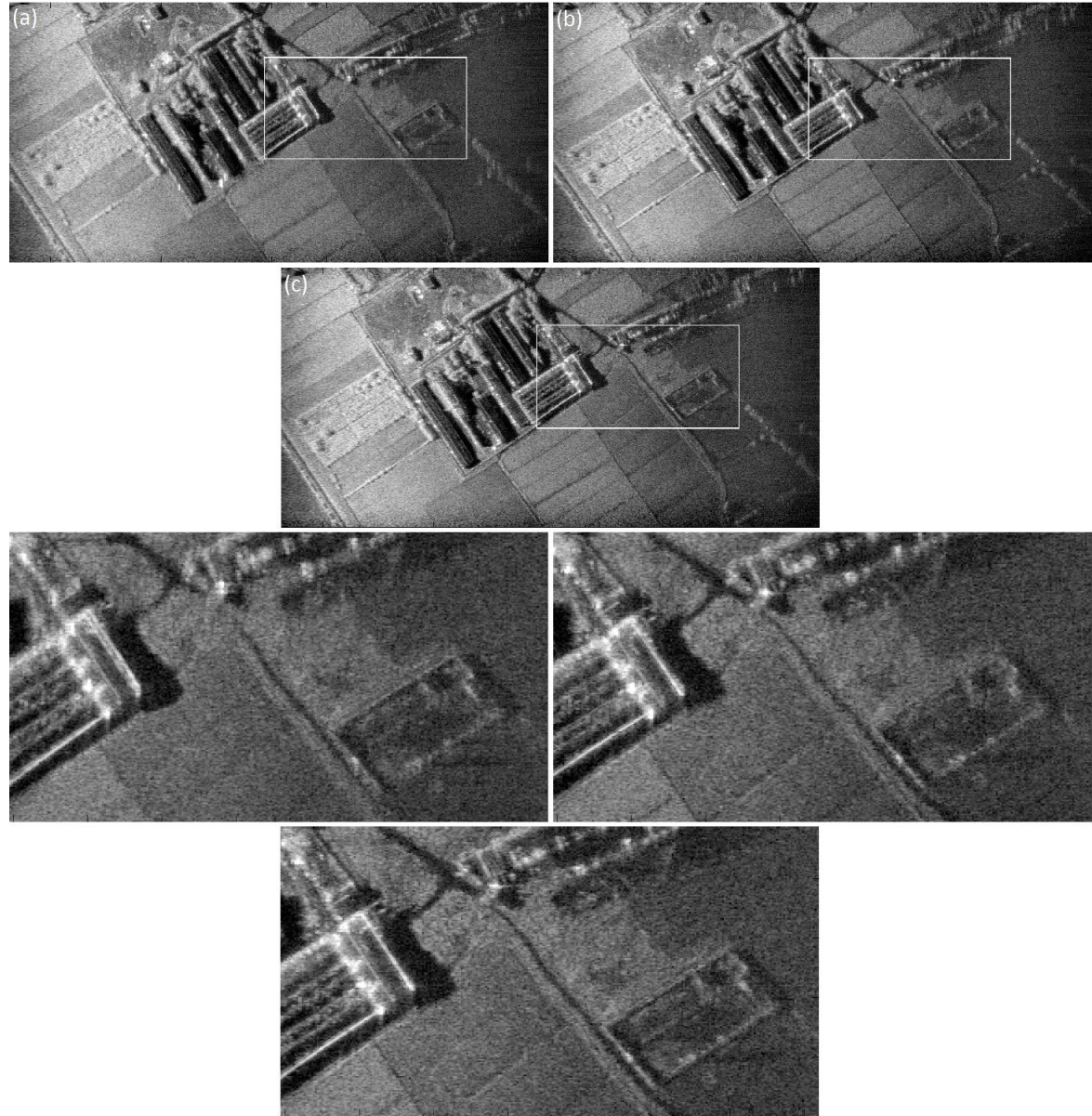


Figure 6.14: A sample SAR image (a) without MC, (b) MC with navigation data, and (c) the proposed autofocus. Bottom row: Magnified images highlighted by white rectangles.

In the following, we have presented the experimental results of the microASAR imagery of CASIE-09 dataset [21, 70]. It provides a resolution of  $1 \times 1$  m (range×azimuth). The microASAR is based on licensed BYU μSAR [10] technology as shown in Fig. 6.15. It is professionally built by ARTEMIS, Inc., making it a much more robust and flexible system [71]. The MicroASAR is a complete, self-contained SAR system that has been designed specifically to be

small and lightweight while still being robust and capable. These characteristics make it an ideal SAR system for use on UAS and other small aircraft. Rather than transmitting pulses, the MicroASAR is a continuous wave (CW) SAR system. A CW system is constantly transmitting and receiving and is thus capable of maintaining a high SNR while transmitting much less peak power than a comparable pulsed system. The microASAR transmits at 1 W and operates at altitudes 1000-3000 ft. It operates at C-band with a variable bandwidth up to 200 MHz. An analog de-chirp on receive reduces the sampling requirements to keep the data rate low. The system is pseudo-monostatic, i.e., it transmits and receives at the same time using two separate antennas that are placed closely together. This enables long transmit chips, which maximize the SNR while minimizing peak transmit power. The return signal is mixed down with a frequency-shifted copy of the transmit signal (this is known as analog dechirp), digitized, and processed with an all-digital IF stage. Raw data is stored into a compact flash (CF) disk along with GPS timing and position data. Using 32 GB CF disks, over two hours of SAR data can be recorded.

In July 2009, a BYU/Artemis microASAR system was flown as part of the Characterization of Arctic Sea Ice Experiment 2009 (CASIE-09). An extensive data set of high resolution C-band SAR data was collected over sea ice by the microASAR from the NASA Sierra UAS 500 miles northwest of Svalbard Island in the Arctic Ocean. For the CASIE experiment, the microASAR transmit bandwidth is set to 170 MHz, yielding a maximum ideal range resolution of approximately 90 cm, though the effective resolution is reduced in processing. The transmit center frequency is 5.42876 GHz. After hardware pre-summing, the effective PRF is 307.292 Hz. A short sample of the raw microASAR data is being made available as a public service, which is used here for second experiment.

The SAR image has been obtained by using the recorded motion parameters from the navigation system, as shown in Fig. 6.16 (b). In Fig. 6.16 (c), the image generated by applying the proposed autofocus approach, is presented. The horizontal direction is range, and the vertical direction is azimuth. In comparison,

the magnified images of the scene highlighted by white rectangles are shown in Fig. 6.16 bottom row. Obviously, the image generated by the MC is blurred and distorted due to the inaccuracy of motion recording. However, the image generated by the proposed autofocus is well-focused. This experiment validates our method for another scenario of UAS SAR imagery, which is used for sea ice observation purpose.

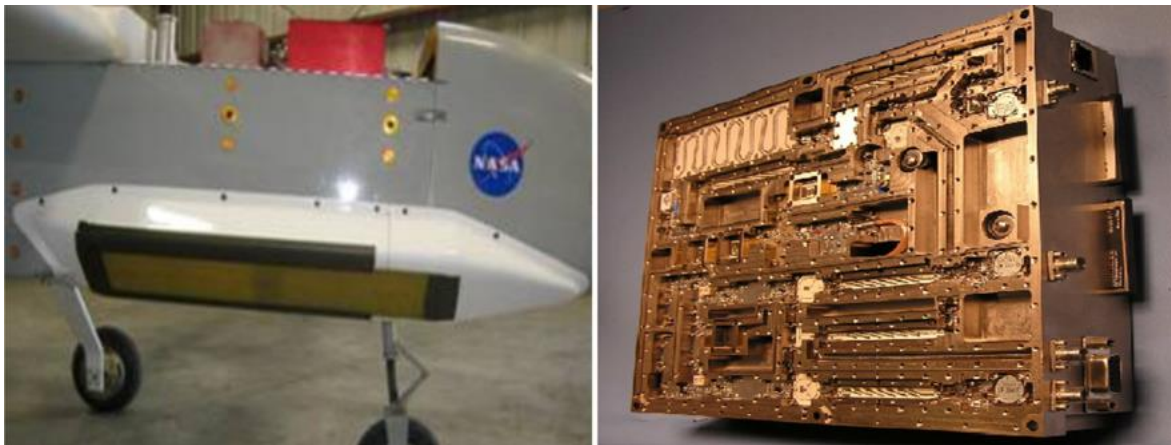


Figure 6.15: Left: Photograph of a microASAR system mounted on a small UAS, and right: SAR system hardware.

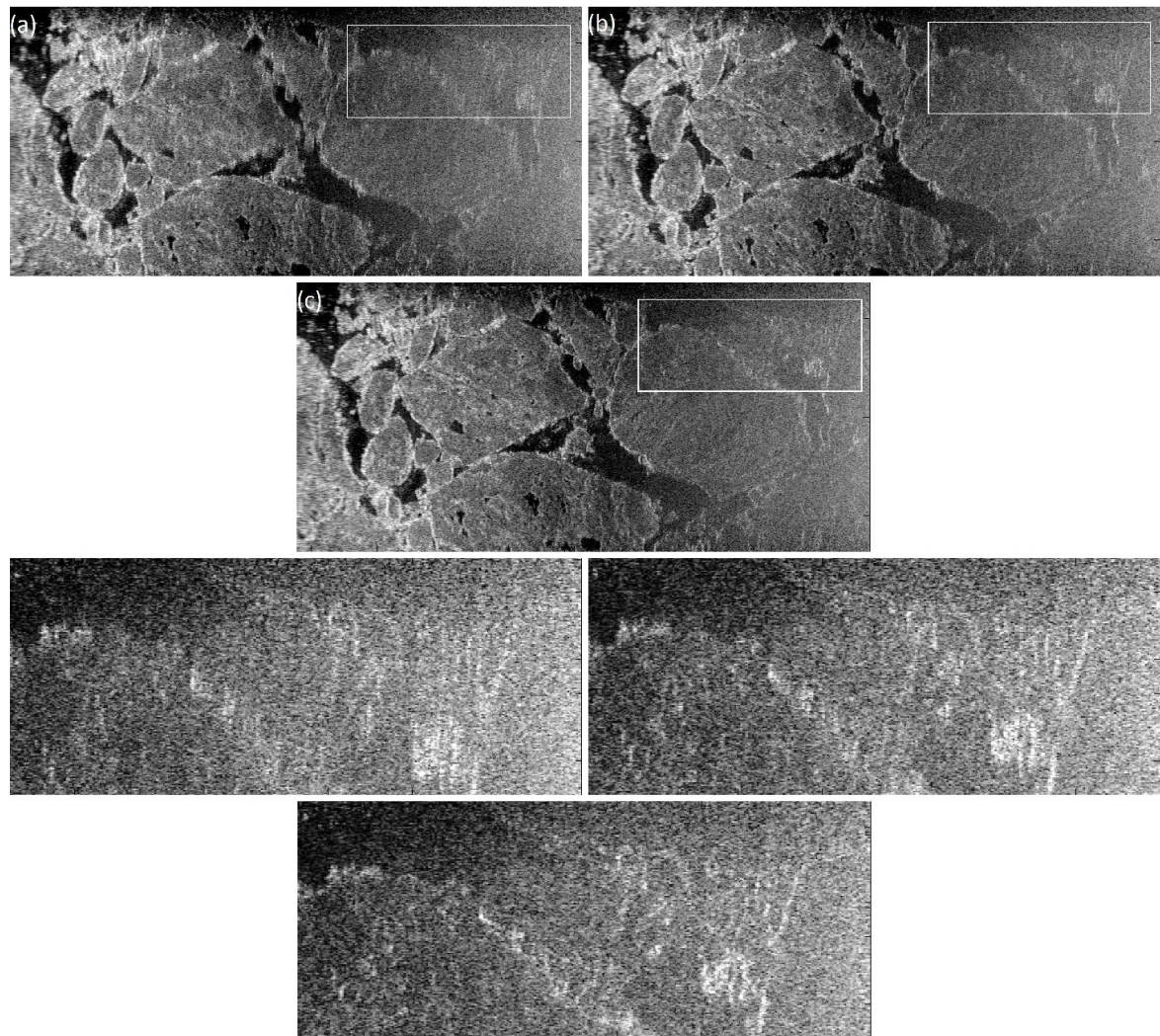


Figure 6.16: A sample SAR image (a) without MC, (b) MC with navigation data, and (c) the proposed autofocus. Bottom row: Magnified images highlighted by white rectangles.

## Chapter 7. Conclusions and future works

In this dissertation, two research topics has been investigated. In the first research, both linear and non-linear frequency modulation have been examined. Traditional NLFM waveforms are reviewed and the instantaneous phase and frequency functions are derived for them. Then, a new NLFM waveform is proposed, which can be used as a transmitted chirp in SAR imaging to improve the imaging quality compared to LFM chirp signal. Time domain signal processing algorithms (TDC and BP) and frequency domain methods (RDA and omega-k) are modified in order to use NLFM waveform as the transmitted chirp for SAR imaging. In addition, a modified motion compensation algorithm is developed for phase error compensation in NLFM waveform case, which is used as transmitting waveform in SAR system. This algorithm has been developed for using with RDA method.

Experimental results demonstrate effectiveness of the proposed NLFM waveform, in which for similar IRW, the proposed NLFM has better PSLR and ISLR indexes as compared to the traditional NLFM waveform. In fact, the proposed NLFM has a better compromise between SPLR, ISLR, and IRW indexes as compared to other alternative waveforms. In addition, the proposed NLFM along with the traditional NLFM waveform have been compared by their Doppler sensitivity. It can be observed from the results that the proposed NLFM waveform has better tolerance against Doppler shift for IRW measure; however for ISLR and SPLR indexes the behavior of different waveforms are almost similar as Doppler shifts. The results of using the proposed NLFM waveform in SAR scenario show

the improved SNR and side-lobe levels compared with LFM waveform and other traditional NLFM waveforms.

In the second research subject, an autofocus method compatible with the SAR BP image formation algorithm is presented. The proposed autofocus, which is a parametric-based method, utilizes genetic optimization algorithm with a new objective function to find an optimal flight trajectory. The objective function is obtained using PPs in different sub-apertures of SAR image. Thus, this autofocus method is well suited to BP image formation and its versatile imaging geometries. This autofocus method is advantageous because it requires no general assumptions of platform motion in order to operate. In addition, this new method can be used for both time and frequency domain algorithms. For frequency domain algorithm like RDA, the optimized flight trajectory can be used in the MC step.

The computational complexity of the proposed method is lower than the traditional parametric-based autofocus algorithm. This is because of two reasons: 1) it forms SAR image in limited range bins corresponding to PPs in each iteration of optimization algorithm instead of generating whole SAR image, and 2) it avoids RCMC step in RDA algorithm for image formation in the optimization loop because of modifying range-compressed data. The proposed algorithm is especially important when a SAR is operated on a small aircraft or UAS, which are especially susceptible to the effects of atmospheric turbulence. Real data from two different SAR systems in LFM-CW mode are also used for experimental results. The results on real LFM-CW SAR data show the validity of the proposed autofocus approach for BP algorithm. Especially, the impulse response of point targets in the images obtained with the proposed method are generated by smaller main-lobe width and lower side-lobe levels than the conventional motion compensation algorithm with navigation data.

During this study, we were able to acquire special achievements in relation to the subject of synthetic aperture radar signal processing. These achievements are summarized in this section:

- ❖ Conceptual and system design of SAR in different functional modes consisting of pulsed and CW modes is accomplished and localized manufacturing capability of synthetic aperture radar has been created in the country.
- ❖ Raw signal simulation based on points and the distributed targets for different operating modes is performed. Since the SAR raw signal simulation for the distributed targets has high computational cost, ability to use special hardware such as GPU for implementation as parallel processing has been created.
- ❖ A new NLFM waveform based on piecewise linear functions has been proposed for improving the MF response in SAR imaging.
- ❖ Different signal prospecting algorithms including time domain correlation, back-projection, omega-k, and range-Doppler algorithm are investigated in order to use NLFM as the transmitted chirp in SAR system.
- ❖ A modified motion compensation algorithm using navigation data is proposed for phase error compensation due to translational motion of SAR platform.
- ❖ Lastly, a new autofocus algorithm is presented for BP image formation for remaining phase error compensation in SAR signal.

The following conference and journal papers are published throughout of this research:

1. J. Saeedi, K. Faez, “Non-linear Frequency Modulation Using Piecewise Linear Functions for Synthetic Aperture Radar Imaging,” *10th European Conference on Synthetic Aperture Radar*, Berlin, Germany, pp. 1-4, 2014
2. J. Saeedi, K. Faez, “A back-projection autofocus algorithm based on flight trajectory optimization for synthetic aperture radar imaging,” *Multidimensional Systems and Signal Processing*, pp. 1-21, December 2014.
3. J. Saeedi, K. Faez, “Synthetic Aperture Radar Signal Processing Using Nonlinear Frequency Modulation Chirp signal,” *IEEE transactions on aerospace and electronic Systems*, 52 (1), pp. 1-12, February 2016.

The work of this dissertation can be applied and extended to a variety of research topics. A few examples are enumerated below:

- ❖ Imaging techniques using SAR system in complex geometrical conditions, such as ballistic missile platform for targeting purposes, and extract appropriate processing algorithms for image formation is one of the proper research area. In addition, SAR system design considerations to determine the appropriate parameters of SAR system for properly functioning in the mentioned geometry conditions is also suitable for research.
- ❖ Another suggested research area can be imaging and detecting ground-moving targets using SAR system. Typically, for detecting moving targets in SAR image, two separate receivers are used. Using a single receiver to image and detect moving targets on the ground is a very interesting and exciting research project.
- ❖ In some of the military applications of SAR, the user encounters what is referred to as electronic warfare (EW). In these scenarios, the enemy utilizes a transmitting radar to send out a signal within the band of the SAR system transmitter to confuse the SAR system receiver; this is called an ECM to jam the SAR system. The ECM jamming signal causes the SAR system to receive and process erroneous information, which results in severe degradations in the output SAR images and/or formation of the image of nonexistent (phony) targets. Jamming and deception of radar systems are relevant for many military situations, platforms, and scenarios. Some situations are:
  - As countermeasure against wide area surveillance radar by deceiving SAR sensors.
  - To prevent situational awareness by introducing false information or hiding true information

Both the SAR ECM and ECCM are old but still hot topics nowadays. Therefore, provide solutions for jamming SAR systems can be considered as one of the important task ahead.

- ❖ The proposed MC algorithm using navigation data developed in this dissertation can be applied with RDA method. The omega-K algorithm has lower approximation towards the RDA method, and therefore results in better SAR imagery. However, it has some deficiencies in performing high precision motion compensation over the entire swath. Therefore, developing the motion compensation techniques for both LFM-CW SAR and pulsed SAR to be applied for the omega-K algorithm can be improved the performance of the motion compensation.

## References

- [1] Sandia. “What is Synthetic Aperture Radar,” *Internet Source*, February 2006. Sandia URL <http://www.sandia.gov/RADAR/whatis.html>.
- [2] I. Cumming, Y. Neo, and F. Wong, “Interpretations of the Omega-K algorithm and comparisons with other algorithms,” *Proceedings of the IEEE International Geoscience and Remote Sensing Symposium*, vol. 3, pp. 1455–1458, July 2003.
- [3] W. G. Carrara, R. S. Goodman, and R. M. Majewski, *Spotlight Synthetic Aperture Radar: Signal Processing Algorithms*. Artech House, 1995.
- [4] M. Soumekh. Synthetic Aperture Radar Signal Processing. John Wiley & Sons, Inc., New York, NY, second edition, 1999.
- [5] M. Blom, and P. Follo, “VHF SAR image formation implemented on a GPU,” in Proceedings of the IEEE International Geoscience and Remote Sensing Symposium, vol. 5, pp. 3352–3356, July 2005
- [6] E. C. Zaugg, “Generalized Image Formation for Pulsed and LFM-CW Synthetic Aperture Radar,” *Ph.D. thesis*, Department of Electrical and Computer Engineering, Brigham Young University, 2010.
- [7] A. Meta, J. deWit, and P. Hoogeboom, “Development of a high resolution airborne millimeter wave FM-CW SAR,” *In Proceedings of the First European Radar Conference*, pp. 209–212, 2004.
- [8] M. Edrich, “Design overview and flight test results of the miniaturised SAR sensorMISAR,” *In Proceedings of the First European Radar Conference*, pp. 205–208, 2004.
- [9] A. Meta, P. Hakkaart, F. Zwan, P. Hoogeboom, and L. Ligthart, “First demonstration of an X-band airborne FMCW SAR,” *In Proceedings of the 6th*

- European Conference on Synthetic Aperture Radar*, 2006.
- [10] E. Zaugg, D. Hudson, and D. Long, “The BYU uSAR: A small, student-built SARfor UAV operation,” *In Proceedings of the IEEE International Geoscience and Remote Sensing Symposium*, pp. 411–414, 2006.
- [11] J. T. Gonzalez-Partida, P. Almorox-Gonzalez, M. Burgos-Garcia, and B. P. Dorta-Naranjo, “SAR system for UAV operation with motion error compensation beyond the resolution cell,” *Sensors*, 8 (5), pp. 3384–3405, 2008.
- [12] M. Edwards, D. Madsen, C. Stringham, A. Margulis, B. Wicks, and D. Long, “microASAR:A small, robust LFM-CW SAR for operation on UAVs and small aircraft,” *In Proceedings of the IEEE International Geoscience and Remote Sensing Symposium*, vol. 5, pp. 514–517, 2008.
- [13] W. Wang, Q. Peng, and J. Cai, “Waveform-diversity-based millimeterwave UAV SAR remote sensing,” *IEEE Trans. Geosci. Remote Sens.*, 47 (3) , pp. 691–700, 2009.
- [14] M. I. Skolnik, *Introduction to Radar Systems*. McGraw-Hill, New York, 2001.
- [15] C. A. Wiley, “Synthetic Aperture Radars: A Paradigm for Technology Evolution,” *IEEE Transactions on Aerospace and Electronic Systems*, AES-21 (3), pp 440-443, May 1985
- [16] J. W. Goodman. *Introduction to Fourier Optics*. McGraw-Hill, New York, 1968.
- [17] D. A. Ausherman, “Digital Versus Optical Techniques in Synthetic Aperture Radar Data Processing,” *In Application of Digital Image Processing* (IOCC 1977), Vol. 119, pp. 238-256. SPIE, 1977.
- [18] J. R. Bennett, I. G. Cumming, R. A. Deane, P. Widmer, R. Fielding, and P. McConnell. SEASAT Imagery Shows St. Lawrence. *Aviation Week and Space Technology*, page 19 and front cover, February 26, 1979.
- [19] C. G. Gilmore, “A Comparison of Imaging Methods using GPR for Landmine Detection and A Preliminary Investigation into the SEM for Identification of Buried

Objects,” Master thesis, University of Manitoba Winnipeg, Manitoba, Canada December 2004

- [20] G. Franceschetti, and R. Lanari, *Synthetic Aperture Radar Processing*. CRC Press, 1999. 12, 122.
- [21] M. Edwards, D. Madsen, C. Stringham, A. Margulis, B. Wicks, and D. Long, “microASAR: A small, robust LFM-CW SAR for operation on UAVs and small aircraft,” in *Proceedings of the IEEE International Geoscience and Remote Sensing Symposium*, vol. 5, pp. V–514–V–517, July 2008
- [22] M. C. Edwards, E. C. Zaugg, D. G. Long, R. Christiansen, and A. Margulis, “A small, manned aircraft as a test bed for radar sensor development,” K. I. Ranney and A. W. Doerry, Eds., vol. 7308, no. 1. SPIE, 2009
- [23] I. G. Cumming and F. H. Wong, *Digital Processing of Synthetic Aperture Radar Data*. Artech House, 2005
- [24] G. Fornaro, “Trajectory deviations in airborne SAR: Analysis and compensation,” *IEEE Trans. Aerosp. Electron. Syst.*, 35 (3), pp. 997–1009, Jul. 1999.
- [25] A. Moreira and H. Yonghong, “Airborne SAR processing of highly squinted data using a chirp scaling approach with integrated motion compensation,” *IEEE Trans. Geosci. Remote Sens.*, 32 (5), pp. 1029–1040, Sep. 1994.
- [26] T. S. Lim, V. C. Koo, H. T. Ewe, and H. T. Chuah, “High frequency phase error reduction in SAR using particle swarm optimization,” *J. of Electromagn. Waves and Appl.*, 21 (6), pp. 795–810, 2007.
- [27] C. E. Mancill, and J. M. Swiger, “A mapdrift autofocus technique for correcting higher order SAR phase errors,” *27th Annual Tri-Service Radar Symposium Record*, pp. 391–400, Monterey, CA, 1981.
- [28] C. V. Jakowatz, and D. E. Wahl, “Eigenvector method for maximum-likelihood estimation of phase errors in synthetic aperture radar imagery,” *Optics Letters*, 10 (12),

- pp. 2539–2546, 1993.
- [29] D. E. Wahl, , P. H. Eichel, D. C. Ghiglia, and C. V. Jakowatz, “Phase gradient autofocus — A robust tool for high resolution SAR phase correction,” *IEEE Transactions on Aerospace and Electronic System*, 30 (3), pp. 827–835, 1994.
- [30] S. Yan, Y. Li, Z. Zhou, “Real-time motion compensation of an airborne UWB SAR,” *Proceedings of the 8th European Radar Conference Manchester*, pp. 305-308, UK 2011
- [31] E. Zaugg, and D. Long, “Theory and application of motion compensation for LFM-CW SAR,” *IEEE Transactions on Geoscience and Remote Sensing*, 46 (10), pp. 2990–2998, Oct. 2008.
- [32] O. Frey, C. Magnard, M. Rüegg, and E. Meier, “Focusing of Airborne Synthetic Aperture Radar Data From Highly Nonlinear Flight Tracks,” *IEEE transactions on geoscience and remote sensing*, 47 (6), JUNE 2009.
- [33] T. S. Lim, V. C. Koo, H. T. Ewe, and H. T. Chuah, “A SAR AUTOFOCUS ALGORITHM BASED ONPARTICLE SWARM OPTIMIZATION,” *Progress In Electromagnetics Research B*, 1, pp. 159–176, 2008
- [34] L. Zhang, Z. Qiao, M.Xing, L.Yang, and Z. Bao, “A Robust Motion Compensation Approach for UAV SAR Imagery,” *IEEE transactions on geoscience and remote sensing*, 50 (8), pp. 3202-3218, 2011
- [35] M. I. Skolnik, *Radar Handbook 3<sup>rd</sup> ed*, McGraw-Hill, New York, 2008.
- [36] M. H. Ackroyd, and F. Ghani, “Optimum mismatched filters for sidelobe suppression,” *IEEE Trans. on Aerospace and Electronic Systems*, AES-9, pp. 214-218. 1973.
- [37] S. R. DeGraaf, “Sidelobe Reduction via Adaptive FIR Filtering in SAR Imagery,” *IEEE trans. on image processing*, 3 (3), pp. 292-301, 1994.
- [38] 28Gbps Serial Transceiver Technology White Paper, XILINKS WP385 (v1.1),

2010.

- [39] W. Doerry, “Generating Nonlinear FM Chirp Waveforms for Radar,” *Sandia Report SAND2006-5856*, Unlimited Release, 2006.
- [40] E. Fowle, “The design of FM pulse compression signals,” *IEEE Transactions on Information Theory*, 10 (1), pp. 61–67, 1964.
- [41] M. Zych, “Suppression of GPR range sidelobes based on NLFM signal,” *19th International Radar Symposium*, Warsaw, Poland, pp. 454-458, 2012.
- [42] W. Doerry, “SAR Processing with Non-Linear FM Chirp Waveforms,” *Sandia Report SAND2006-7729*, Unlimited Release, 2006.
- [43] R. Wang, O. Loffeld, H. Nies, S. Knedlik , M. Hägelen, and H. Essen, “Focus FMCW SAR Data Using the Wavenumber Domain Algorithm,” *IEEE Trans. on Geoscience and Remote Sensing*, 48 (4), pp. 2109-2118, 2010
- [44] C. Bayindir, “ENHANCEMENTS TO SYNTHETIC APERTURE RADAR CHIRP WAVEFORMS AND NON-COHERENT SAR CHANGE DETECTION FOLLOWING LARGE SCALE DISASTERS,” *Ph.D. thesis*, School of Electrical and Computer Engineering, Georgia Institute of Technology, 2013
- [45] Y. K. Chan, M. Y. Chua, and V. C. Koo, “SIDELOBES REDUCTION USING SIMPLE TWO AND TRI-STAGES NON LINEAR FREQUENCY MODULATION (NLFM),” *Progress In Electromagnetics Research*, PIER 98, pp. 33-52, 2009.
- [46] H. Hellsten, P. Dammert and A. Ahlander, “Autofocus in Fast Factorized Backprojection for Processing of SAR Images when Geometry Parameters Are Unknown,” *IEEE Radar Conference*, pp. 603-608, 2010.
- [47] M. Liu, Ch. Li, and X. Shi, “A Back-Projection Fast Autofocus Algorithm Based on Minimum Entropy for SAR Imaging,” *3rd International Asia-Pacific Conference on Synthetic Aperture Radar*, pp. 1-4, 2011.
- [48] J. N. Ash, “An Autofocus Method for Backprojection Imagery in Synthetic

- Aperture Radar," IEEE geoscience and remote sensing letters, 9 (1), pp. 104-108, 2012.
- [49] J. Saeedi, K. Faez, "Non-linear Frequency Modulation Using Piecewise Linear Functions for Synthetic Aperture Radar Imaging," *10th European Conference on Synthetic Aperture Radar*, Berlin, Germany, pp. 1-4, 2014
- [50] J. Saeedi, K. Faez, "Synthetic Aperture Radar Signal Processing Using Nonlinear Frequency Modulation Chirp signal," *IEEE transactions on aerospace and electronic Systems*, 52 (1), pp. 99-110, February 2016.
- [51] E. Cook, "A Class of Nonlinear FM Pulse Compression Signals," *Proceedings of the IEEE*, 52 (11), pp. 1369-1371, 1964.
- [52] N. Levanon, and E. Mozeson, *Radar Signals*, Wiley, Hoboken, New Jersey, 2004.
- [53] P. S. Brandon, "The design of a nonlinear pulse compression system to give a low loss high resolution radar performance," *Marconi Rev.*, 36, pp. 1-45, 1973.
- [54] R. Price, "Chebyshev low pulse compression sidelobes via a nonlinear FM," *National Radio Science Meeting of URSI*, Seattle, WA, 1979.
- [55] P. Yichun, P. Shirui, Y. Kefeng, and D. Wenfeng, "Optimization design of nlfm signal and its Pulse compression simulation," *Radar Conference, Proceedings of the IEEE*, pp. 383-386, 2005.
- [56] C. E. Cook and M. Bernfeld, *Radar Signals*. Academic press, New York, 1967
- [57] F. J. Harris, "On the Use of Windows for Harmonic Analysis with the Discrete Fourier Transform," *Proceedings of the IEEE*, Vol. 66, pp. 51-84, 1978
- [58] J. A. Johnston, and A. C. Fairhead, "Waveform design and doppler sensitivity analysis for nonlinear FM chirp pulsed," *IEE Communications, Radar and Signal Processing*, Vol. 133, pp. 163-175, 1986.

- [59] F. W. Gembicki, “Vector Optimization for Control with Performance and Parameter Sensitivity Indices,” *Ph.D. Thesis*, Case Western Reserve Univ., Cleveland, Ohio, 1974
- [60] R. H. Stolt, “Migration by Transform,” *Geophysics*, 43 (1): pp. 23–48, February 1978.
- [61] J. Saeedi, K. Faez, “A back-projection autofocus algorithm based on flight trajectory optimization for synthetic aperture radar imaging,” *Multidimensional Systems and Signal Processing*, pp. 1-21, December 2014.
- [62] J. Saeedi, S.M. Alavi, “Improved navigation-based motion compensation for LFMCW synthetic aperture radar imaging,” *Signal, Image and Video Processing*, 10 (2), pp. 405-412, 2016
- [63] A. Meta, P. Hoogeboom, and L.P. Ligthart, “Signal processing for FMCW SAR,” *IEEE Trans. Geosci. Remote Sens.*, 45 (11), pp. 3519–3532, 2007.
- [64] M. Horemuz, J.V. Andersson, “Polynomial interpolation of GPS satellite coordinates,” *GPS Solut* (10), pp. 67–72, 2006.
- [65] M. Schenewerk, “A brief review of basic GPS orbit interpolation strategies,” *GPS Solutions* (6), pp. 265–267. 2003.
- [66] E. Goldberg, *Genetic Algorithms in Search, Optimization & Machine Learning*, Addison-Wesley, 1989.
- [67] S. Kirkpatrick, C.D. Gelatt, M.P. Vecchi, “Optimization by simulated annealing,” *Science* 220, pp. 671–680, 1983.
- [68] S. Rao, *Optimization: Theory and Applications*, Wiley, New York, 1984.
- [69] J. Kennedy, R.C. Eberhart, “A discrete binary version of the particle swarm algorithm,” In: *Proceedings of the 1997 IEEE Conference on Systems, Man, and Cybernetics*, Piscataway, NJ, pp. 4104–4109, 1997.

- [70] C. Stringham, and D.G. Long, "Improved processing of the CASIE SAR data," *IEEE International Geoscience and Remote Sensing Symposium 2011*, July 2011.
- [71] M. C. Edwards, "Design of a continuous-wave synthetic aperture radar system with analog dechirp," *Master's thesis*, Brigham Young University, 2009.

## Appendix

**Principle of stationary phase:** The principle of stationary phase (PoSP) is an integration method [29], which can be applied to solve oscillatory integrals of the following form:

$$S(k_x) = \int_a^b s(x)e^{j\phi(x)}dx \quad (\text{A.1})$$

where  $s(x)$  varies slowly, and  $\phi(x)$  changes with many cycles over the integration interval.

Based on these conditions, the above integral over most of the  $x$  interval adds little value to  $S$  [29]. An exception happens for the integral value at the stationary points of the phase function  $\phi(x)$ , defined as those values of  $x$  for which

$$\frac{d}{dx}[\phi(x)] = 0 \quad (\text{A.2})$$

The PoSP states that the integral of (A.1) receives its greatest influences from those values of  $x$  which are stationary points of  $\phi(x)$  on the interval  $[a, b]$ . The following two steps are performed to estimate the integral (A.1):

- Determine the location of the stationary point(s) of  $\phi(x)$ .
- Evaluate the integrand of (A.1) at the stationary point  $x^*$ . If  $x^*$  is the only stationary point on  $[a, b]$ , then an approximation for the integral is obtained as:

$$\int_a^b s(x)e^{j\phi(x)}dx \approx \left[ \frac{-\pi}{2\phi''(x^*)} e^{-j\frac{\pi}{2}} \right]^{\frac{1}{2}} s(x^*)e^{j\phi(x^*)} \quad (\text{A.3})$$

For radar signal processing applications, the factor in square brackets in (A.3), including magnitude and phase, is constant ( $\phi''(x^*)$  is constant).



## Synthetic Aperture Radar Signal Processing Using Nonlinear Frequency Modulation and Phase Error Compensation

In this thesis, signal-processing issues of synthetic aperture radar (SAR) have been under consideration. Specifically, we have focused on two topics in the field of SAR signal processing in this research consisting of nonlinear frequency modulation (NLFM) signal in SAR imaging, and phase error compensation using a new autofocus algorithm. In the first study, a new NLFM waveform is developed, which can be used as a transmitted chirp in SAR imaging to improve the imaging quality compared to LFM chirp signal. The new NLFM is constructed based on pricewise linear functions which is optimized using multi-objective optimization. Different signal prospecting algorithms including time domain correlation, back-projection, omega-k, and range-Doppler algorithm are investigated in order to use NLFM as the transmitted chirp in SAR system. In addition, a modified motion compensation algorithm using navigation data is proposed for frequency domain algorithm. Strip-map SAR geometry is considered to generate SAR raw signal for both point and distributed targets, in order to validate the new offered chirp signal and the proposed motion compensation algorithm. In the second study, a new autofocus algorithm is proposed for back-projection (BP) image formation of SAR imaging. The approach is based on maximizing an objective function obtained by prominent points in different sub-apertures of constructed SAR image by varying the flight trajectory parameters. While image-quality-based autofocus approach together with BP algorithm can be computationally intensive, we use approximations that allow optimal corrections to be derived. The approach is applicable for focusing different signal processing algorithms by obtaining modified flight trajectory parameters.